

ACTIVE AND PASSIVE MICROWAVE REMOTE
SENSING OF HIGHER LATITUDE PRECIPITATION

by

Mark S. Kulie

A dissertation submitted in partial fulfillment of

the requirements for the degree of

Doctor of Philosophy

(Atmospheric and Oceanic Sciences)

at the

UNIVERSITY OF WISCONSIN-MADISON

2010

UMI Number: 3421955

All rights reserved

INFORMATION TO ALL USERS

The quality of this reproduction is dependent upon the quality of the copy submitted.

In the unlikely event that the author did not send a complete manuscript and there are missing pages, these will be noted. Also, if material had to be removed, a note will indicate the deletion.



UMI 3421955

Copyright 2010 by ProQuest LLC.

All rights reserved. This edition of the work is protected against unauthorized copying under Title 17, United States Code.



ProQuest LLC
789 East Eisenhower Parkway
P.O. Box 1346
Ann Arbor, MI 48106-1346

A dissertation entitled

**ACTIVE AND PASSIVE MICROWAVE REMOTE
SENSING OF HIGHER LATITUDE PRECIPITATION**

submitted to the Graduate School of the
University of Wisconsin-Madison
in partial fulfillment of the requirements for the
degree of Doctor of Philosophy

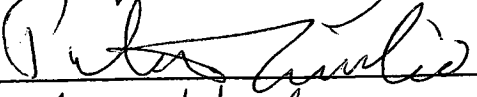
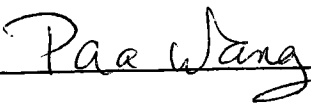
by

Mark S. Kulie

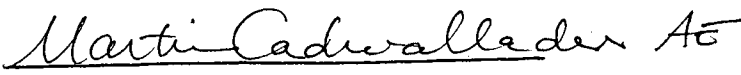
Date of Final Oral Examination: 22 March 2010

Month & Year Degree to be awarded: **December** **May 2010** **August**

Approval Signatures of Dissertation Committee

Signature, Dean of Graduate School

 **AE**

Abstract

Space-borne microwave remote sensing of precipitation at higher latitudes is investigated using an integrated observational and modeling approach. An ice particle model database containing optical properties of twenty-five ice habits is developed and serves as the centerpiece of both a radar-based snowfall retrieval scheme and a combined active/passive modeling system. Equivalent radar reflectivity factor (Z_e) – snowfall rate (S) and ice water content (IWC) relationships are first derived, and their sensitivity to ice model, size distribution, and temperature are demonstrated. Next, a combined active/passive modeling system that converts CloudSat Cloud Profiling Radar (CPR) observations to simulated microwave brightness temperatures (T_B) is utilized to physically assess the ice particle models under precipitating conditions. Simulation results indicate certain ice models (e.g., low-density spheres) produce excessive scattering and implausibly low simulated T_B 's for stratiform precipitation events due to the combined effects of excessive derived ice water paths (IWP) and extinction. An ensemble of non-spherical ice particle models, however, consistently produces more physically realistic results under most circumstances and adequately captures the radiative properties of frozen hydrometeors associated with precipitation – with the possible exception of very high IWP events. Large derived IWP uncertainties are also noted and may indicate IWP retrieval accuracy limitations using passive microwave observations. Simulated brightness temperature uncertainties due to the ice particle model can approach 9 (5) K at 89 (157) GHz for high IWP conditions associated with

snowfall and $\sim 2-3$ ($\sim 1-2$) K under typical mid-latitude stratiform rain conditions. These uncertainties – and sample error correlations and covariances for select microwave frequencies - display distinct variability due to IWP, precipitation type, satellite zenith angle, and frequency. Active-only snowfall retrievals using CPR near-surface reflectivity histograms indicate the dominant mode of global snowfall has extremely light reflectivity values. The average retrieved global snowfall rate is $\sim 0.3 \text{ mm h}^{-1}$, but shows regional variability with large uncertainties. Future multi-frequency space-borne radars are also evaluated using proxy 35/13.6 GHz reflectivities, and potential snowfall detection shortcomings are noted.

Acknowledgments

The constructive comments and continual guidance from my doctoral committee members (Professors Ralf Bennartz, Grant Petty, Steven Ackerman, Pao Wang, and Peter Timbie) are gratefully acknowledged. I am especially indebted to my research advisor (Prof. Ralf Bennartz) for providing the opportunity to work with him, his research group, and the many collaborators who have visited over the past several years. Prof. Bennartz provided instrumental guidance throughout this research project and allowed me to creatively explore numerous research pathways, but always provided useful input, encouragement, and acted as a necessary focusing mechanism at key junctures of this work. I am also eternally grateful for the assistance provided by Dr. Chris O'Dell during the early stages of this research - especially for patiently conveying his infinite wisdom of the IDL programming language. Drs. Sabrina Pinori, Min-Jeong Kim, and Benjamin Johnson are also acknowledged for fruitful early discussions about passive microwave remote sensing.

Drs. Min-Jeong Kim and Gang Hong are acknowledged for supplying microwave optical properties for some of the ice particle models used in this study, and Dr. Guosheng Liu is commended for making his optical properties database publicly available and easily accessible. Drs. Yong Chen and Fuzhong Weng provided the combined CloudSat/MHS dataset, which proved to be the perfect testbed for the combined active/passive modeling system presented in this study. Dr. Thomas

Greenwald provided crucial tools, feedback, and encouragement for the assessment of ice particle models, and his collaborative efforts are also acknowledged. Mr. Michael Hiley provided extensive data processing assistance for this study and provided excellent scientific support for many aspects of this study. Finally, this work would not have been possible without the support, patience, and understanding of my family. Special thanks to Terri, Katy, and Alex for enduring frequent late-night and weekend work sessions while I completed this work and for providing a necessary outlet when I needed it most.

This research was partially supported by NASA Grant NNX07AE29G and the Joint Center for Satellite Data Assimilation.

Table of Contents

ABSTRACT	I
ACKNOWLEDGMENTS.....	III
TABLE OF CONTENTS	V
LIST OF TABLES	VII
LIST OF FIGURES	IX
1. INTRODUCTION.....	1
2. INSTRUMENTS AND DATA	8
A. CPR.....	8
B. AMSR-E.....	9
C. MHS.....	9
3. MICROWAVE OPTICAL PROPERTIES DATABASE.....	10
A. BACKGROUND	10
B. DATABASE DESCRIPTION.....	14
C. OPTICAL PROPERTIES.....	17
4. PARTICLE SIZE DISTRIBUTION	33
A. EXPONENTIAL PSD	33
B. FIELD ET AL. (2005, 2007) PSD	35
C. DERIVING THE PSD	40
D. PSD EXAMPLES	42
5. Z_E-S/Z_E-IWC RELATIONSHIPS	51
A. OVERVIEW	51
B. METHODOLOGY	51
C. SENSITIVITY TO ICE PARTICLE MODEL AND TEMPERATURE.....	53
D. ENSEMBLE AVERAGED Z_E -S RELATIONSHIPS	54
E. SENSITIVITY TO PSD	55
6. ACTIVE/PASSIVE ASSESSMENT OF ICE PARTICLE MODELS	68
A. OVERVIEW	68
B. CPR/AMSR-E/MHS DATASET.....	71
C. METHODOLOGY	72
D. CASE STUDY RESULTS	75
i. <i>OVERVIEW</i>	75
ii. <i>VALIDITY OF ICE PARTICLE MODELS</i>	76
iii. <i>SIMULATION UNCERTAINTIES AND ERRORS</i>	78
iv. <i>INDIVIDUAL ICE PARTICLE MODEL COMPARISONS</i>	80
v. <i>SUMMARY OF CASE STUDY RESULTS</i>	81
E. GLOBAL RESULTS.....	82
i. <i>STATISTICAL COMPARISON BY PRECIPITATION TYPE</i>	82
ii. <i>DEPENDENCE ON ICE CONTENT</i>	84
iii. <i>ERROR COVARIANCE/CORRELATIONS</i>	87
F. SUMMARY	89

7. SPACE-BORNE RADAR SNOWFALL RETRIEVALS	110
A. OVERVIEW	110
B. DATA	111
C. METHODOLOGY	113
D. GLOBAL RESULTS.....	118
E. SENSITIVITY TO PARTICLE TYPE	120
F. SENSITIVITY TO VERTICAL CONTINUITY THRESHOLD.....	121
G. REGIONAL RESULTS.....	124
<i>i. GREENLAND</i>	126
<i>ii. GREENLAND OCEAN</i>	128
<i>iii. ANTARCTICA AND NORTH CENTRAL RUSSIA</i>	129
H. SUMMARY	130
8. SUMMARY AND OUTLOOK	145
9. APPENDIX	147
10. REFERENCES	151

List of Tables

Table 3.1: Ice particle model habits and abbreviations from the DDA results of Hong (2007), Kim et al. (2007), and Liu (2008). Surrussavadee and Staelin (2006; SS06) frequency-dependent soft spheres and three variable-density fluffy spheres for snow, graupel, and hail are also indicated. The range of maximum particle dimension (D_{max}) and equivalent particle radii (R_e) from these studies are also indicated.	23
Table 3.2: Coefficients and exponents for mass-particle size (Eq. 3.4) and fall speed-particle size (Eq. 4.3) relationships. SI units are assumed. References for the fall speed-particle relationships are indicated in the footnotes below.	24
Table 5.1: Ensemble averaged 35 GHz Z_e - S relationships – and upper and lower 1- σ uncertainty results – for all ice models (spheres) and only the non-spherical models (DDA) in Table 3.1.	59
Table 5.2: Same as Table 5.1, but for 13.6 GHz.	59
Table 6.1: Description of the different cloud and precipitation categories used for simulation versus observation comparisons. Abbreviations used to denote the categories in various figures and tables are also indicated. The number of CloudSat/AMSR-E/MHS coincident observations for each category (N_{obs}) used to generate the statistics in Fig. 6.7 is also shown.	94
Table 6.2: Lower freezing level mid-latitude stratiform precipitation model error covariances [K^2] (bold; lower left half) and correlations (upper right half) from the 40 dBZ _{int} data bin for the following frequencies: 18V, 23V, 36V, 89V, and 157 GHz.	95
Table 6.3: Same as Table 6.2, but for higher freezing level mid-latitude stratiform precipitation.	96
Table 7.1: Derived Z_e - S relationships for various shapes and frequencies used in Section 7. Published Z_e - S relationships for other recent studies of dry snowfall are also shown. Z_e has units of [$mm^6 m^{-3}$], while S is assumed to be in units of [$mm h^{-1}$].	136
Table 7.2: The first two columns are percentages of near-surface proxy DPR-like radar reflectivities at 35/13.6 GHz greater than or equal to the proposed DPR minimum detectable signal of 12/17 dBZ _e calculated from CPR observations. The last two columns are the percentage of total snowfall accumulation that would be detected at 35/13.6 GHz for the same snowfall dataset. Bold numbers indicate percentages after quality-control measures were applied to clutter-contaminated data points (see Section 7g).	137
Table 9.1: Coefficient a for the temperature-dependent 94 GHz $Z_e = aS^b$ relationships.	147
Table 9.2: Exponent b for the temperature-dependent 94 GHz $Z_e = aS^b$ relationships.	148
Table 9.3: Same as Table 9.1, but for 35 GHz.	149

Table 9.4: Same as Table 9.2 but for 35 GHz.150

v

List of Figures

Fig. 3.1: Ice particle model shapes from Hong (2007; Fig. 1).....	25
Fig. 3.2: Ice particle model shapes from Liu (2004; Fig. 1).....	26
Fig. 3.3: Ice particle model shapes from Kim et al. (2007; Fig. 1).....	27
Fig. 3.4: 150 GHz optical properties for the ice particle models in Table 3.1. The following optical properties are shown: (a) extinction cross-section, (b) single scatter albedo, and (c) asymmetry parameter.	28
Fig. 3.5: Mass- D_{max} relationships for (a) all ice models from Table 3.1 and (b) only the six-bullet/arm shapes from Liu (2004), Hong (2007), and Kim et al. (2007).	29
Fig. 3.6: Same as Fig. 3.4, but shown as a function of particle mass.....	30
Fig. 3.7: Backscatter cross-section (σ_b) and backscatter efficiency ($Q_{b, eff}$) for the ice particle models in Table 3.1 for 35 and 94 GHz.	31
Fig. 3.8: Panels (a) and (b) respectively illustrate extinction cross-section (σ_e) and σ_e per unit mass at 150 GHz for the six-bullet/arm shapes from Liu (2004), Hong (2007), and Kim et al. (2007). Panels (c) and (d) respectively illustrate backscatter cross-section (σ_b) and σ_b per unit mass at 94 GHz for the same shapes in Panels (a) and (b).	32
Fig. 4.1: Frozen particle size distributions from the observations of Braham (1990), adapted from Matrosov (2007). Colored lines indicate average results for the snowfall rates indicated.....	45
Fig. 4.2 (a) Mass-size and (b) fall speed-size relationships of aggregates from various studies. Shapes indicated include aggregates of unrimed radiating assemblages of dendrites (LH1) and unrimed radiating assemblages of plates, side planes, bullets, and columns (LH2) from Locatelli and Hobbs (1974), and other aggregates from Mitchell (1996; M96), Heymsfield et al. (2004; H04), Mitchell and Heymsfield (2005), and Wilson and Ballard (1999; WB99). The best fit mass/fall speed-size relationships derived from all of these studies is indicated by the thick, solid line (AVG).....	46
Fig. 4.3: Derived snowfall rates for the 49 Braham (1990) cases using the best-fit mass-size (m - D_{max}) and fall speed-size (v - D_{max}) relationships from Fig. 4.2 (Best-fit). Derived snowfall rates using the upper and lower limit m - D_{max} and v - D_{max} relationships in Fig. 4.2 are also indicated.	47
Fig. 4.4: Sample ice particle size distributions derived using the Field et al. (2005) parameterization assuming the LR6 shape and an input ice water content of 1.0 (solid) and 0.1 g m ⁻³ (dash-dot) at different temperatures (colored lines).	48
Fig. 4.5: Derived ice particle size distributions using the Field et al. (2005) parameterization for various ice models (see Table 3.1 for abbreviations) assuming an ice water content of 1.0 g m ⁻³	49

- Fig. 4.6:** Derived ice particle size distribution using the Field et al. (2005; F05) (solid) and Field et al. (2007; F07) (dash) parameterization at different temperatures (colored lines) for an assumed liquid equivalent snowfall rate of (a) 0.1 and (b) 1.0 mm h⁻¹. The Braham (1990; B90) exponential PSD is also indicated (red dashed line). The average aggregate $m-D_{max}$ and $v-D_{max}$ relationships (Fig. 4.2) are also assumed.50
- Fig. 5.1:** Equivalent radar reflectivity factor (Z_e) – ice water content (IWC) relationships for the ice particle models in Table 3.1 for an assumed temperature of -7.5 C.60
- Fig. 5.2:** Equivalent radar reflectivity factor (Z_e) – liquid equivalent snowfall rate (S) relationships for the ice particle models in Table 3.1 for an assumed temperature of -7.5 C.61
- Fig. 5.3:** Same as Fig. 5.2, but for 35 GHz.62
- Fig. 5.4:** Same as Fig. 5.2 and Fig. 5.3, but showing variation of Z_e - S relationships for the LR3 (solid), LSS (dash-dot), and FS (dash) shapes at various temperatures between -2.5 and -42.5 C (colored lines).63
- Fig. 5.5:** Ensemble-averaged 94 GHz Z_e - S relationships for (a) all ice models and (b) only the non-spherical ice models in Table 3.1. Upper and lower 1- σ uncertainty bounds are also indicated.64
- Fig. 5.6:** Z_e - S relationships for the LR6 and LSS habits at 94 and 35 GHz using the F05 (dark blue), F07 (light blue), and B90 (green) PSD's. The F05 and F07 results are derived at -2.5 C (solid) and -17.5 C (dash).65
- Fig. 5.7:** Contribution of different D_{max} values to the total 94 GHz Z_e (in dBZ_e) for the LR6 habit at (a) 0.1 mm h⁻¹ and (b) 0.5 mm h⁻¹. Panels (c) and (d) are the same as panel (a) and (b), except for the LSS shape. The F05 (dark blue), F07 (light blue), and B90 (green) PSD's are also indicated. The F05 and F07 results are derived at -2.5 C (solid) and -17.5 C (dash). B90 results using the average aggregate $m-D_{max}$ and $v-D_{max}$ properties (Fig. 4.2) are also shown (green dash).66
- Fig. 5.8:** Same as Fig. 5.7, but for 35 GHz.67
- Fig. 6.1:** Panel (a) shows the attenuation-corrected CPR reflectivity and freezing level (blue line) from CloudSat orbit 01497, panels (b) to (e) show brightness temperature [K] for the following instruments and channels (black lines/asterisks): (b) AMSR-E 36V and (c) 89V GHz; (d) MHS 89 and (e) 157 GHz. Panel (f) also shows AMSR-E derived LWP (green) and IWP (blue) derived from the DDA ensemble results. Simulated T_B 's for the DDA ensemble and 1- σ uncertainties (light gray shading), as well as spherical and Kim et al. (2007) models (using same color scheme as Fig. 5.1) are also included in panels (b)-(e). Panel (a) also shows five separate zones that are used for calculating the individual ice habit biases in Fig. 6.6.97
- Fig. 6.2:** Derived ice water path [kg m⁻²] for fluffy spheres (FS), graupel (FG), and hail (FH), as well as the Kim et al. (2007) six-arm rosette (KR6). The DDA ensemble average and 1- σ uncertainty results (light gray shading) are also shown.98
- Fig. 6.3:** Simulated volume extinction coefficient [km⁻¹] as a function of ice water content [g m⁻³] for the same ice habits indicated in Fig. 6.2.99

- Fig. 6.4:** Simulated T_B uncertainties for 36V (light dash), 89V (dark solid), 89 (light solid), and 157 (light dash-dot) GHz. The five separate zones from Fig. 6.1a are also shown.100
- Fig. 6.5:** (a) AMSR-E (dark) and simulated (light) scattering index for 89 GHz [K], (b) MHS 89 (dark asterisk)/157 (light diamond) and simulated 89(dark solid line)/157(light solid line) GHz brightness temperature depression [K] compared to water vapor-only results, and (c) MHS (triangles) and simulated (solid line) 157-89 GHz brightness temperature difference [K]. The latitude domain corresponds to Fig. 6.1 for CloudSat orbit 01497.101
- Fig. 6.6:** Simulated versus observed 157 GHz brightness temperature bias [K] corresponding to the case study illustrated in Fig. 6.1. The “All” column refers to the entire latitudinal domain shown in Fig. 6.1, while the other columns (I, II, II, IV, V) refer to the regional subsets indicated in Fig. 6.1a. The ice habits follow the same nomenclature as Table 3.1.102
- Fig. 6.7:** Simulated DDA ensemble brightness temperature versus AMSR-E/MHS (a) bias, (b) bias-corrected root mean square error (rmse), (c) correlation, and (d) average simulated T_B uncertainty ($\bar{\sigma}$) for different cloud and precipitation categories. Abbreviations for the cloud and precipitation categories can be found in Table 6.1.104
- Fig. 6.8:** Histograms of column-integrated reflectivity above the freezing level [dBZ] for different precipitation categories in 2 dB bins.105
- Fig. 6.9:** Retrieved ice water path, IWP [kg m^{-2}] versus column-integrated reflectivity above the freezing level, Z_{int} [$\text{mm}^6 \text{m}^{-2}$] (shown in dBZ) for all mid-latitude stratiform cases using the DDA ensemble of ice particles. $1-\sigma$ uncertainties for every 2 dB Z_{int} data bin are also indicated.106
- Fig. 6.10:** Simulated T_B uncertainty [K] (top) and bias corrected root mean square error [K] (bottom) as a function of Z_{int} for the different precipitation categories listed in Table 6.1.107
- Fig. 6.11:** Simulated versus observed 157 GHz brightness temperature bias [K] using the DDA ensemble of ice particle models for the mid-latitude stratiform precipitation category.108
- Fig. 6.12:** Panels (a) 157-89V and (b) 89V-36V show error correlations for three different precipitation categories as a function of integrated reflectivity above the freezing level (Z_{int}). Panel (c) displays 157 GHz error variances for the same precipitation categories. The low freezing level mid-latitude stratiform (Low FL), higher freezing level mid-latitude stratiform (High FL), and higher latitude, shallow convective precipitation categories are shown (see Table 6.1).109
- Fig. 7.1:** Similar to Fig. 3.7b, but the following three ice particle models used in Section 6 – LR3 (black), HA (red), and SS (purple) – are highlighted by thick, solid lines.138
- Fig. 7.2:** (a) Radar reflectivity factor, Z_e [$\text{mm}^6 \text{m}^{-3}$], as a function of snowfall rate, S [mm h^{-1}], at 94 GHz for the three different ice particle models highlighted in Fig. 7.1 – LR3 (diamonds), HA (triangles), and SS (crosses). Best-fit lines using the Z_e - S relationships outlined in Table 7.1 are also indicated through the data points for each ice particle model. (b) Same as (a), but for S as a function of Z_e (using the Z_e - S relationships from Table 7.1) at 94 GHz. (c) Same as (a), but for 35 GHz. (d) Same as (a), but for 13.6 GHz.139
- Fig. 7.3:** (a) Radar reflectivity factor histograms in 1 dB Z_e bins for observed CloudSat CPR snowfall events (solid line) and calculated proxy radar reflectivities for 35 GHz (dash) and 13.6 GHz (dash-

dot) using the LR3 Z_e - S relationship from Table 7.1. The thick solid line on the 35 and 13.6 GHz histograms indicates the reflectivity bins that exceed the proposed minimum detectable signal (MDS) of the GPM DPR for each respective frequency. (b) Conditional snowfall rate histogram (left axis) and average conditional snowfall rate cumulative distribution function (right axis). The thick solid and dash-dot line on each curve represents the snowfall rate threshold corresponding to a MDS of 12 and 17 dBZ_e, respectively.140

Fig. 7.4: Radar reflectivity factor histograms for (a) 35 GHz and (b) 13.6 GHz for the LR3 (solid), HA (dash), and SS (dash-dot) shapes. The thick solid lines indicate the assumed MDS of 12 and 17 dBZ_e for 35 and 13.6 GHz, respectively. (c) Snowfall rate histograms and (d) cumulative distribution function of the snowfall rate histograms from (c) (expressed as an average snowfall rate) for LR3 (solid), HA (dash), and SS (dash-dot) shapes. The thick solid lines in (c) and (d) indicate the snowfall rate for each shape that corresponds to the assumed MDS of 12 dBZ_e for 35 GHz.....141

Fig. 7.5: (a) Radar reflectivity factor histograms in 1 dBZ_e bins for observed CloudSat CPR snowfall events based on the assumed vertical reflectivity thickness above the near-surface reflectivity value needed for a near-surface CPR observation to be included in the snowfall dataset (e.g., “1000 m” means the reflectivities must exceed -15 dBZ_e for ~1000 m above the near-surface reflectivity value). (b) Same as (a), but the ordinate is provided in a logarithmic scale to accentuate differences in the histograms above 20 dBZ_e. (c) Bar plot showing the frequency of occurrence of total snowfall cases included in the dataset for the various vertical reflectivity thresholds. (d) Same as (a), but for conditional snowfall rate histogram (left axis) and average conditional snowfall rate cumulative distribution function (right axis). Snowfall rates are calculated using the LR3 Z_e - S relationship in Table 7.1. The frequency of occurrence indicated on the ordinate is in units of 10⁵ in (a) and (d)...142

Fig. 7.6: Same as Fig. 7.3, but histograms are derived on a regional, not global, basis. Also, the average conditional snowfall rate thin dotted line shown for the Greenland, Greenland Ocean, and Antarctica regions represents the quality-controlled (QC) cumulative distribution function that alters the reflectivity pixels potentially associated with ground clutter in topographically complex regions....143

Fig. 7.7: CloudSat CPR radar reflectivity observations [dBZ_e] and ECMWF temperature [K] of three snowfall events over Greenland. The 6th reflectivity bin above the surface (“near-surface” reflectivity) and above are shown to correspond with the actual dataset used in this study. The land surface – derived from a digital elevation map database used in the official CloudSat products – is also indicated by the black line.144

1. Introduction

Over the past twelve years, the Tropical Rainfall Measuring Mission (TRMM; Kummerow 1998) – with its single-frequency (13.8 GHz) TRMM Precipitation Radar (PR) and multi-frequency TRMM Microwave Imager (TMI) – has demonstrated the unique synergy of space-borne radar and passive microwave observations to study clouds and precipitation in tropical regions. Similar to TRMM, the upcoming Global Precipitation Measurement (GPM; Smith et al. 2007) mission will also carry combined active/passive microwave instrumentation dedicated to precipitation investigation on its core satellite. The GPM core spacecraft will exceed the capabilities of TRMM by hosting the Dual-frequency Precipitation Radar (DPR) that will operate at 13.6 (Ku band) and 35.5 (Ka band) GHz and the GPM Microwave Imager (GMI) that will possess additional higher frequency channels near 166 and 183 GHz not included on the TMI. These extended capabilities, combined with a higher orbital inclination than TRMM, will expand GPM's coverage to higher latitudes and will allow combined active/passive precipitation detection and measurement from space on a near-global basis. Additional sensors – both currently available and proposed platforms to be launched in the future – without active microwave equipment will augment the core satellite and will strive to attain global temporal sampling of clouds and precipitation on the order of about three hours. Besides enhancing our knowledge of the global distribution of clouds, precipitation, and other essential geophysical parameters (e.g., sea surface temperature,

water vapor, winds, etc.), observations from GPM's unique sensor package should also benefit numerical weather prediction via improved data assimilation.

The ability of the GPM core satellite to sample precipitation at mid- to high-latitudes also presents challenges not frequently encountered by TRMM – most notably retrieving snowfall and lighter rain associated with climatologically lower freezing levels. Snowfall retrievals will be especially important since frozen precipitation comprises a non-negligible amount of the total precipitation at many higher latitude locations and has important hydrological and societal impacts. Snowfall also plays a crucial role in such important geophysical research topics like ice sheet dynamics, so knowledge of annual snowfall accumulations are extremely important to areas covered by large expanses of ice (e.g., Greenland, Antarctica, and alpine glacial regions). Additionally, the importance of obtaining global snowfall information and monitoring future fluctuations in its spatial distribution, frequency, and intensity are highlighted by recent reports of the accelerated effects of rapid climatic change experienced at higher latitudes (e.g., Krabill et al. 1999; Hinzman et al. 2005; Luckman et al. 2006). Satellite-based microwave remote sensing remains the most viable option to obtain global snowfall information since routine surface measurements of snow are scarce in remote regions where it frequently occurs. The need for enhanced, sustained observations of higher latitude precipitation has never been greater, and the importance of improved and accurate precipitation retrievals at higher latitudes – especially physically-based retrievals – cannot be overstated.

The current state-of-the-art microwave-based snowfall retrieval methodologies are still largely in the developmental stage and have mostly been comprised of proof-of-

concept investigations relying on case studies or numerical simulations of specific snowfall events to highlight the potential of microwave retrievals of snow (e.g., Katsumata et al 2000; Skofronick-Jackson et al. 2004; Noh et al. 2006; Kim et al. 2007; Johnson 2007; Grecu and Olson 2008). The practicality and viability of physically-based microwave retrievals of snowfall is still relatively unknown, and few large-scale global assessments have been attempted. Furthermore, many of the previously published works concentrated on heavier snowfall events, but recent snowfall studies using CloudSat's 94 GHz Cloud Profiling Radar (CPR) have indicated the dominant mode of global snowfall is associated with relatively low precipitation rates, and certain regions experience extremely light snowfall almost exclusively (Liu 2008a; Kulie and Bennartz 2009). Methods to successfully retrieve these ubiquitous light precipitation events need to be developed, or at the very least, a quantitative assessment of the potential snowfall and light precipitation that cannot be successfully detected and retrieved by GPM – with appropriate metrics for retrieval uncertainties – must be undertaken.

The extensive historical record of satellite-based passive microwave sensors is exceedingly rich and provides a vast dataset that can be used for GPM preparations. But passive-only microwave precipitation retrievals at higher latitudes using microwave imagers face many complicating factors that limit their ability to generate reliable results on a global scale. Multi-frequency over-ocean rainfall retrieval algorithms rely on a combination of emission and scattering signatures to retrieve surface precipitation rates (e.g. Petty 1994 a, b; Kummerow et al. 1996; Bauer et al. 2001; Wilheit et al. 2003 and many others). The “warm” emission signal emanates from liquid rain and cloud water to

increase the top-of-the-atmosphere (TOA) microwave brightness temperature when compared to clear sky microwave brightness temperatures appearing “cold” due to the relatively low ocean surface emissivity at microwave frequencies. The clear-sky, over-ocean signature is also distinctly polarized when viewed from an oblique angle and differs from the cloud/precipitation signature, which usually does not possess drastic polarization discrepancies. The microwave scattering signature is recognized as a brightness temperature depression at higher microwave frequencies (above ~85 GHz) due to the scattering effects of frozen particles of sufficient size (e.g., Spencer et al. 1989; Petty 1994 a, b). Significant scattering signatures generally coincide with convective or frontal precipitation containing large amounts of columnar ice content, although the scattering signature is not well-correlated with surface precipitation rates (Todd and Bailey 1995; Kidd 1998; Bennartz et al. 2002; Bennartz and Michelson 2003). This scattering signature also serves as the primary physical basis for microwave precipitation retrievals over land due to surface emissivity complications (e.g., Kongoli et al. 2003; McCollum and Ferraro 2003).

Snowfall retrievals are limited almost entirely to the scattering signature at higher microwave frequencies. Current and recent microwave imagers orbiting over higher latitudes [e.g. Special Sensor Microwave/Imager(SSM/I), Advanced Microwave Scanning Radiometer (AMSR-E)] possess either an 85 or 89 GHz channel, but high and variable land/ice surface emissivities at these frequencies dominate the passive microwave snowfall signal over the continents, thus rendering most retrievals over land virtually impossible except for only the most extreme snowfall events. Additionally, the

89 GHz response to light snowfall events over oceans makes it difficult to detect due to its often subtle signature; no reliable minimum snowfall detectability threshold has been established for over-ocean observations. Higher frequencies, such as near the 150 GHz window region and/or the combination of 150 GHz with a microwave channel near water vapor or oxygen absorption lines, show more promise than just the 89 GHz frequency for successfully retrieving snowfall due enhanced sensitivity to ice particle scattering effects combined with a better ability to mask out surface features (e.g., Kongoli et al. 2003; Bennartz and Bauer 2003). Currently available Advanced Microwave Sounding Unit-B (AMSU-B)/Microwave Humidity Sounder (MHS) instruments have such channels that can be utilized for GPM preparatory purposes. Last, and perhaps most important, higher latitude precipitation retrievals rely on two essential components that are sources of potentially large uncertainties: (1) ice particle models (either spherical or non-spherical) employed as proxies for frozen hydrometeors, and (2) ice particle size distribution (PSD) parameterizations. Further work must be undertaken to assess retrieval uncertainties due to these limiting factors.

Compared to the column-integrated retrievals from passive-only microwave precipitation observations, active space-borne observations offer the distinct advantage of providing high-resolution information about the vertical structure of clouds and precipitation by directly measuring the backscatter of microwave radiation due to both liquid and frozen hydrometeors and can be used as an additional constraint to coincident passive microwave observations. However, active satellite-based global snowfall and higher latitude rainfall observations are limited. The TRMM PR has collected tropical

precipitation data since 1997, but its orbital constraints, combined with its relatively high minimum detectable signal (~ 18 dBZ_e), preclude it from effectively observing snowfall events. True global active higher latitude precipitation measurements have only been available since the launch of CloudSat (Stephens et al. 2002) and its 94 GHz Cloud Profiling Radar (CPR; Tanelli et al. 2008) in 2006. The CPR's enhanced sensitivity allows it to observe light precipitating structures and most non-precipitating clouds. Despite its relatively brief existence, the CPR has already demonstrated an ability to effectively detect and retrieve snowfall properties (e.g., Liu 2008a; Matrosov et al. 2008; Hudak et al. 2008; Kulie and Bennartz 2009), albeit with currently large uncertainties due to the ice particle model and PSD limitations previously described (Kulie and Bennartz 2009). Future active snowfall observations will be also available from the GPM DPR. The dual-frequency capability of the DPR distinguishes it from the single frequency TRMM PR and CloudSat CPR and should allow GPM to more effectively observe lighter precipitation that commonly occurs at higher latitudes. The dual-frequency radar should also provide additional information about the droplet size distribution of rain and snow.

The most promising avenue to study combined active and passive microwave remote sensing of higher latitude precipitation – and its attendant uncertainties – in preparation for GPM is to utilize CloudSat CPR and passive microwave observations from AMSR-E and AMSU-B/MHS. This study describes the development of a microwave ice particle model optical properties database that serves as the key component of both an active-only microwave snowfall retrieval scheme and a combined active/passive microwave modeling system that is applied to higher latitude precipitation events. The ice particle

model database contains previously developed optical properties for a variety of spherical and non-spherical ice models. The active-only microwave snowfall retrieval scheme is used to study global snowfall retrievals and uncertainties due to ice particle model using CloudSat CPR observations and offers a preliminary assessment of the GPM DPR's ability to observe typical snowfall events. The combined active/passive modeling system is developed using currently available coincident CloudSat, AMSR-E, and MHS observations and can simulate all GPM microwave frequencies and proxy radar returns at GPM's DPR frequencies. This combined modeling platform allows the multi-frequency active and passive response to clouds and precipitation to be modeled in a physically consistent framework and enables the uncertainties associated with the forward calculations to be readily obtained. An especially important application of this modeling system is the objective assessment of the different ice particle models – and their associated scattering properties – under precipitating conditions. Systematic errors associated with the modeling system can also be obtained by comparing modeling results with actual observations from AMSR-E and AMSU-B/MHS.

A cursory description of the instruments and data used in this study is provided in Section 2. Sections 3 and 4 respectively describe the microwave optical properties database and ice particle size distribution parameterizations used throughout the study. Section 5 highlights temperature- and habit-dependent equivalent radar reflectivity factor (Z_e) – snowfall rate (S) and Z_e – ice water content (IWC) relationships derived from the microwave optical properties database and ice particle size distribution parameterizations that are employed throughout the study. Section 6 describes the active/passive microwave

modeling system and demonstrates the sensitivity – and an objective physical assessment – of higher frequency microwave brightness temperatures to the assumed ice particle model using the combined active/passive modeling system. Section 7 illustrates near-surface snowfall retrievals from a global and regional perspective using CloudSat data and provides an initial assessment of the GPM DPR’s snowfall detection efficacy. Summaries and an extended discussion of the main results from Sections 6 and 7 are also found at the end of each respective section, while Section 8 provides an overall summary and future work.

2. Instruments and Data

The data utilized in this study are from the following space-borne microwave instruments: CloudSat’s Cloud Profiling Radar (CPR), the Advanced Microwave Scanning Radiometer-Earth Observing System (AMSR-E), and the Microwave Humidity Sounder (MHS). The following sub-sections provide a brief overview of each instrument and the specific data products used in this study.

a. CPR

CloudSat (Stephens et al. 2002) carries an active, single-frequency, W-band (94 GHz) CPR (Tanelli et al. 2008) that has provided global cloud and precipitation profiles since its launch in 2006. The CPR is a non-scanning, near-nadir pointing instrument with a mean spatial resolution of about 1.5 km and a vertical range gate spacing of 500 m, although instrument oversampling effectively increases the CPR’s vertical resolution to

about 240 m in the CloudSat data products. This study utilizes the following CloudSat products available from the CloudSat Data Processing Center (<http://www.cloudsat.cira.colostate.edu/>): 2B-Geometric Profile (2B-GEOPROF), 2B-Cloud Water Content-Radar Only (2B-CWC-RO), 2C-Precipitation-Column (2C-PRECIP-COLUMN), and European Centre for Medium-Range Weather Forecasts-Auxiliary (ECMWF-AUX). Detailed product documentation can be obtained from the CloudSat Data Processing Center. Sections 6 and 7 further describe how these products are used in this study.

b. AMSR-E

The AMSR-E is a passive imaging radiometer on the Aqua satellite operating at six dual-polarized frequencies ranging from 6.9 to 89.0 GHz (Kawanishi et al. 2003). The AMSR-E conically scans at a constant 55 degree earth incidence angle with a swath width of about 1440 km and collects data with a mean spatial resolution varying from near 56 to 5 km for the 6.9 and 89 GHz channels, respectively. AMSR-E L2A Global Swath Spatially-Resampled Brightness Temperatures (Ashcroft and Wentz 2006) and Level-2B Global Ocean Swath Product (Wentz and Meissner 2004) products were obtained from the National Snow and Ice Data Center (<http://nsidc.org/data/amsre/>). Both Aqua and CloudSat fly in close formation as part of the “A-train” satellite constellation.

c. MHS

The MHS instrument flies on numerous European Organisation for the Exploitation of Meteorological Satellites' (EUMETSAT) and National Oceanographic and Atmospheric Administration's (NOAA) polar-orbiting platforms, and possesses five high-frequency microwave channels between 89.0 and 190.3 GHz that are exploited primarily for water vapor sounding purposes. Only the 89.0 and 157.0 GHz microwave window channels, however, will be utilized for precipitation-related purposes in this study. The MHS scans in a cross-track fashion with a total swath of over 1900 km and possesses a mean spatial resolution of about 16 km at nadir, and only near-nadir MHS observations will be utilized in this study. MHS level 1B data are publicly available from NOAA's Comprehensive Large Array-data Stewardship System (<http://www.nsof.class.noaa.gov/saa/products/welcome/>).

3. Microwave Optical Properties Database

a. Background

Remote sensing of clouds and precipitation is complicated by the wide variety of ice particle habits occurring in the atmosphere governed by atmospheric conditions – such as the amount of supersaturation with respect to ice and ambient temperature – and cloud-scale processes (Pruppacher and Klett 1997). Properly describing the complex interaction of microwave radiation with a potentially diverse population of frozen

particles is critical for atmospheric remote sensing and modeling purposes, and numerous studies have been undertaken to find both realistic and computationally inexpensive methods to perform this challenging task. For instance, non-spherical ice particles have commonly been modeled as equivalent spheres – either as “solid” spheres (e.g., Liu and Curry 2000; Evans et al 2002; Liu 2004), lower density “soft” or “fluffy” spheres (e.g., Bauer et al. 1999; Bennartz and Petty 2001; Petty 2001; Liu 2004; Surussavadee and Staelin 2006), or a host of other possible representations (e.g., Donovan et al. 2004) – for the purposes of calculating scattering and absorption characteristics of frozen hydrometeors at microwave frequencies. These equivalent sphere methods allow optical properties of frozen particles to be calculated efficiently using Mie (1908) theory, although soft spheres require mixing rules (Maxwell-Garnet 1904; Bruggeman 1935) to calculate an effective dielectric constant of the medium representing the ice particle, which can be a mixture of ice and air for “dry” particles or an ice/air/water mixture for “wet” particles. Studies have illustrated varying results based on what mixing rule is invoked for a given situation, and further variability arises when the matrix or inclusion in the Maxwell-Garnet methodology is changed among the possible constituents (e.g., Bauer et al. 2000; Meneghini and Liao 2000; Johnson and Petty 2004; Johnson 2007). Another option besides the equivalent sphere/Mie pathway to generate optical properties is to represent frozen particles as oblate spheroids and utilize the T-matrix method (e.g., Mishchenko and Travis 1998). Matrosov et al. (2005) and Matrosov (2007) have employed this methodology and demonstrated some degree of success when comparing dual frequency radar observations of snowfall to modeled results. Furthermore,

Matrosov et al. (2005) points out that aggregates – which tend to be the dominant form of frozen particle in accumulating snowfall – are potentially difficult to model by other means and found using oblate spheroids with a spheroid aspect ratio of about 0.6 produces optimal results. It should be noted that the T-matrix method cannot be used on particles with large aspect ratios or irregularly-shaped ice habits, so many ice particles may not be adequately represented by this method.

An increasingly popular, but computationally more expensive, alternative to the equivalent spheres/Mie methodology is to model the interaction of microwave radiation with non-spherical frozen particle models using numerical methods such as the Discrete Dipole Approximation (Purcell and Pennypacker 1973; Draine 1988; Draine and Flatau 1994). The major advantage of the Discrete Dipole Approximation (DDA) is the flexibility for ice particles to be represented by more complex, and presumably realistic, shapes than spherical models by portraying them as an array of dipoles that are subjected to an electromagnetic wave by using readily available computing code – such as DDSCAT (Draine and Flatau 2004) – to calculate single scattering ice particle properties. Unlike fluffy spheres, no dielectric mixing rules are required when using the DDA method. DDA-based optical properties suitable for passive and active microwave remote sensing applications have been calculated by numerous investigators for a wide range of ice particle shapes, including cylindrical columns, various forms of hexagonal columns, multi-appendage rosettes, disks, plates, droxtals, planar snowflakes, and simple aggregates (Evans and Stephens 1995; Liu 2004, 2008b; Donovan et al. 2004; Kim 2006; Hong 2007a). While the modeled shapes in these studies are definitely more complex

than spheres and may sufficiently represent pristine ice crystals found in non-precipitating clouds such as high-level cirrus, they are still admittedly highly idealized and by no means represent the full spectrum of possible frozen habit types, especially for aggregate-type particles that tend to dominate accumulating snowfall. Numerous investigations, however, have employed such idealized non-spherical shapes to represent frozen hydrometeors in microwave remote sensing studies with varying degrees of success (e.g., Kim et al. 2005; Noh et al. 2006; Kim et al. 2007; Kulie and Bennartz 2009). Additional DDA-related work is currently being performed using more complicated, large aggregate models that may be more applicable for near-surface snowfall retrieval applications (e.g., Petty and Huang 2010). All of these highlighted studies assume the modeled particles are randomly oriented – a suitable assumption for acquiescent atmospheric conditions – and sufficiently “dry” (i.e., no rimed or partially melted surfaces).

The recent DDA-themed studies differ slightly in the particular ice habits, range of particle sizes, and microwave frequencies being considered in each respective investigation, but many common themes arise from their collective work. Their results universally highlight the large differences, especially at larger particle sizes, in single scattering properties evident between the different modeled ice habits, as well as between DDA-based optical properties and those derived using solid and/or fluffy equivalent spheres. Liu (2004) specifically showed the DDA-produced scattering and absorption cross-sections (normalized by an effective particle cross sectional area) largely fall between the solid and fluffy sphere representations for many different particles at larger

(≥ 2 mm) maximum particle dimensions. Kim (2006) illustrated DDA-generated optical properties for passive microwave applications are mostly shape independent when the size parameter is less than about 2.5 and spherical models may be appropriate to use below this threshold. Large differences in optical properties, however, are observed when the size parameter exceeds 2.5, where the size parameter (x) is defined as:

$$x = \frac{2\pi r_e}{\lambda}, \quad (3.1)$$

where r_e is an equivalent particle radius [r_e is defined as the radius of the frozen particle such that the mass equals $(4/3)\pi r_e^3 \rho_i$, where ρ_i is the density of pure ice (917 kg m^{-3})] and λ the wavelength of interest. Hong (2007a) showed similar results and also highlighted the sensitivity of the DDA-derived results to different assumed ice habit compositions used to describe the overall distribution of frozen cloud particles.

b. Database description

A standardized database containing microwave optical properties of twenty-five ice particle models has been compiled for use throughout this study. Table 3.1 briefly describes the ice particle models used in this study from previously published work, as well as corresponding abbreviations for the ice habits and maximum particle diameter (D_{max}) ranges from the original sources. The particle equivalent radius (r_e) range is also

shown. Non-spherical ice particle models and their respective DDA-based optical properties from Hong (2007a,b; hereinafter H07), Kim et al. (2007; hereinafter K07), and Liu (2004; hereinafter L04) are included in the database. Renditions of the H07 columns, plates, rosettes, aggregates, and droxtals are shown in Fig. 3.1. The L04 habits consisting of columns, plates, rosettes, and planar snowflakes are indicated in Fig. 3.2, while the K07 column and rosette models are presented in Fig. 3.3.

Fluffy sphere results using three commonly assumed effective densities (ρ_e) used to represent snow ($\rho_e = 100 \text{ kg m}^{-3}$), graupel ($\rho_e = 400 \text{ kg m}^{-3}$), and hail ($\rho_e = 700 \text{ kg m}^{-3}$) are also indicated in Table 3.1. Such “soft” or “fluffy” spheres are used extensively in precipitation retrieval algorithms for current passive microwave sensors (e.g., Kummerow et al. 2001; Wilheit et al. 2003) and are standard ice particle models embedded within the Joint Center for Satellite Data Assimilation’s (JCSDA) Community Radiative Transfer Model (CRTM; Han et al. 2006). Additional spherical models from Surusavadee and Staelin (2006; hereinafter SS06) are also shown in Table 3.1. These spherical models utilize empirically calculated, frequency-dependent densities for the snow and graupel categories. It should be noted that the SS06 spherical results are rooted in the DDA methodology. SS06 derived ice factors, or effective particle densities, that produced Mie scattering cross-sections comparable to scattering cross-sections derived by DDA calculations of equal-mass, non-spherical ice habit models. SS06 found hexagonal plates produced corresponding ice factors for snow that compared well with multi-frequency passive microwave observations, while rosettes worked best for the graupel category.

Optical properties, such as extinction and scattering properties, from the various DDA and spherical models shown in Table 3.1 are interpolated to a common D_{max} grid with a $20\ \mu\text{m}$ D_{max} spacing between a range of 0.1 and 5.5 mm. Note that some of the ice particle models in Table 3.1 have a maximum D_{max} value less than 5.5 mm (e.g., L04 columns and plates and K07 shapes). Three options are provided in the database to account for the optical properties of such shapes between the D_{max} value shown in Table 3.1 and 5.5 mm: (1) direct extrapolation of the optical properties to 5.5 mm; (2) all optical properties above D_{max} are assigned a constant value equivalent to their respective values at D_{max} ; and (3) no extrapolation performed. When heavy snowfall rates or high ice water contents exist, the upper D_{max} threshold of 5.5 mm range may not be sufficient to account for large particles that can strongly influence quantities such as radar reflectivity factor. Therefore, an option also exists to extrapolate the database results to D_{max} values of 15 mm, but the results of certain ice habit models should be used cautiously under such circumstances and will be noted throughout this study. Note that a few select habits (e.g., spheres, LSS, and LDS) already have optical properties calculated up to D_{max} values of 10-15 mm, so little extrapolation is required for these particle models. Additionally, the L04 results have been updated in Liu (2008b) to include larger D_{max} ranges for many of the ice particle models that would reduce the need to extrapolate to larger particle sizes. The Liu (2008b) results are not currently incorporated into the database used in this study, but will be included in future work.

c. Optical properties

Since the optical properties of the various ice particle models have been reported in previously published studies, only a cursory inspection is provided in this section. Fig. 3.4 depicts DDA- and Mie-derived optical properties at 150 GHz – a high frequency microwave window channel sensitive to scattering from frozen hydrometeors. The optical properties shown are the extinction cross-section (σ_e ; in units of $[m^2]$), single scatter albedo (ω_o), and asymmetry parameter (g). The single scatter albedo is defined as:

$$\omega_o = \frac{\sigma_s}{\sigma_e}, \quad (3.2)$$

where σ_s is the particle scattering cross-section, and thus quantifies the relative contribution of scattering versus absorption by a frozen particle at a given particle size and frequency (e.g., a ω_o of unity indicates pure scattering). The asymmetry factor is the mean cosine of the scattering angle integrated over the entire scattering phase function and is defined as:

$$g = \frac{1}{4\pi} \int_{4\pi} p(\cos\Theta) \cos\Theta d\omega, \quad (3.3)$$

where Θ is the scattering angle, $p(\cos\Theta)$ the scattering phase function, and $d\omega$ the solid angle integration increment. An asymmetry factor near 1 (-1) indicates strong forward (backward) scattering, while a value of zero represents isotropic scattering.

The σ_e results shown in Fig. 3.4 highlight the often expansive differences between ice particle models for a given particle size that can exceed many orders of magnitude at the larger particle sizes and can lead to different simulated microwave brightness temperatures. Note also the universally large increase in ω_o as D_{max} increases, with all particles containing ω_o values exceeding 0.9 – indicating the dominance of scattering versus absorption – at the largest particle sizes. Even though all particles trend toward higher values of ω_o with increasing D_{max} , considerable spread between the ice habits is evident. Similar to the ω_o results, values of g increase abruptly when D_{max} is larger than about 0.5 mm for most particles. Note, however, the wide disparity in asymmetry factors ranging between 0.2 and 0.9 above D_{max} values exceeding ~ 1.0 mm for the various ice particle models that highlight large differences in the dominant scattering direction for each habit.

Using D_{max} as the independent variable for illustrating the optical properties in Fig. 3.4 can be somewhat misleading, however, as the effective densities of the ice particle models can vary dramatically, and a given D_{max} value does not correspond to an equal mass for all of the particles. The mass (m) – D_{max} relationships for the various ice particle models are described by the following power-law relationship:

$$m(D_{\max}) = aD_{\max}^b, \quad (3.4)$$

where the coefficient a and exponent b for each ice particle model are shown in Table 3.2. The α and γ columns in Table 3.2 correspond to particle fall speed- D_{\max} relationships used to calculate snowfall rates and will be discussed in greater detail in following sections. Fig. 3.5a displays the m - D_{\max} relationships for the entire ice particle database and highlights the large difference in respective particle masses for a given D_{\max} value. Note also the “AGG” category shown in Fig. 3.5 with corresponding a and b values derived from previously published observational studies of unrimed aggregate snowflakes (Locatelli and Hobbs 1974; Mitchell 1996; Wilson and Ballard 1999; Heymsfield et al. 2004; Mitchell and Heymsfield 2005). Fig. 3.5b shows a subset of m - D_{\max} relationships for the HR6, LR6, and KR6 ice particle models, and the differences between these six-arm/bullet-rosette models will be highlighted later in this section. Fig. 3.6 depicts the optical properties as a function of particle mass and is directly analogous to Fig. 3.4. The σ_e per unit mass results show large variations for a given particle mass – similar to the D_{\max} results. Note, however, the extreme outliers (e.g., spherical hail, graupel and some non-spherical plates/columns) that are accentuated when displayed as a function of particle mass. The ω_o and g results generally show reduced spread between the ice particle models when plotted as a function of mass instead of D_{\max} , but the g results still diverge considerably at the largest particle masses.

Ice particle backscatter properties are required to calculate the radar reflectivity factor for active microwave remote sensing applications. Backscatter cross-sections for all of the ice particle models in the database for the 35 and 94 GHz frequencies are shown in Fig. 3.7. These two frequencies are especially relevant for active space-borne microwave instruments, as the GPM DPR will have one of two channels operating near 35 GHz, while CloudSat's CPR currently operates at 94 GHz, and future proposed space-borne radars (e.g., EarthCARE, ACE) will also feature 94 GHz capabilities. Like the previous optical properties shown in Fig. 3.4, there is considerable variability in the backscatter properties of the respective ice particle models, with the range of backscatter cross-sections for a given D_{max} value varying by three to four orders of magnitude (Fig. 3.7a and Fig. 3.7b). Another perspective of the backscatter properties is offered in Fig. 3.7c and Fig. 3.7d which show the backscatter efficiency ($Q_{b, eff}$) as a function of size parameter (x). The backscatter efficiency is defined as:

$$Q_{b, eff} = \frac{\sigma_b}{\pi r_e^2}, \quad (3.5)$$

where σ_b is the backscatter cross-section and r_e the equivalent particle radius. Note the considerable differences in backscatter efficiency at size parameters below about 0.5 and the Mie-related resonant features associated with spherical models at both frequencies. The spherical models also have consistently lower backscatter efficiencies than the DDA-generated results associated with the non-spherical ice habits, and the implications of the

different backscatter properties between spherical and non-spherical habits will be discussed in later sections.

Since few direct comparisons between different DDA-based results have been published to date, Fig. 3.8 illustrates extinction and backscatter cross-sections for three similarly shaped habits from the ice particle model database – the six bullet rosette from L04 and H07 (denoted as LR6 and HR6, respectively) and the 6-arm rosette from K07 (KR6). The snow fluffy sphere (FS) is also indicated for reference. From casual inspection of these ice particle models in Fig. 3.1 through Fig. 3.3, large differences in optical properties for these habits might not be anticipated. The extinction and backscatter properties, however, widely diverge at larger particle sizes. All rosette models compare reasonably well at smaller particle masses, but the KR6 has a much larger extinction cross-section per unit mass when the particle mass exceeds about 0.1 mg. Differences are also evident in the backscatter cross-section versus D_{max} plot shown in Fig. 3.8, and the KR6 shape again displays consistently higher values. Note, however, the extremely low backscatter cross-section per unit mass for the KR6 shape versus the LR6 and HR6 habits. The only noteworthy superficial difference between the rosette models that could cause such different optical properties is the “bullet” shape of the LR6 and HR6 appendages versus the cylindrical structure of the KR6 arms. A more important underlying difference between each respective model is the assumed aspect ratio (i.e., the ratio between diameter and length of each rosette appendage) used to construct the respective ice particle models that can also affect their inherent scattering properties. Another potential source of these differences could be the assumed temperature used to

derive the particles' optical properties. Both the KR6 and LR6 habits assume a temperature of -15 C, while the HR6 optical properties were derived using a temperature of -30 C. K07, however, indicates a minimal temperature dependency of less than 1% for DDA-derived scattering properties due to temperature-dependent dielectric constant variations, and L04 reports a 0.2% variation in scattering properties between 0 and -20 C, so temperature effects are most likely a negligible contributing factor to the differences between these habits. The implications of these differences in the optical properties between ice models will be discussed in greater detail in subsequent sections.

Table 3.1: Ice particle model habits and abbreviations from the DDA results of Hong (2007), Kim et al. (2007), and Liu (2008). Surrussavadee and Staelin (2006; SS06) frequency-dependent soft spheres and three variable-density fluffy spheres for snow, graupel, and hail are also indicated. The range of maximum particle dimension (D_{max}) and equivalent particle radii (R_e) from these studies are also indicated.

Database	Shape #	Habit	Abbreviation	D_{max} (μm)	R_e (μm)
Hong (2007)	1	Hex Column	HC1	100-5500	42-610
Hong (2007)	2	Hollow Hex Column	HC2	100-5500	40-574
Hong (2007)	3	Hex Plate	HP	100-5500	29-793
Hong (2007)	4	6-Bullet Rosette	HR6	100-5500	27-625
Hong (2007)	5	Aggregate	HA	100-5500	26-1416.
Hong (2007)	6	Droxtal	HD	100-5500	45-2469
Liu (2004)	7	Long Hex Column	LC1	242-3626	55-771
Liu (2004)	8	Short Hex Column	LC2	166-2477	56-772
Liu (2004)	9	Block Hex Column	LC3	132-1974	55-766
Liu (2004)	10	Thick Hex Plate	LP1	163-2434	57-767
Liu (2004)	11	Thin Hex Plate	LP2	253-3794	53-769
Liu (2004)	12	3-Bullet Rosette	LR3	100-5000	30-666
Liu (2004)	13	4-Bullet Rosette	LR4	100-5000	37-591
Liu (2004)	14	5-Bullet Rosette	LR5	100-5000	40-635
Liu (2004)	15	6-Bullet Rosette	LR6	100-5000	42-674
Liu (2004)	16	Sector Snowflake	LSS	50-10000	61-502
Liu (2004)	17	Dendrite Snowflake	LDS	75-12453	40-506
Kim (2007)	18	Hex Column	KC	60-3000	23-590
Kim (2007)	19	4-Bullet Rosette	KR4	60-3000	29-766
Kim (2007)	20	6-Bullet Rosette	KR6	60-3000	33-875
SS06*	21	Snow (sphere)	SS	100-15000	30-2968
SS06*	22	Graupel (sphere)	SG	100-15000	23-2251
Snow	23	Snow (sphere)	FS	100-15000	24-2389
Graupel	24	Graupel (sphere)	FG	100-15000	38-3791
Hail	25	Hail (sphere)	FH	100-15000	50-4969

Table 3.2: Coefficients and exponents for mass-particle size (Eq. 3.4) and fall speed-particle size (Eq. 4.3) relationships. SI units are assumed. References for the fall speed-particle relationships are indicated in the footnotes below.

Habit	a	b	α	γ
HC1	0.03	2.00	22.36 [@]	0.48
HC2	0.02	2.00	22.36 [@]	0.48
HP	0.75	2.47	155.87 [#]	0.86
HR6	0.18	2.34	8.83 [%]	0.36
HA	65.45	3.00	8.83 [%]	0.36
HD	347.31	3.00	369.97 [*]	0.89
LC1	37.09	3.00	22.36 [@]	0.48
LC2	116.12	3.00	22.36 [@]	0.48
LC3	229.66	3.00	22.36 [@]	0.48
LP1	122.66	3.00	155.87 [#]	0.86
LP2	32.36	3.00	155.87 [#]	0.86
LR3	0.32	2.37	8.83 [%]	0.36
LR4	0.06	2.12	8.83 [%]	0.36
LR5	0.07	2.12	8.83 [%]	0.36
LR6	0.09	2.13	8.83 [%]	0.36
LSS	0.002	1.58	79.21 ^{##}	0.81
LDS	0.01	1.90	5.02 ^{&}	0.48
KC	14.19	2.88	22.36 [@]	0.48
KR4	32.30	2.88	8.83 [%]	0.36
KR6	47.45	2.88	8.83 [%]	0.36
SS	3.69	3.00	8.83 [%]	0.36
SG	19.34	3.00	369.97 [*]	0.89
FS	5.26	3.00	8.83 [%]	0.36
FG	84.09	3.00	369.97 [*]	0.89
FH	425.71	3.00	369.97 [*]	0.89
AGG	.034	1.95	8.83 [%]	0.36

[@] Mitchell (1996) columns

[#] Heymsfield and Kajikawa (1987) hexagonal plate

[%] Best-fit aggregate properties. See Fig. 4.2.

^{*} Heymsfield and Kajikawa (1987) graupel

^{##} Heymsfield and Kajikawa (1987) plate with sector-like branches

[&] Heymsfield and Kajikawa (1987) dendrite

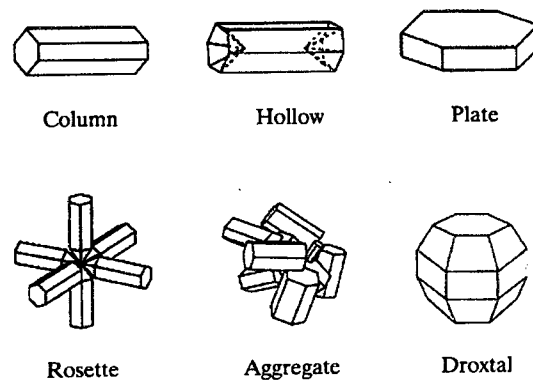


Fig. 3.1: Ice particle model shapes from Hong (2007; Fig. 1).

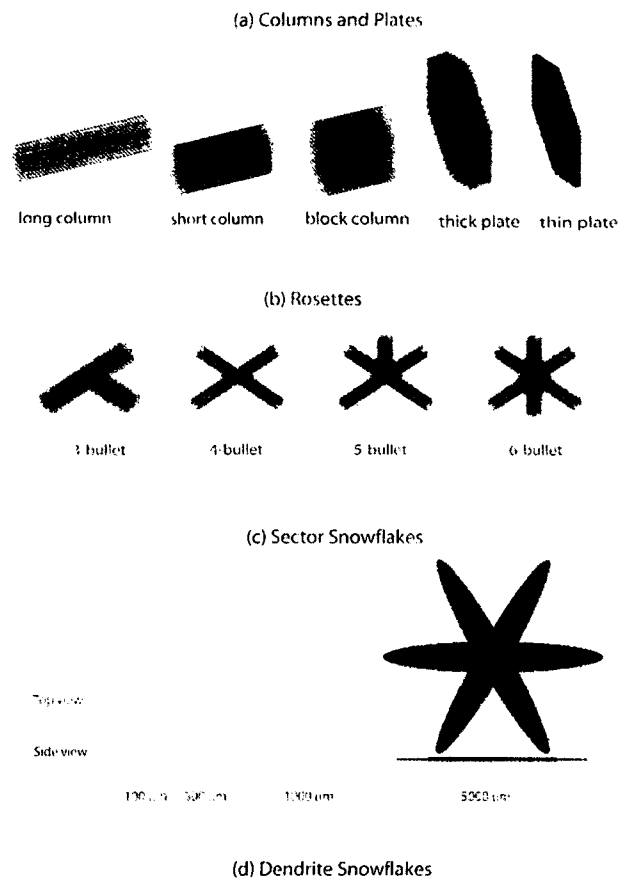


Fig. 3.2: Ice particle model shapes from Liu (2004; Fig. 1).

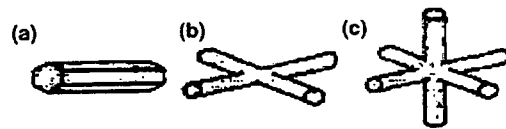


Fig. 3.3: Ice particle model shapes from Kim et al. (2007; Fig. 1)

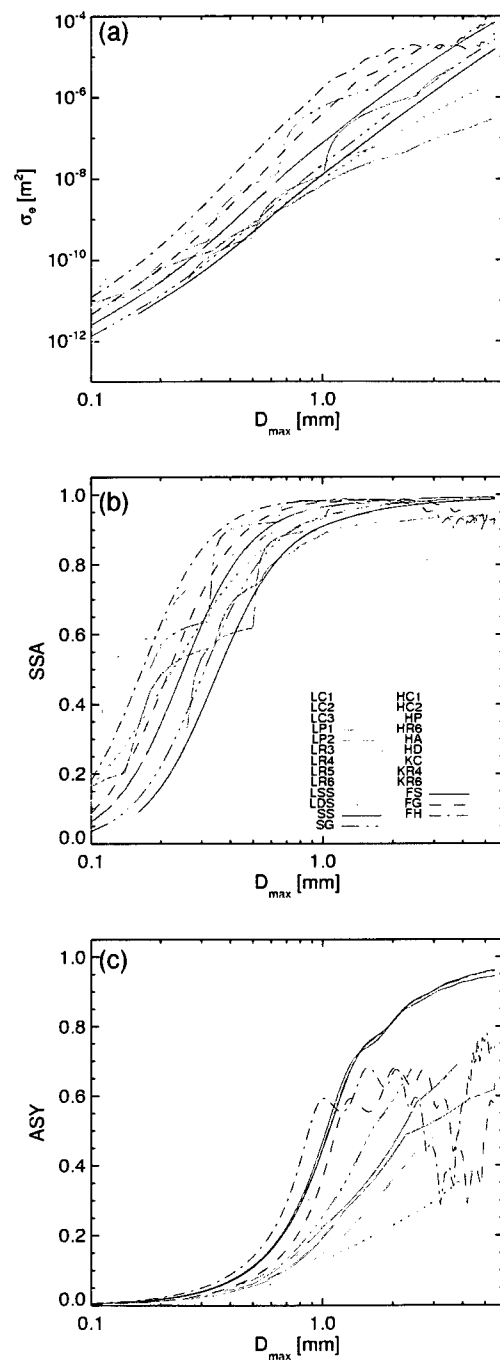


Fig. 3.4: 150 GHz optical properties for the ice particle models in Table 3.1. The following optical properties are shown: (a) extinction cross-section, (b) single scatter albedo, and (c) asymmetry parameter.

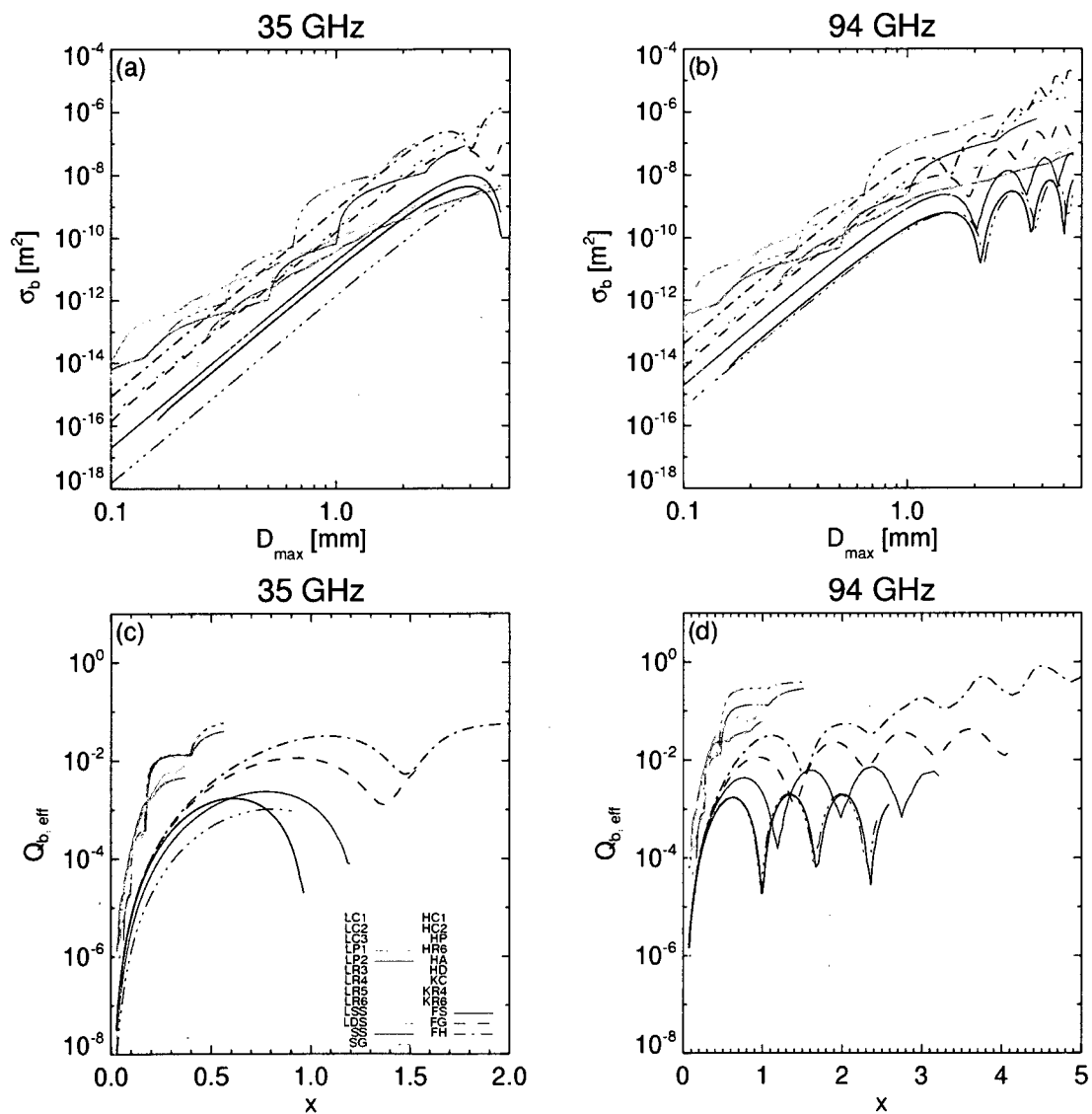


Fig. 3.7: Backscatter cross-section (σ_b) and backscatter efficiency ($Q_{b, \text{eff}}$) for the ice particle models in Table 3.1 for 35 and 94 GHz.

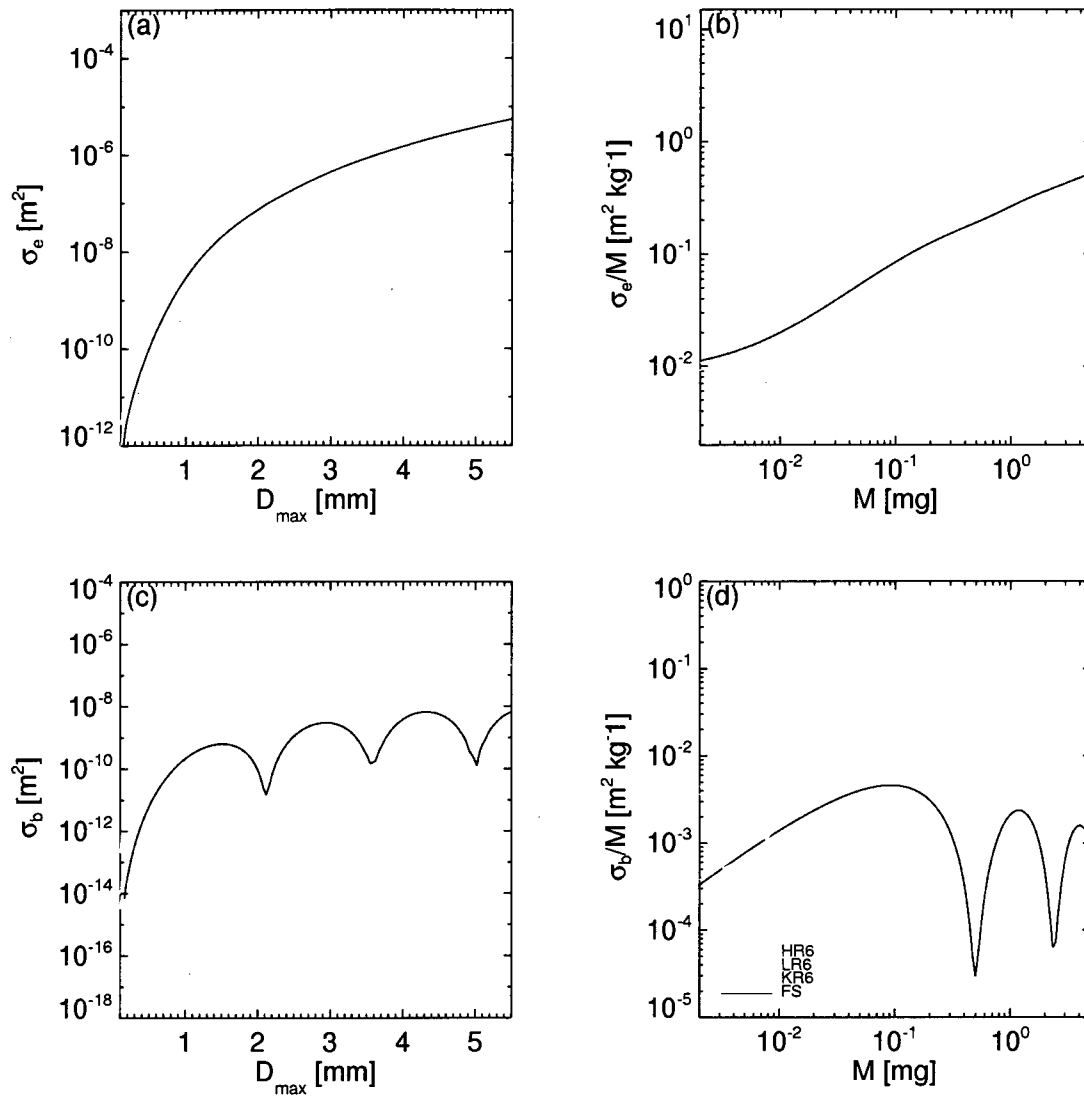


Fig. 3.8: Panels (a) and (b) respectively illustrate extinction cross-section (σ_e) and σ_e per unit mass at 150 GHz for the six-bullet/arm shapes from Liu (2004), Hong (2007), and Kim et al. (2007). Panels (c) and (d) respectively illustrate backscatter cross-section (σ_b) and σ_b per unit mass at 94 GHz for the same shapes in Panels (a) and (b).

4. Particle Size Distribution

a. Exponential PSD

Representing the particle size distribution (PSD) of frozen hydrometeors is another complicating factor associated with active and passive microwave remote sensing of precipitation, especially given the relative scarcity of such observations and the demonstrated sensitivity of microwave optical properties to underlying differences in the PSD (e.g., Bennartz and Petty 2001). Frozen PSD's have commonly been described in terms of an exponential form analogous to the Marshall and Palmer (1948) rainfall PSD, written in the form of:

$$N(D_l) = N_o \exp(-\Lambda D_l), \quad (4.1)$$

where $N(D_l)$ is the number of frozen particles with a liquid-equivalent diameter (D_l) in a given size bin per unit volume, N_o is the intercept parameter, and Λ the slope parameter. One of the most widely utilized ice PSD parameterizations was reported by Sekhon and Srivastava (1970; hereinafter SS70). As demonstrated by SS70, both N_o and Λ are functions of snowfall rate, although both parameters are often assumed to be invariant for a defined frozen particle type for cloud modeling purposes or have built-in temperature or height dependencies to model their vertical variability (e.g., Wilson and Ballard 1999; Ryan 2000; Woods et al. 2008).

Braham (1990; hereinafter B90) reported PSD results in terms of maximum particle dimension (D_{max}) from in-situ measurements of lake-effect snowfall events in the Great Lakes region and also documented an exponential size distribution for frozen particles with D_{max} larger than ~ 1 mm. The PSD's resulting from the intercept and slope parameters published by the B90 observations are shown in Fig. 4.1. The PSD's exhibit different properties based on relative snowfall intensity, with higher snowfall rates generally displaying larger N_o and smaller Λ values. The B90 N_o and Λ values are further partitioned into the following five snowfall rate bins (0.05, 0.1, 0.5, 1.0, and 1.5 mm h⁻¹) spanning the snowfall intensity spectrum¹ and correspond to the five additional thick PSD lines overlaid on Fig. 4.1. The five snowfall rate categories are analogous to B90's light, moderate, and heavy snowfall cases (B90 Figs. 3 through 5, respectively). The snowfall rates (liquid equivalent) are calculated using the following expression:

$$S = \rho_l^{-1} \int m(D_{max})v(D_{max})N(D_{max})dD_{max}, \quad (4.2)$$

where ρ_l is the density of liquid water, $m(D_{max})$ and $v(D_{max})$ are the size-dependent particle mass and fall speed, respectively, and $N(D_{max})dD_{max}$ is the particle concentration (in this case, calculated using the B90 observations) within a size interval defined by D_{max} to $D_{max} + dD_{max}$. As shown in Fig. 4.2, there are a variety of previously published m - D_{max} and fall speed-particle size (v - D_{max}) relationships for aggregate snowflakes. Eq. 3.4

¹ Assuming a 15:1 snow-to-liquid equivalent ratio – which is not unreasonable for lake-effect snow – for a 1.5 mm h⁻¹ snowfall rate yields ~ 23 mm (.9 inches) of snowfall accumulation in one hour.

provided the power-law equation for $m-D_{max}$, while the following equation is used to describe the $v-D_{max}$ relationship:

$$v(D_{max}) = \alpha D_{max}^{\gamma}, \quad (4.3)$$

where the particle fall speed and mass in Eqs. 3.4 and 4.3 are provided in SI units. A least-squares fit of the various $m-D_{max}$ and $v-D_{max}$ relationships (Locatelli and Hobbs 1974; Heymsfield and Kajikawa 1987; Mitchell 1996; Wilson and Ballard 1999; Heymsfield et al. 2004; Mitchell and Heymsfield 2005) is adopted to describe the mass and fall speed of aggregate snowflakes and is indicated by the solid line shown in Fig. 4.2, where the prefactors and exponents in Eqs. (3.4) and (4.3) of these best fit lines are $a = 0.033608$, $b = 1.95226$, $\alpha = 8.83486$, and $\gamma = 0.358411$, respectively. As shown in Fig. 4.3, the derived snowfall rates for the 49 B90 snowfall events are extremely sensitive to the assumed $m-D_{max}/v-D_{max}$ relationships and can vary by over 50% from the best-fit line if the upper and lower bounding $m-D_{max}/v-D_{max}$ relationships are used. Therefore, appropriate caveats must be highlighted when computing snowfall rates – or any other quantity that depends on mass and fall speed relationships – due to the potentially large source of uncertainties associated with such calculations.

b. Field et al. (2005, 2007) PSD

Even though the findings of SS70 and B90 were limited to near-surface observations – and also restricted to shallow, convective lake effect snowfall events in B90 – numerous studies utilizing airborne observations of large scale synoptic weather systems have confirmed the ubiquitous existence of exponential frozen PSD's for larger particle sizes (e.g., Houze et al. 1979; Lo and Passarelli 1982; Field et al. 2005, 2007). There is also overwhelming evidence in all of the aforementioned studies – plus other independent studies (e.g., Gordon and Marwitz 1984; Herzegh and Hobbs 1985; Mitchell 1991; Platt 1997) – of noticeably higher particle concentrations and an accompanying slope increase in the ice PSD at smaller particle sizes. The existence of such “super-exponential” ice particle concentrations is usually ignored in most microwave remote sensing studies of precipitation, as the largest particles described by the exponential distributions usually play a dominant role in the signal ultimately measured by the remote sensing instruments. However, subtleties in the shape of the PSD at the lower end may play a crucial role in correctly deciphering the signal received by sensors like CloudSat that are very sensitive to smaller frozen particles, have an extremely low minimum detectable signal (near -30 dBZ_e), and are well-suited to study lighter snowfall events with an appreciable contribution from smaller particles. A relatively new ice PSD parameterization developed by Field et al. (2005; hereinafter F05), and an updated version by Field et al. (2007; hereinafter F07), more realistically accounts for both the narrow particle concentration peak at smaller particle sizes and the inherent temperature-dependency of observed PSD's.

To explore the sensitivity of modeled radar reflectivity factor on the choice of ice PSD, the F05 and F07 parameterizations are employed as viable alternatives to a strictly exponential PSD. The F05 results are based on aircraft observations of frozen particles in stratiform clouds near the United Kingdom and provide a physically realistic method to conveniently relate any two moments of the ice PSD via the following temperature-dependent power law relationship:

$$M_n = a_F(n, T_c) M_2^{b_F(n, T_c)}, \quad (4.4)$$

where M_n represents any arbitrary “ n^{th} ” moment of the PSD, e.g.,

$$M_n = \int D^n N(D) dD, \quad (4.5)$$

M_2 is the reference second moment of the frozen PSD, T_c is the temperature (C), and a_F and b_F are temperature- and moment-dependent parameters based on curve fits relating the second moment of the PSD to other moments (e.g., Table 2 in F05). (Note the subscript denoting maximum particle dimension has been eliminated from Eq. 4.5, and any reference to “ D ” in the PSD will henceforth imply maximum particle dimension unless specifically noted otherwise.) The PSD power law curve fits follow a steeply-sloped exponential distribution at the smallest particle sizes in the F05 parameterization, then transitions to a gamma distribution at larger particle sizes.

The F07 parameterization is similar to F05, but uses a different observational dataset as its basis and presents results for both mid-latitude (based on observations from the United States southern Great Plains) and tropical (based on observations from the Marshall Islands and Florida) environments in an attempt to extend their parameterization globally. The F07 moment relationships are based on the following equation:

$$M_n = a_{F07}(n) \exp[b_{F07}(n)T_c] M_2^{c_{F07}(n)}, \quad (4.6)$$

where the a_{F07} , b_{F07} , and c_{F07} parameters are solely functions of the moment number n (see F07 Table 3). It should be noted that the F05/F07 parameterizations are only valid for particle sizes larger than $100 \mu\text{m}$ due to measuring uncertainties for smaller particle sizes, and SI units are assumed when using Eqs. 4.4 and 4.6.

If a specific moment of the PSD is known a priori, Eqs. 4.4 and 4.6 can be inverted to obtain M_2 . Once M_2 is known, any other moment of the PSD, or the PSD itself (as will be illustrated momentarily), can be derived. The F05/F07 parameterizations are utilized as follows in this study:

1. The moment of the ice PSD defining the snowfall rate (S) or ice water content (IWC) is calculated. For instance, by solving for the integrand in the equation defining snowfall rate (Eq. 4.2) and applying the m - D_{max} (Eq. 3.4) and v - D_{max} (Eq. 4.3) relationships shown in Table 3.2 for a particular ice particle model, the following expression for the “ $b+\gamma$ ” moment of the PSD is obtained:

$$M_{b+\gamma} = \int D^{b+\gamma} N(D) dD = \frac{\rho_i S}{a\alpha}. \quad (4.7)$$

When possible, using IWC is preferable to snowfall rate since it does not depend on the particle fall speed, e.g.,

$$IWC = \int m(D) N(D) dD. \quad (4.8)$$

A similar relationship as Eq. 4.7 can be written for the “ b ” moment of the PSD defining the IWC by applying the m - D_{max} relationships (Eq. 3.4) and solving for the integrand in Eq. 4.8:

$$M_b = \int D^b N(D) dD = \frac{IWC}{a}. \quad (4.9)$$

2. The reference second moment of the ice PSD can then be obtained by inverting the moment relationships from Eqs. 4.4 or 4.6.
3. Any other moment of the ice PSD can then be calculated via the reference second moment and Eqs. 4.4 or 4.6.
4. The actual PSD can be derived using the second and third moments of the PSD from steps 2 and 3 above (see Section 4c). Other PSD-dependent quantities (e.g.,

reflectivity, PSD-averaged extinction coefficient, etc.) can then be calculated using the PSD and optical properties from the database described in Section 3.

c. Deriving the PSD

Lee et al. (2004) present the following generalized scaling function that characterizes the ice particle concentration $N(D)$ via any two moments of the PSD:

$$N(D) = M_i^{(j+1)/(j-1)} M_j^{(i+1)/(i-1)} \phi_{ij}(x), \quad (4.10)$$

where M_i and M_j represent the two chosen moments of the PSD, $\phi_{ij}(x)$ is a universal scaling function, and x is the dimensionless particle size, where

$$\phi_{ij}(x) = \kappa_o \exp(-\Lambda_o x) + \kappa_1 x^v \exp(-\Lambda_1 x), \quad (4.11)$$

and

$$x = D \left(\frac{M_i}{M_j} \right)^{1/(j-i)}. \quad (4.12)$$

The Λ and ν terms in Eq. 4.11 are PSD shape parameters reflecting the combination of exponential and gamma size distributions of observed frozen particles (e.g., Westbrook et al. 2004 a,b). By using the second and third moments of the PSD, F05 calculated optimal fits for these shape parameters such that Eq. 4.11 can be written as

$$\phi_{23}(x) = 490.6 \exp(-20.78x) + 17.46x^{0.6357} \exp(-3.29x), \quad (4.13)$$

while F07's expression for $\phi_{23}(x)$ is

$$\phi_{23}(x) = 141 \exp(-16.8x) + 102x^{2.07} \exp(-4.82x), \quad (4.14)$$

Eq. 4.14 is valid only for the mid-latitudes. A version of Eq. 4.14 is also available from F07 for the tropics, but will not be considered here since this study focuses on higher latitude applications. The value of x in Eqs. 4.13 and 4.14 comes directly from Eq. 4.12, which reduces to the following expression when using the second and third moments of the PSD:

$$x = D \left(\frac{M_2}{M_3} \right), \quad (4.15)$$

Therefore, the Eq. 4.10 can be written in its final form as

$$N(D) = \phi_{23} \left(\frac{M_2^4}{M_3^3} \right). \quad (4.16)$$

d. PSD examples

Sample ice PSD's derived from the F05 parameterization for two different assumed IWC's are displayed in Fig. 4.4. The temperature dependency of the derived PSD's for a given IWC is an obvious feature. Note the steep reduction in particle concentrations at larger particle sizes as temperature decreases for all of the IWC's shown. For instance, the largest particle size predicted by the F05 scheme for an input IWC of 0.1 g m^{-3} decreases from $\sim 6 \text{ mm}$ (-2.5 C) to less than 2 mm (-42.5 C). Further inspection of Fig. 4.4 reveals elevated particle number concentrations at larger particle sizes for the 1.0 g m^{-3} IWC case compared to the 0.1 g m^{-3} IWC results, thus reflecting the prevalence of larger particles associated with higher IWC levels. The large variation between derived PSD's at warmer versus colder temperatures, especially for the 1.0 g m^{-3} case, hints at possible ramifications for quantities that intimately depend on the PSD (e.g., radar reflectivity factor and PSD-averaged optical properties averaged).

The derived PSD also strongly depends on the properties of the assumed ice particle model (Fig. 4.5). The variations in the PSD's indicated in Fig. 4.5 are due entirely to the m - D_{max} relationships used to derive the PSD (Section 4b). For a given input IWC or snowfall rate, the F05 moment conversion scheme automatically adjusts the

predicted PSD so heavier particles for a given D_{max} (e.g., HD and LP1) predict smaller overall particle sizes, while lighter particles (e.g., HR6 and LDS) possess much larger particles since each particle's $m-D_{max}$ relationship (Table 3.2) defines a different input moment of the PSD. The PSD derived using the average aggregate (AGG) particle properties (Fig. 4.2) is also overlaid in Fig. 4.5 for reference, and implications of the derived PSD's will be discussed in later sections.

Fig. 4.6 highlights the differences between PSD's derived for different snowfall rates using the F05/F07 methods and the B90 exponential distribution for lighter (0.1 mm h^{-1}) and heavier (1.0 mm h^{-1}) snowfall rates. The F05 parameterization is adopted as the baseline, default PSD throughout the remainder of this study, but the F07 and B90 PSD's will be utilized in the next section to illustrate the potential uncertainty associated with calculated radar reflectivity factor. In addition to the noticeable temperature-dependent features of F05/F07-derived PSD's, a few other prominent trends are apparent in Fig. 4.6 when comparing the various PSD's. First, the distinctive peak in F05/F07 particle concentrations at smaller particle sizes does not occur in the B90 particle concentrations at the smallest particle sizes. The B90 PSD contains particle concentration deficits one to two orders of magnitude less than the F05/F07 results depending on the snowfall rate and temperature. Conversely, the B90 exponential PSD also tends to overestimate the particle concentrations at larger particle sizes relative to the F05/F07 results, and this feature is especially accentuated at the lowest snowfall rates. A noticeable exception to this trend is the F05 -2.5 C results that compare very favorably with the B90 exponential PSD at D_{max} values greater than about $\sim 1 \text{ mm}$.

The F05 versus F07 parameterization differences also warrant some discussion (recall that these schemes are based on two different observational datasets). The variation between F05 and F07 is generally not significant at the smallest snowfall rates, smallest particle sizes, and lowest temperatures shown in Fig. 4.6, but substantial discrepancies are evident at larger particle sizes and snowfall rates. For instance, the -2.5 C F07 PSD for an assumed snowfall rate of 1.0 mm h^{-1} exhibits noticeably larger particle concentrations than F05 in a critical region located between $0.5 < D_{max} < 2.0 \text{ mm}$. This region exists at lower snowfall rates as well, but the magnitude of the differences and the extent of the region both get progressively more expansive as the snowfall rate increases. This behavior, however, reverses at the largest particle sizes ($D_{max} > 2.0 \text{ mm}$) for the heavier snowfall rate case, as F05 shows increasingly larger particle concentrations compared to F07. Differences between F05 and F07 are generally not as expansive for the lighter snowfall rate case.

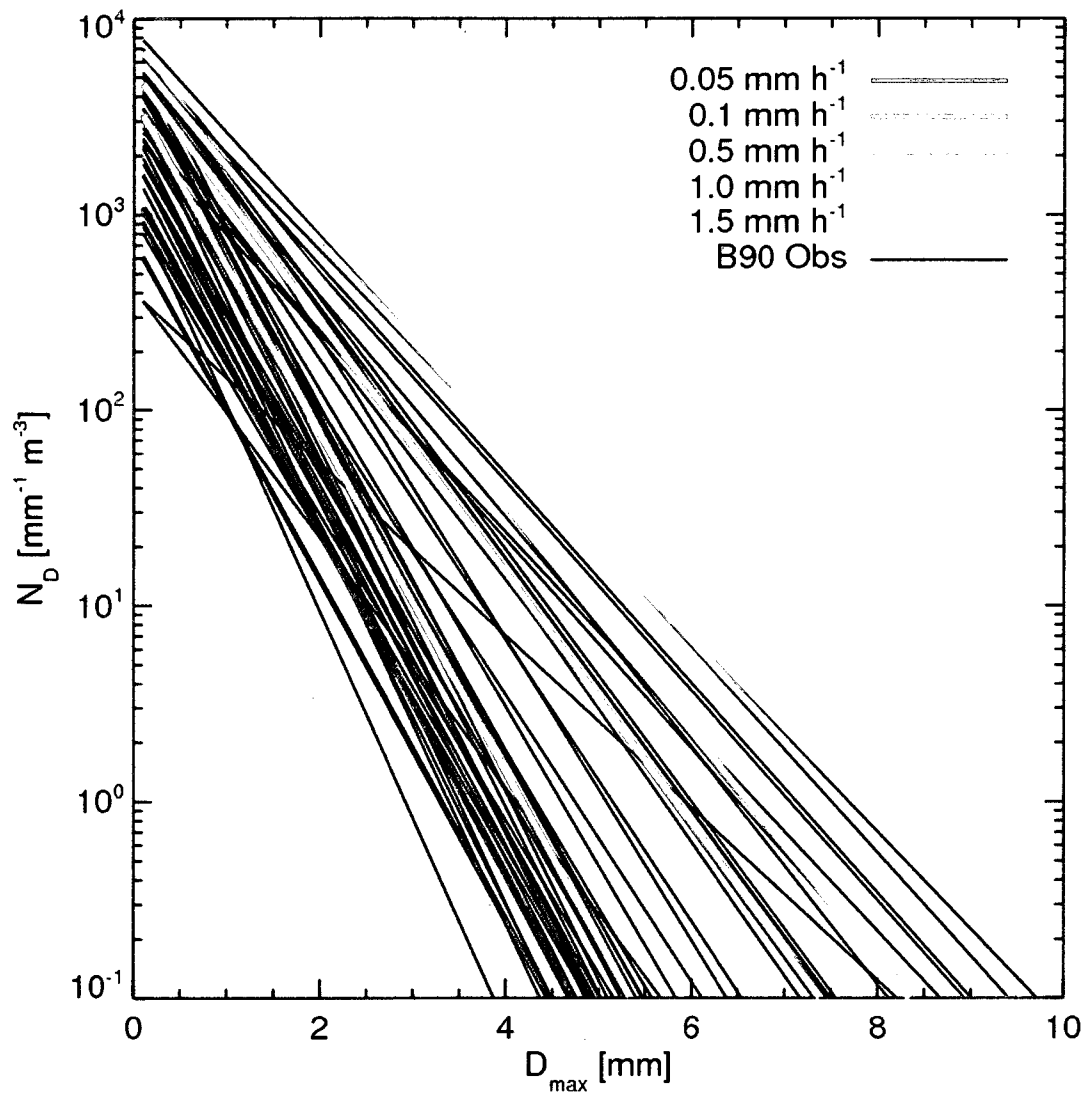


Fig. 4.1: Frozen particle size distributions from the observations of Braham (1990), adapted from Matrosov (2007). Colored lines indicate average results for the snowfall rates indicated.

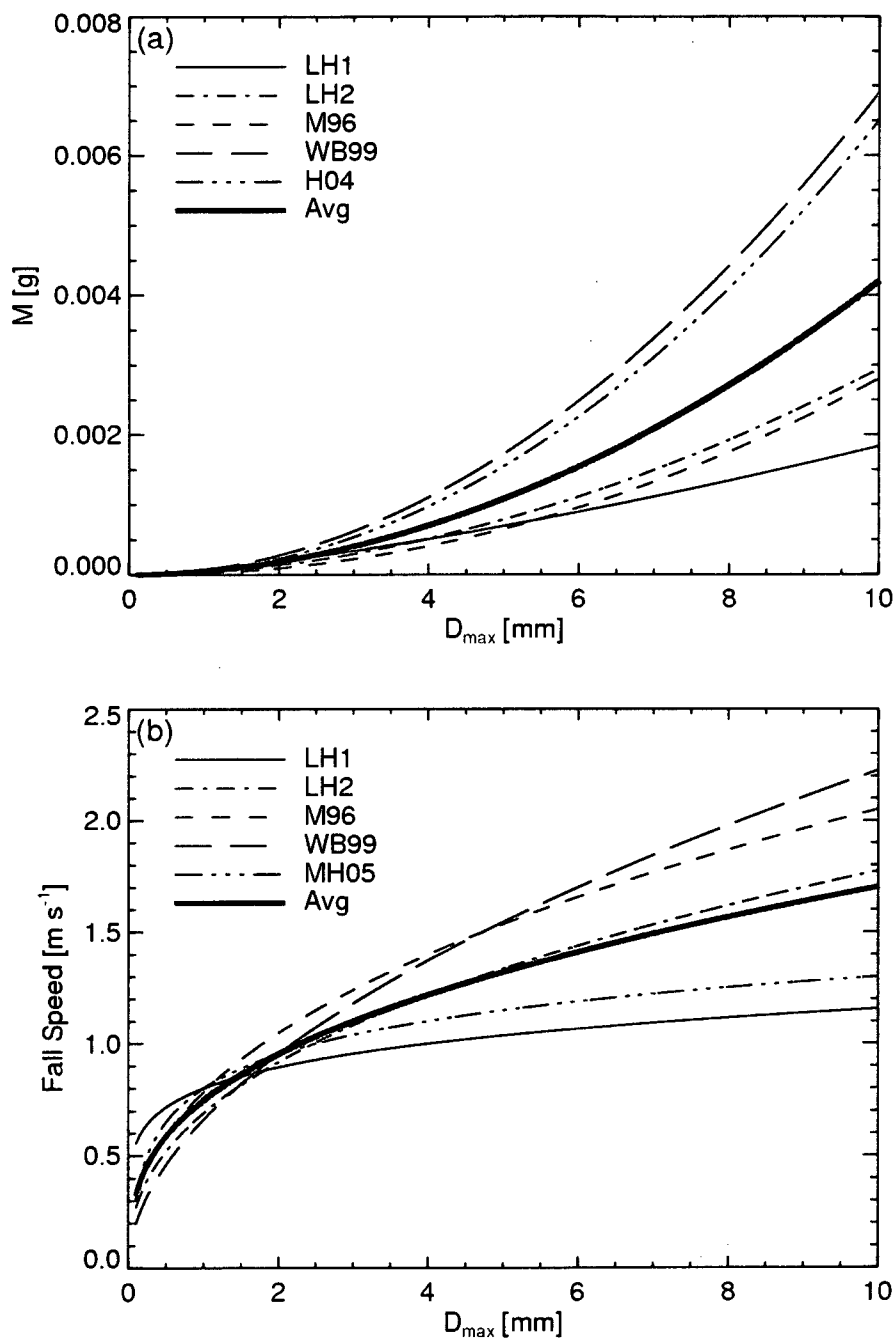


Fig. 4.2 (a) Mass-size and (b) fall speed-size relationships of aggregates from various studies. Shapes indicated include aggregates of unrimed radiating assemblages of dendrites (LH1) and unrimed radiating assemblages of plates, side planes, bullets, and columns (LH2) from Locatelli and Hobbs (1974), and other aggregates from Mitchell (1996; M96), Heymsfield et al. (2004; H04), Mitchell and Heymsfield (2005), and Wilson and Ballard (1999; WB99). The best fit mass/fall speed-size relationships derived from all of these studies is indicated by the thick, solid line (AVG).

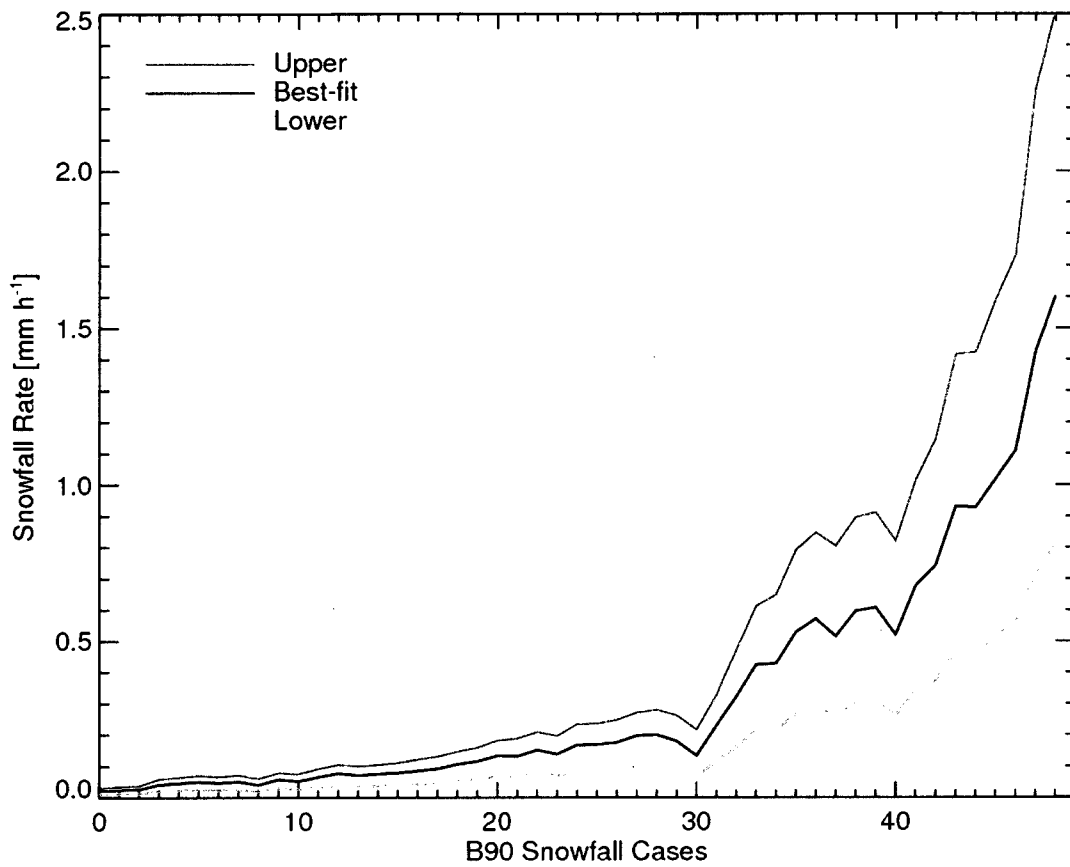


Fig. 4.3: Derived snowfall rates for the 49 Braham (1990) cases using the best-fit mass-size ($m-D_{max}$) and fall speed-size ($v-D_{max}$) relationships from Fig. 4.2 (Best-fit). Derived snowfall rates using the upper and lower limit $m-D_{max}$ and $v-D_{max}$ relationships in Fig. 4.2 are also indicated.

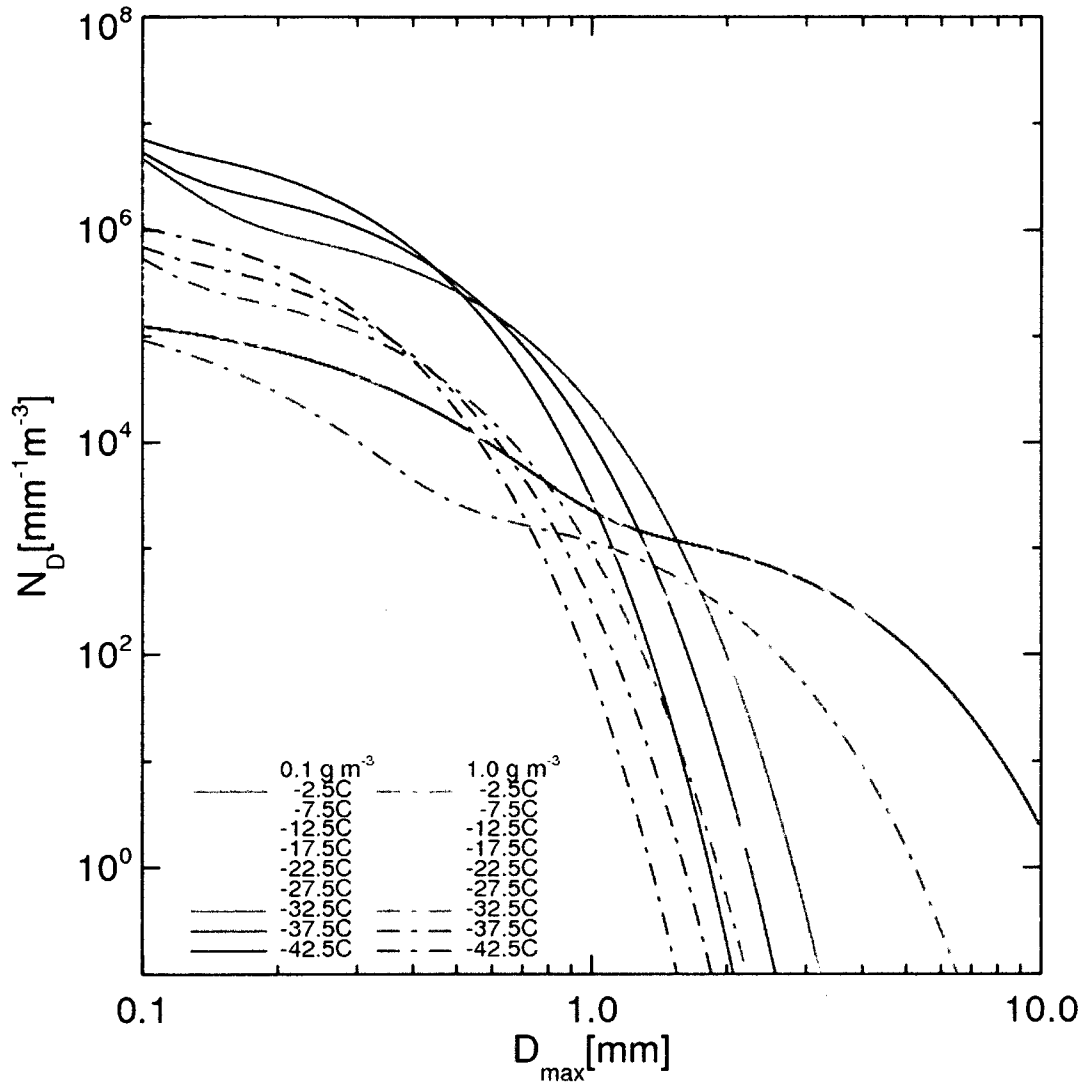


Fig. 4.4: Sample ice particle size distributions derived using the Field et al. (2005) parameterization assuming the LR6 shape and an input ice water content of 1.0 (solid) and 0.1 g m^{-3} (dash-dot) at different temperatures (colored lines).

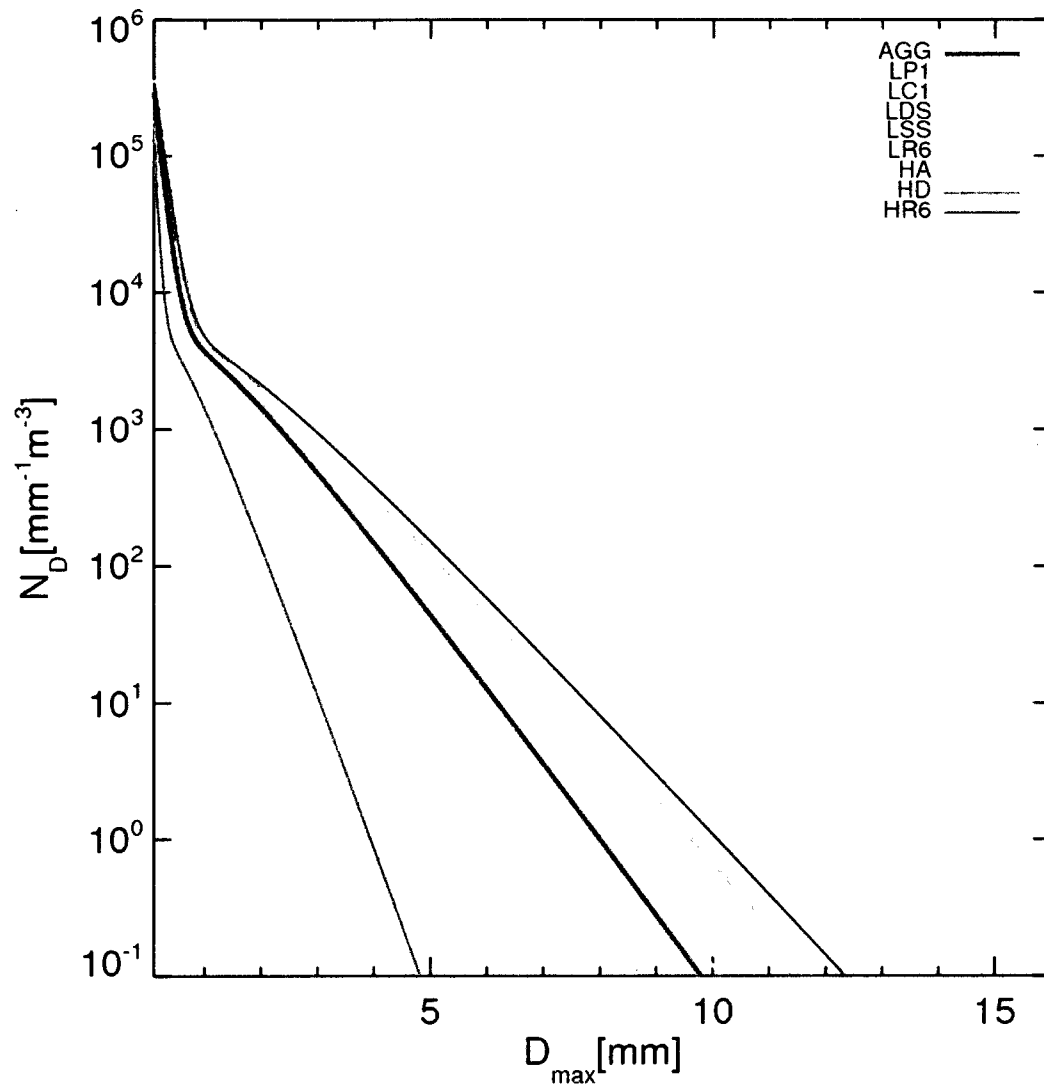


Fig. 4.5: Derived ice particle size distributions using the Field et al. (2005) parameterization for various ice models (see Table 3.1 for abbreviations) assuming an ice water content of 1.0 g m^{-3} .

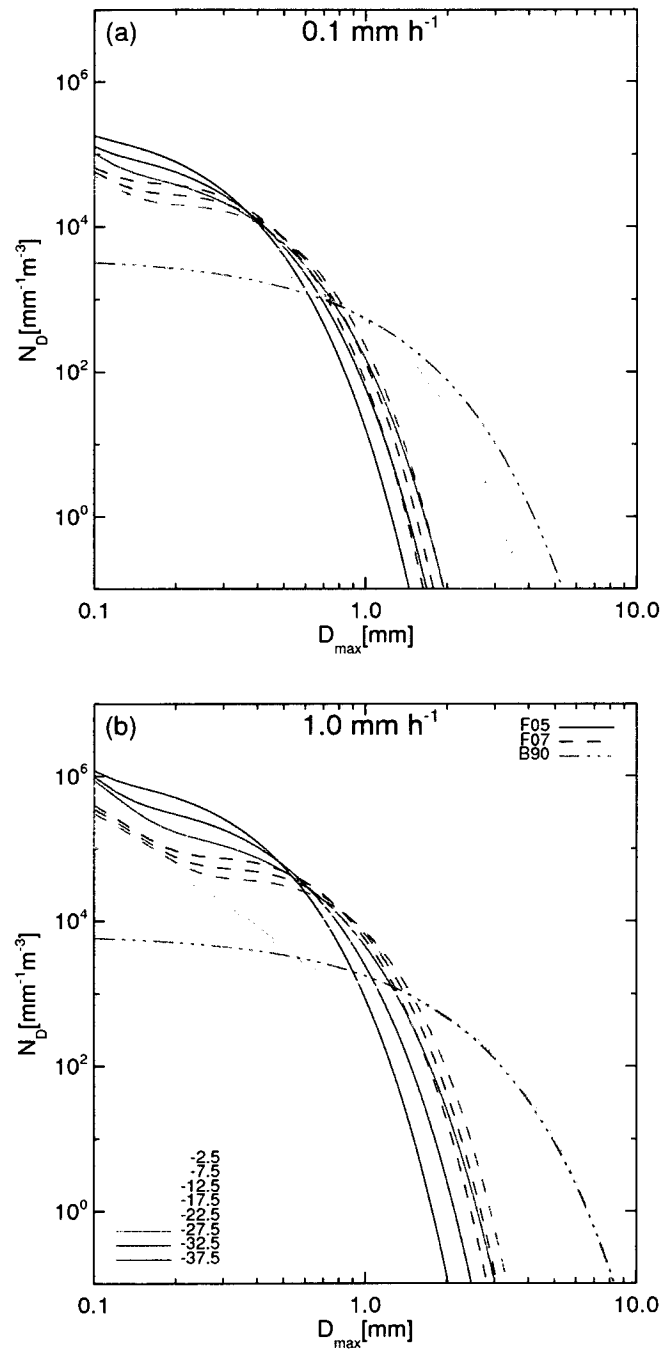


Fig. 4.6: Derived ice particle size distribution using the Field et al. (2005; F05) (solid) and Field et al. (2007; F07) (dash) parameterization at different temperatures (colored lines) for an assumed liquid equivalent snowfall rate of (a) 0.1 and (b) 1.0 mm h⁻¹. The Braham (1990; B90) exponential PSD is also indicated (red dashed line). The average aggregate m - D_{max} and v - D_{max} relationships (Fig. 4.2) are also assumed.

5. Z_e - S/Z_e - IWC relationships

a. Overview

This section describes model-derived equivalent radar reflectivity factor (Z_e) to liquid equivalent snowfall rate (S) or ice water content (IWC) relationships. The Z_e - S/Z_e - IWC relationships are derived using backscatter properties from the ice particle models described in Table 3.1 and Fig. 3.1 through Fig. 3.3, combined with the temperature-dependent F05 PSD parameterization described in Section 4. The Z_e - S/Z_e - IWC relationships are used for the following primary purposes:

- Converting the radar signal (Z_e) to a physically useful geophysical parameter such as S or IWC ;
- Reducing the computational load of explicitly calculating S or IWC . For instance, each CloudSat data swath contains over 37,000 profiles containing over 100 vertical data bins, and the computational burden required to average backscatter properties – and optical properties for radiative transfer simulations – over the derived PSD for each CPR observation is substantial;
- Reconstructing the actual CPR snowfall-related reflectivities to proxy reflectivities at other frequencies of interest (e.g., 13.6 and 35 GHz).

b. Methodology

The Z_e - S/Z_e - IWC relationships are derived via the following two-step process:

1. The ice particle size distribution (PSD) for a specified range of S (0.01 to 2.5 mm h⁻¹) or IWC (0.01 to 2.0 g m⁻³) is derived via the F05 ice PSD moment conversion scheme outlined in Section 4;
2. The dependent variable, Z_e , is calculated for a given S/IWC and ice particle model using the PSD derived in the previous step and backscatter characteristics from various ice habit models. Final Z_e-S/Z_e-IWC relationships are derived using a power law curve fitting routine.

The equivalent radar reflectivity factor, Z_e , can be written (in units of mm⁶ m⁻³) as

$$Z_{e,\lambda} = \frac{\lambda^4}{\pi^5 |K|_{\lambda}^2} \int_{D_0}^{D_1} \sigma(D)_{b,\lambda} N(D) dD, \quad (5.1)$$

where λ is the radar wavelength, $|K|^2$ is related to the dielectric constant of water (assumed to be .93, .88, and .75 at 13.6, 35, and 94 GHz, respectively), σ_b is the frequency-dependent backscatter cross-section for an individual frozen particle shape and size (Fig. 3.7), and D is the maximum particle dimension. The D_0 and D_1 integral constraints are assumed to be 0.1 and 5.5 mm. The lower limit of 0.1 mm is restricted by the F05 PSD parameterization (see Section 4.b), while the upper limit of 5.5 mm corresponds to the H07 – and standardized optical properties (Section 3) – database. Reflectivity values may be artificially depressed by this upper limit when large frozen

hydrometeors associated with elevated S or IWC exceed the D_l threshold for certain ice particle models, so the backscatter properties are extrapolated up to 15 mm to calculate reflectivities under these circumstances (not applicable to certain particle models like spheres and LSS/LDS where optical properties have already been calculated at larger particle sizes).

c. Sensitivity to ice particle model and temperature

Fig. 5.1 and Fig. 5.2 respectively highlight Z_e - S and Z_e - IWC relationships for an assumed temperature of -7.5 C for the 94 GHz frequency and exemplarily illustrate the sensitivity of the derived relationships to the choice of ice particle model. For instance, for an assumed snowfall rate of 1.0 mm h^{-1} , the range of calculated reflectivities exceeds 20 dB due to the combined effects of the backscatter properties and underlying derived PSD's of the various ice habit models. Backscatter properties are also available for many of the ice models at lower frequencies, and Fig. 5.3 illustrates the frequency-dependent nature of the derived Z_e - S relationships as the frequency decreases and the size parameter (i.e., particle size relative to radar wavelength) changes.

The Z_e - S / Z_e - IWC relationships are inherently temperature-dependent and are derived for eleven temperature bins at 5 C intervals between -2.5 C and -57.5 C to account for PSD differences modulated by temperature (F05). Complete temperature-dependent coefficients and exponents for the derived Z_e - S / Z_e - IWC relationships of all ice particle models are presented in Appendix A. Fig. 5.4 also illustrates the effect of

temperature on derived Z_e - S relationships for three different ice models (LR3, LSS, and FS). Each ice habit displays different temperature-dependent sensitivity due to the complex interplay between the backscatter properties and derived PSD at each temperature bin. For example, the possible range of calculated 94 GHz reflectivities for a snowfall rate of 1.0 mm h^{-1} exceeds 9 and 4 dB for the LR3 and FS shapes due to temperature effects, while the LSS habit is rather insensitive to temperature ($< 1 \text{ dB}$). Also note both the LSS and FS shapes produce larger reflectivities at colder temperatures at moderate to heavier snowfall rates, while the LR3 shape progressively produces larger reflectivities at warmer temperatures throughout the entire snowfall rate spectrum – a finding directly linked to the underlying PSD's derived using the models' respective mass and fall speed properties (e.g., Fig. 4.5). Fig. 5.4b indicates amplified temperature dependencies for the three ice particles at 35 GHz exceeding 12, 3, and 10 dB for the LR3, LSS, and FS shapes, respectively. The FS and LSS shapes also reverse the 94 GHz temperature dependency trend, as warmer temperatures generally produce larger reflectivities (especially for the FS shape) due to the differential influence of larger particles in the underlying derived PSD's at 35 versus 94 GHz.

d. Ensemble averaged Z_e - S relationships

Since large uncertainties exist in Z_e - S relationships when prescribing individual ice particle models, an ensemble approach might be advantageous for retrieving average global snowfall rates with appropriate uncertainty bounds. Fig. 5.5 shows best-fit 94

GHz Z_e - S relationships for all of the ice particle models indicated in Table 3.1, with accompanying 1- σ upper and lower uncertainty bounds due to the variable backscatter and PSD properties of the ensemble members. The uncertainty bounds are relatively stable throughout the entire snowfall rate spectrum and indicate an estimated uncertainty of ~ 7 dB due to the ice model. The spherical ice models strongly influence the ensemble average Z_e - S results, especially at higher snowfall rates. If the non-spherical ice models from Table 3.1 are exclusively used to derive the ensemble-averaged Z_e - S relationships, and the 1- σ uncertainties contract from ~ 7 dB to ~ 5 dB at the highest snowfall rates, while the uncertainty related to the lowest snowfall rate remains virtually unchanged. Similar 35 and 13.6 GHz ensemble average results are also available (Table 5.1 and Table 5.2). The validity of spherical ice models – especially in the context of combined active and passive microwave remote sensing of precipitation – will be explored further in Section 7. It also should be noted that a stable power-law relationship for the Z_e - S relationships may not be valid at the highest snowfall rates due to the dampening influence of the backscatter properties associated large particles at 94 GHz – especially for the spherical models. This effect, however, was minimized in the current study by truncating the input snowfall rates used to create the Z_e - S relationships to a maximum value of 2.5 mm h^{-1} . Liquid equivalent snowfall rates exceeding this threshold may contain larger relative errors due to curve fitting effects.

e. Sensitivity to PSD

As shown in Fig. 5.6, the PSD parameterization employed also influences the Z_e - S relationships. Three PSD parameterizations are indicated in Fig. 5.6 (F05, F07, and B90), while two ice models (LR6 and LSS) are chosen for illustrative purposes. For these two ice models, Z_e - S differences due to the F05 and F07 PSD's are virtually indistinguishable at lower temperatures and at low snowfall rates, while reflectivity differences of about 1.5-2.0 dB are possible at higher snowfall rates and warmer temperatures. A definite frequency-dependence exists, however, as the LR6 warmer temperature 35 GHz differences between F05 and F07 increases to over 2.5 dB, while the LSS differences are negligible.

Differences between the B90 and F05/F07 parameterizations are also shape-dependent. As previously mentioned, the LSS habit shows very little sensitivity to the various PSD parameterizations. The B90 and F05 results for the LR6 habit are very similar at warmer temperatures and higher snowfall rates for both 94 and 35 GHz frequencies. Reflectivities produced by the B90 PSD, however, exceed the F05/F07 reflectivities by about 2.5 dB at low snowfall rates and over 4 dB at colder temperatures. The 35 GHz B90 results also consistently exceed the F05/F07 results by ~5-7 dB at lower temperatures.

Simulated reflectivity differences between the PSD parameterizations are better illustrated in Fig. 5.7 and Fig. 5.8, which show the cumulative reflectivity for the LR6 and LSS shapes at two different snowfall rates and frequencies. These figures not only support the findings of Fig. 5.6, but also emphasize the importance of what particle sizes

largely determine calculated reflectivities using the different PSD's and illustrate *how* the Z_e - S differences in Fig. 5.6 arise. Major findings of Fig. 5.7 and Fig. 5.8 include:

1. The increased and important role of sub-1 mm particles contributing to the total reflectivity for the F05/F07 results compared to the B90 exponential PSD;
2. Low overall sensitivity of calculated reflectivities for certain snowfall rates and assumed shapes (e.g., Fig. 5.7c and Fig. 5.7d), but contributions from different particle sizes produce similar reflectivities depending on the PSD parameterization used;
3. B90 PSD results are strongly affected by the assumed particle properties. E.g., if the average aggregate mass/fall speed properties (Fig. 4.2) are assumed instead of the LSS mass/fall speed properties, the derived B90 calculated reflectivity is reduced by ~ 4 -7 dB. The LR6 B90 results, however, are insensitive to this choice.

The Z_e - S differences due to PSD parameterizations can be significant, but they are seemingly of secondary importance compared to the backscatter property differences between the ice models. These results indicate the B90 exponential PSD can produce significantly different results than F05/F07, especially at lower temperatures and snowfall rates, but reflectivity differences at higher snowfall rates and temperatures appear minimal. Even though the magnitude of calculated reflectivities is similar at higher

snowfall rates (e.g. LSS shape at 35 GHz in Fig. 5.6 and Fig. 5.8d), retrieving certain quantities like characteristic particle size may still be complicated by the multitude of different PSD's that can produce similar reflectivities using single frequency radar data. But using combined 94-35 GHz frequencies can enhance retrievals by exploiting the different signatures of the PSD and habit combinations, and further investigation of this topic is necessary for future dual-frequency radar applications. The differences at low temperatures between B90 and the F05/F07 parameterizations can most likely be mitigated by using simple adjustment techniques, as many previous studies have adjusted the exponential PSD slope intercept parameter (N_0) based on temperature (e.g., Wilson and Ballard 1999; Ryan 2000; Woods et al. 2008), and such adjustments appear necessary if exponential PSD's are employed at higher atmospheric levels/lower temperatures to produce physically realistic results. If the exponential slope parameter (Λ) is not adjusted as well, though, vastly differing results than the F05/F07 PSD parameterization are still possible at lower snowfall rates and temperatures. Further comparisons of temperature-adjusted exponential PSD's to F05/F07 are warranted to better characterize PSD uncertainties, but such comparisons are beyond the scope of this study. The F05 PSD parameterization will be utilized as the PSD parameterization throughout the remainder of this study with the implicit acknowledgment that the uncertainty due to PSD assumptions has yet to be fully determined.

Table 5.1: Ensemble averaged 35 GHz Z_e -S relationships – and upper and lower 1- σ uncertainty results – for all ice models (spheres) and only the non-spherical models (DDA) in Table 3.1.

	Spheres	DDA
Upper	$202.69S^{1.25}$	$204.74S^{1.23}$
Average	$46.36S^{1.35}$	$67.79S^{1.36}$
Lower	$10.61S^{1.44}$	$22.45S^{1.49}$

Table 5.2: Same as Table 5.1, but for 13.6 GHz.

	Spheres	DDA
Upper	$306.92S^{1.29}$	$252.01S^{1.26}$
Average	$56.31S^{1.35}$	$73.75S^{1.37}$
Lower	$10.34S^{1.39}$	$21.54S^{1.47}$

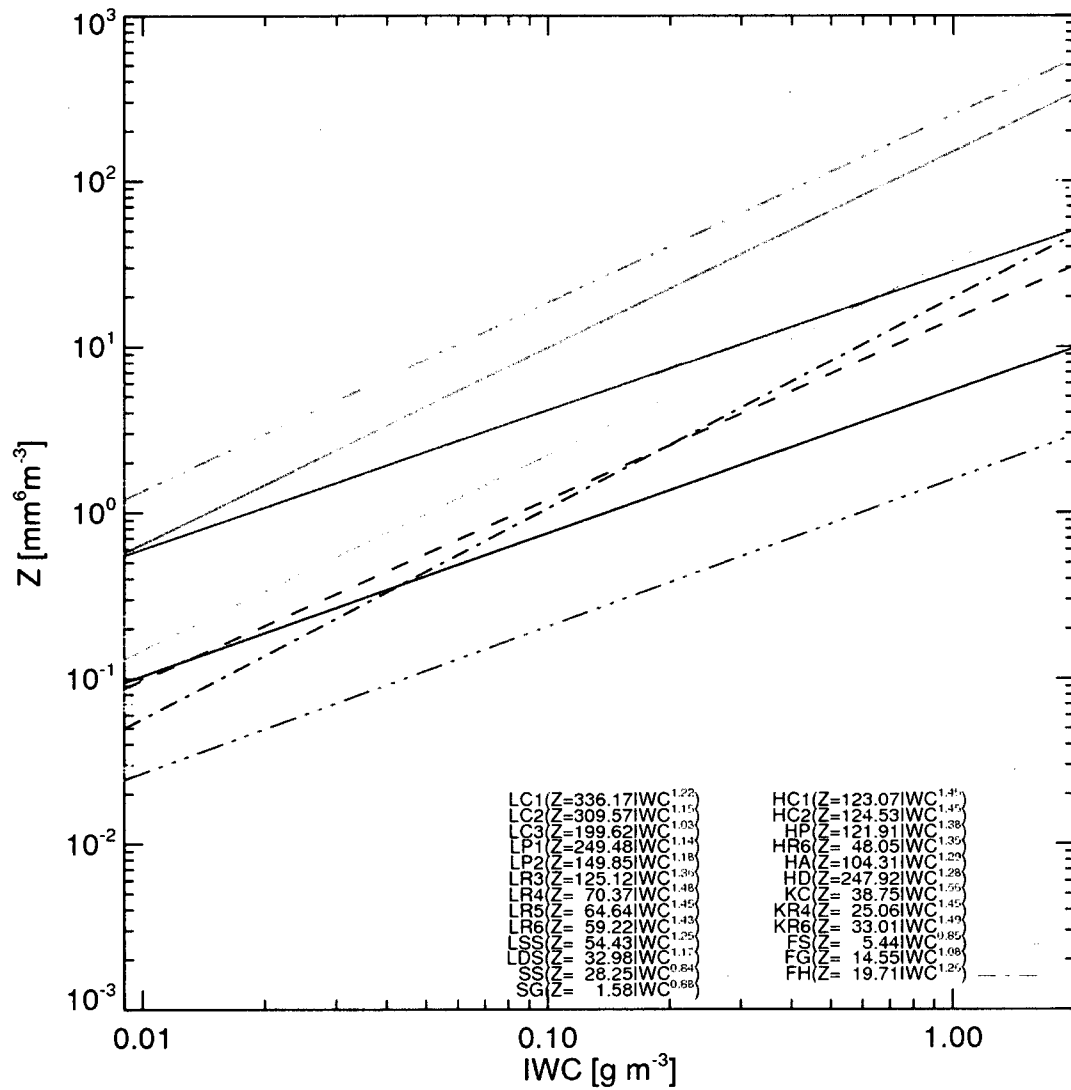


Fig. 5.1: Equivalent radar reflectivity factor (Z_e) – ice water content (IWC) relationships for the ice particle models in Table 3.1 for an assumed temperature of -7.5 C.

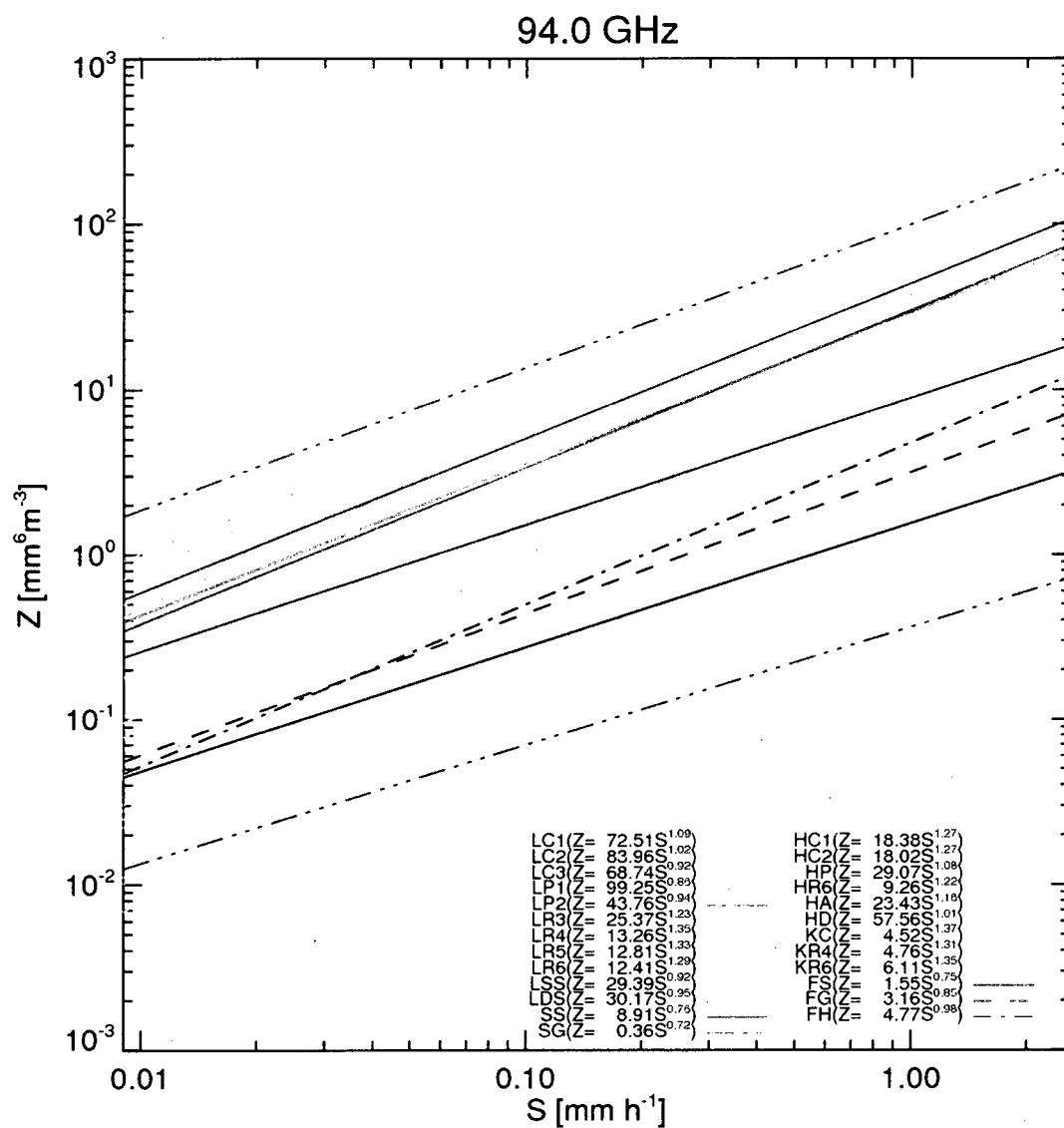


Fig. 5.2: Equivalent radar reflectivity factor (Z_e) – liquid equivalent snowfall rate (S) relationships for the ice particle models in Table 3.1 for an assumed temperature of -7.5 C.

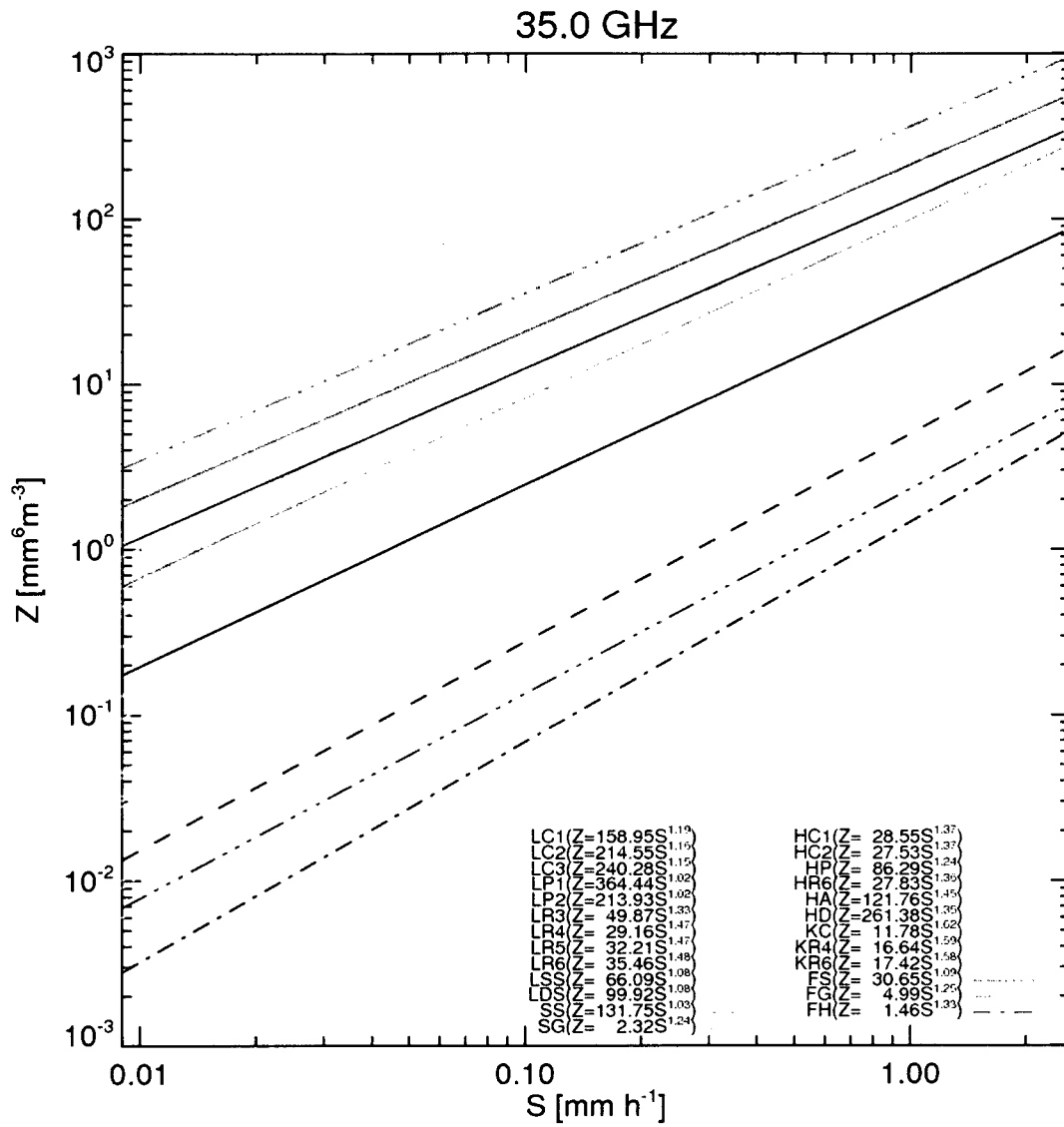


Fig. 5.3: Same as Fig. 5.2, but for 35 GHz.

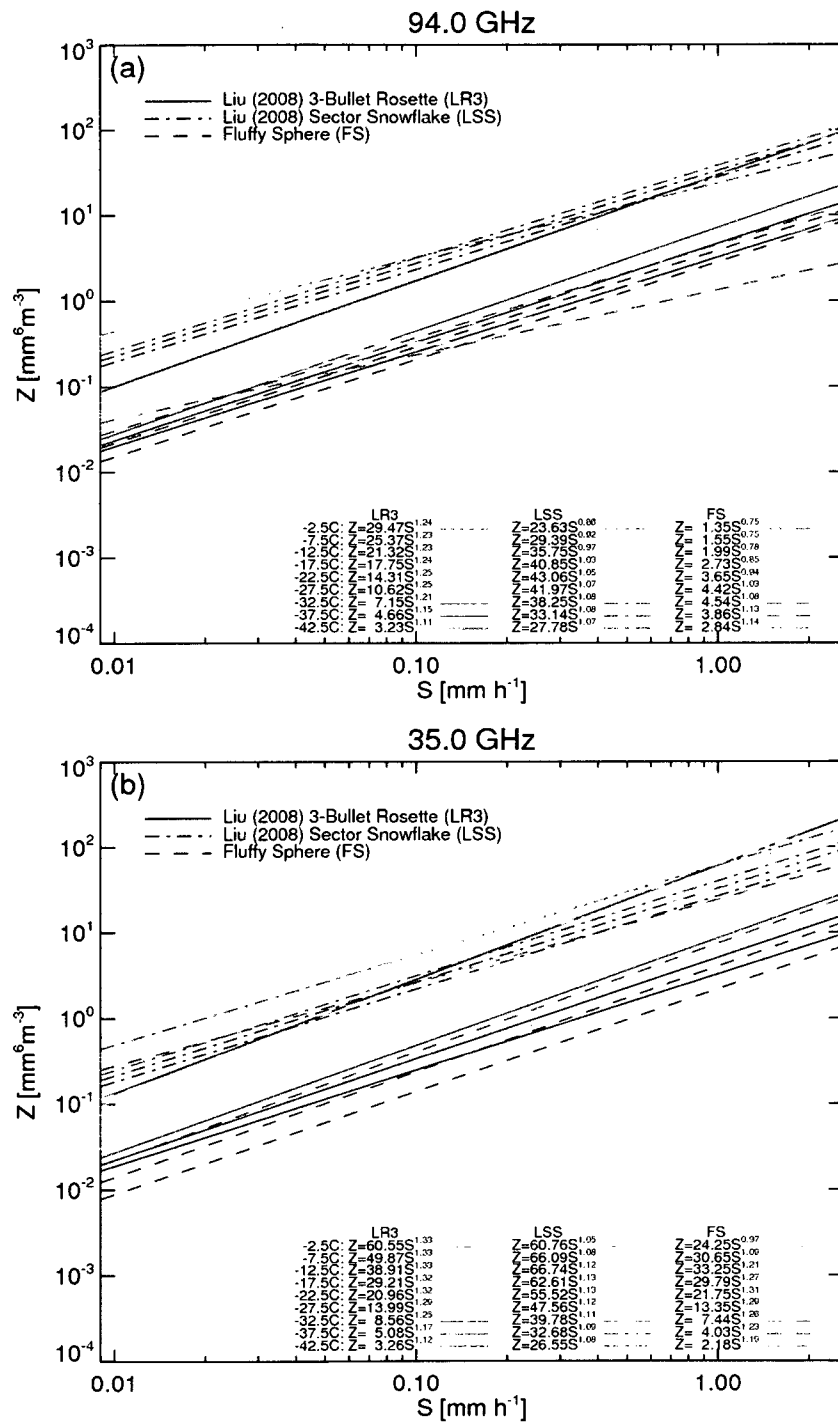


Fig. 5.4: Same as Fig. 5.2 and Fig. 5.3, but showing variation of Z_e - S relationships for the LR3 (solid), LSS (dash-dot), and FS (dash) shapes at various temperatures between -2.5 and -42.5 C (colored lines).

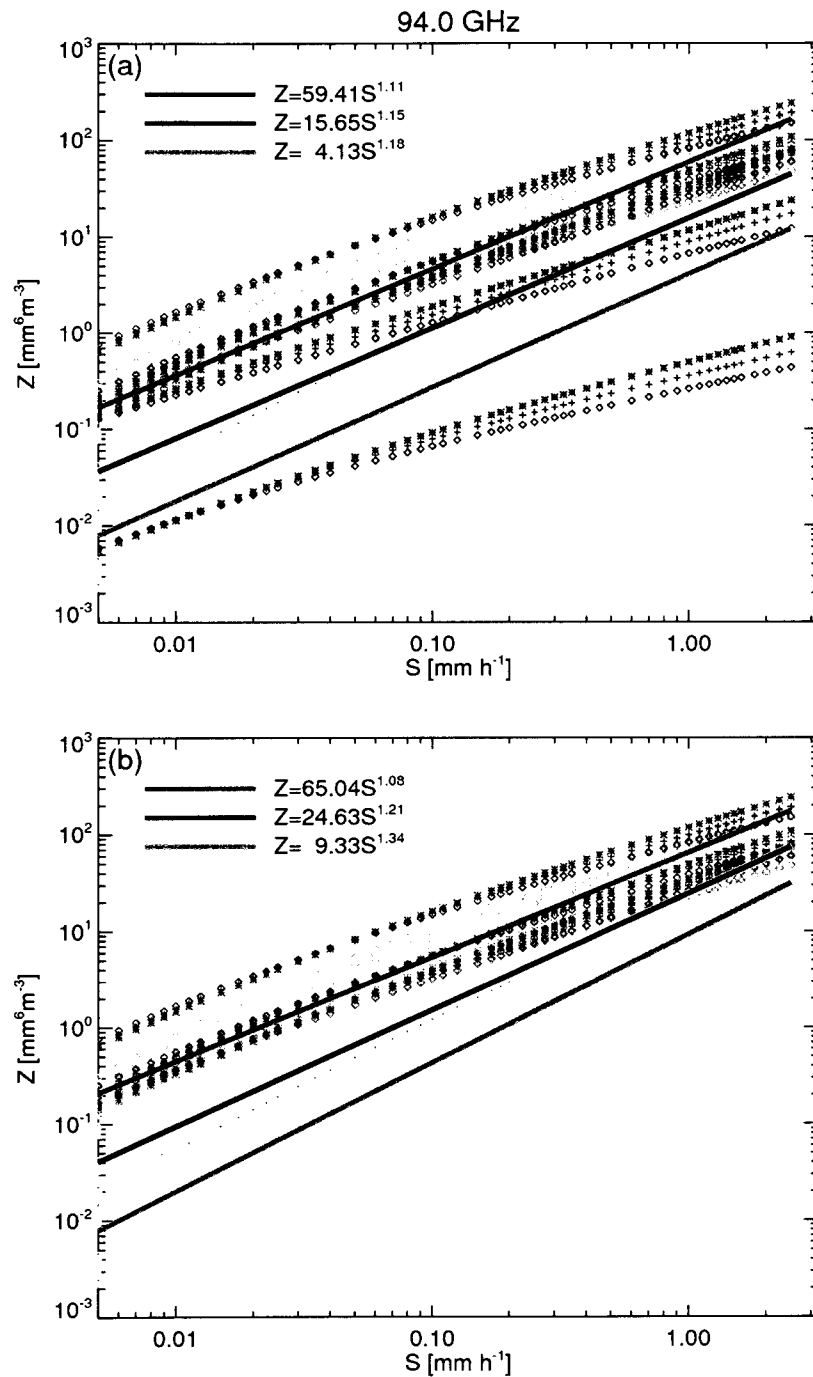


Fig. 5.5: Ensemble-averaged 94 GHz Z_e - S relationships for (a) all ice models and (b) only the non-spherical ice models in Table 3.1. Upper and lower 1- σ uncertainty bounds are also indicated.

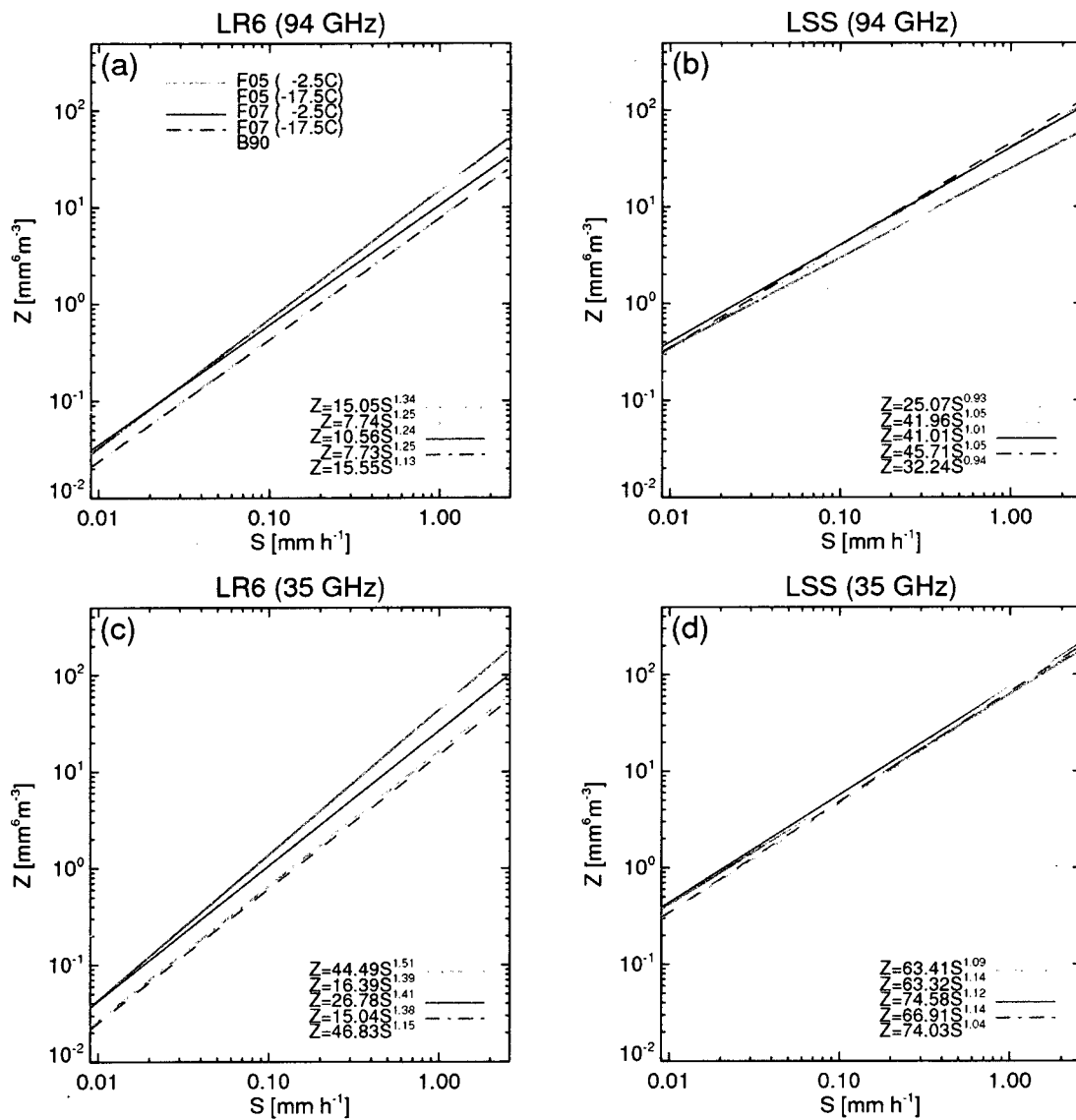


Fig. 5.6: Z_e - S relationships for the LR6 and LSS habits at 94 and 35 GHz using the F05 (dark blue), F07 (light blue), and B90 (green) PSD's. The F05 and F07 results are derived at -2.5 C (solid) and -17.5C (dash).

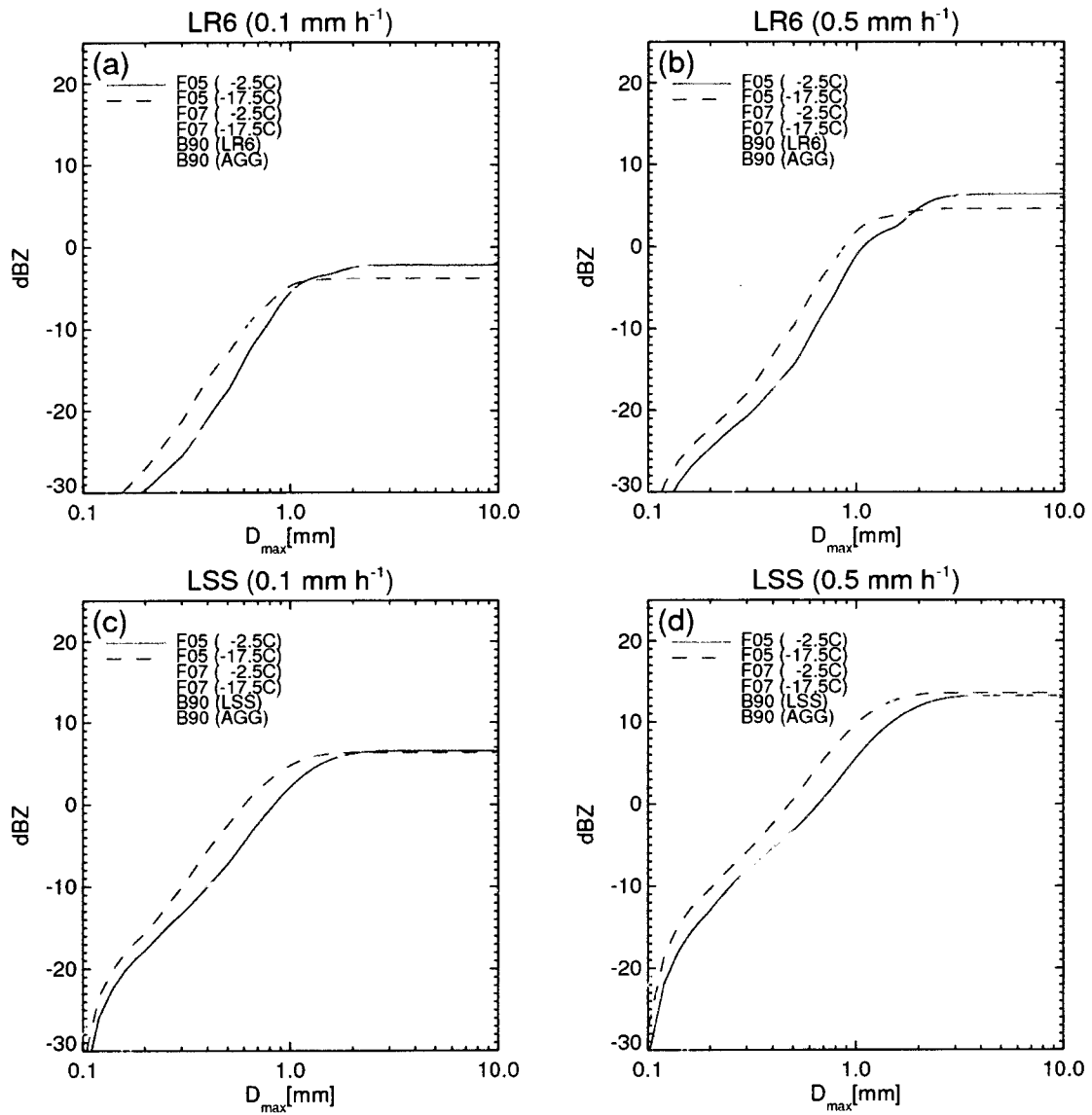


Fig. 5.7: Contribution of different D_{max} values to the total 94 GHz Z_e (in dBZ_e) for the LR6 habit at (a) 0.1 mm h⁻¹ and (b) 0.5 mm h⁻¹. Panels (c) and (d) are the same as panel (a) and (b), except for the LSS shape. The F05 (dark blue), F07 (light blue), and B90 (green) PSD's are also indicated. The F05 and F07 results are derived at -2.5 C (solid) and -17.5 C (dash). B90 results using the average aggregate m - D_{max} and v - D_{max} properties (Fig. 4.2) are also shown (green dash).

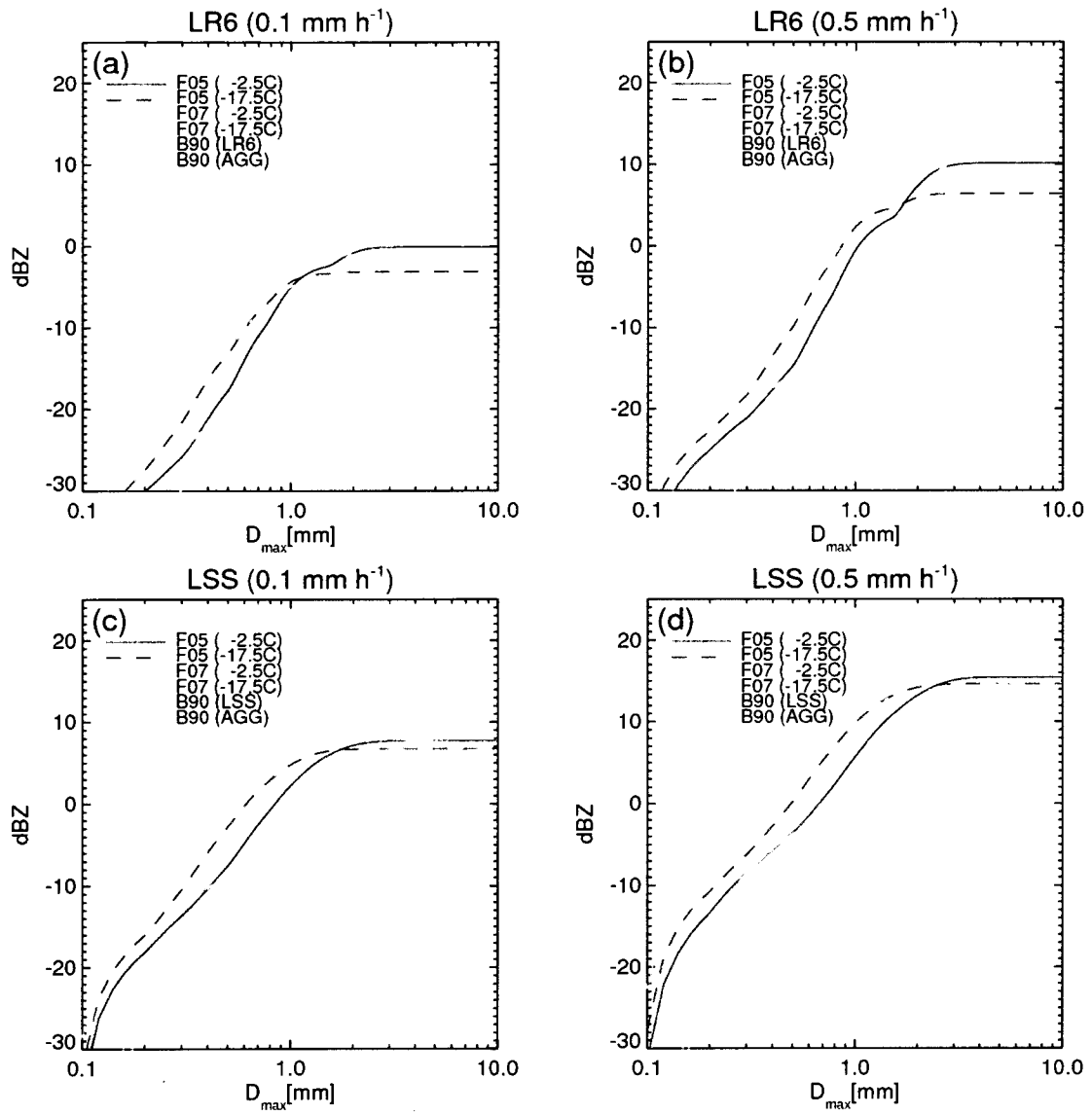


Fig. 5.8: Same as Fig. 5.7, but for 35 GHz.

6. Active/passive assessment of ice particle models

a. Overview

Since the launch of the Scanning Multichannel Microwave Radiometer in the late 1970's, multi-frequency satellite-based passive microwave imagers (e.g., SSM/I, TMI, AMSR-E) have provided retrievals of important geophysical parameters, including ocean and land surface properties, column-integrated atmospheric and cloud properties, and surface precipitation rates. Passive microwave sounders (e.g., MSU, AMSU, MHS) have provided crucial information about the vertical structure of temperature and humidity and have also been exploited for cloud and precipitation applications, while recent spaceborne active microwave instruments (e.g., TRMM, CloudSat) have generated valuable datasets of cloud and precipitation profiles. Cloud and precipitation research has particularly benefited from sustained microwave observations that have enabled the development and continual improvement of global cloud and precipitation climatologies (e.g., Weng et al. 1997; O'Dell et al. 2008; Hilburn and Wentz 2008; Liu and Zipser 2009; Ellis et al. 2009). These climatologies are not only useful to study the global distribution of clouds and precipitation, but also serve as valuable independent validation datasets for global climate and numerical weather prediction (NWP) models.

In addition to numerical model validation, global satellite-based microwave observations (either radiances or derived products) enhance operational NWP applications via data assimilation. This topic has received considerable attention in recent years due to the inherently valuable information content contained in microwave

observations that increases forecast skill (e.g., English et al. 2000; Mahfouf et al. 2005; Weng et al. 2007; Kelly et al. 2008). Clear sky data assimilation is a largely tractable problem from a forward modeling and assimilation standpoint, and clear sky microwave observations have been routinely assimilated operationally in NWP models over the past two decades. Advances in all-weather (i.e., including cloudy and precipitating observations) microwave radiance assimilation have been aided by the recent development of computationally efficient and accurate radiative transfer (RT) models for scattering-intensive conditions commonly associated with clouds and precipitation (e.g., Greenwald et al. 2005; Heidinger et al. 2006; Liu and Weng 2006; Evans 2007). Assimilation of microwave radiances under cloudy and/or precipitating conditions, however, is still rife with many complexities (see Errico et al. 2007 a,b and references therein), and only recently have operational centers assimilated observations containing clouds and precipitation (Bauer et al. 2006 a, b).

Properly characterizing forward modeling errors is essential for effectively incorporating microwave radiances under cloudy and precipitating conditions in operational data assimilation. Numerous possible forward modeling error sources (e.g., the RT solver, cloud microphysical assumptions, surface emissivity parameterizations, three-dimensional RT effects, and others) define the total observation-operator error and its related covariance matrix that influence how the observations are utilized within the data assimilation procedure. To illustrate the complexity and importance of this issue, e.g., O'Dell et al. (2006) reported sample error correlations and covariances due strictly to RT model differences for select microwave imager frequencies. The model errors and

their associated correlations and covariances studied in O'Dell et al. (2006) are undoubtedly less important than some of the other possible forward model error sources previously listed, but they still displayed markedly different behavior depending on the choice of RT model. More work must be undertaken to study the larger sources of observation-operator error and their subsequent impact on data assimilation.

This section focuses on one such potentially large forward model error source related to cloud microphysics – modeling the scattering and extinction properties of frozen hydrometeors – that can produce significant forward model uncertainties in precipitating regions. The scattering signature at higher microwave frequencies due to precipitation-sized frozen hydrometeors was introduced in Section 1, and modeling the scattering signature is a challenging task due to limitations of models used as proxies for naturally-occurring ice habits. Optical properties have been generated for both spherical and non-spherical ice models in an effort to properly characterize realistic scattering effects (see Section 3), and physically assessing these various ice particle models under precipitating conditions is a necessary and critical task for both microwave precipitation retrieval development and data assimilation purposes.

In this section, a modeling system will be described allowing both the active and passive microwave response to clouds and precipitation to be modeled in a framework that requires relevant backscattering (active) and extinction (passive) properties of ice particle models to be physically consistent. This approach uses active microwave data from CloudSat as input to provide vertical profiles of hydrometeors that are subsequently utilized to simulate multi-frequency passive microwave brightness temperatures. The

centerpiece of this combined active/passive modeling system is the microwave optical properties database containing over twenty-five ice particle models and their associated optical properties (Table 3.1) that allows side-by-side objective assessment of these ice models over the entire microwave spectral range and enables realistic forward model uncertainties due to the choice of ice particle model to be established. Simulated brightness temperatures can also be compared with passive microwave observations to study model errors under all-weather conditions. Furthermore, these errors and uncertainties, as well as sample error correlations and covariances, can be partitioned by cloud or precipitation taxonomy to investigate their variability under different meteorological conditions.

b. CPR/AMSR-E/MHS dataset

Data from the AMSR-E and MHS (NOAA-18 satellite only) were collocated with the CloudSat observations for this study (see Section 2 for a description of these instruments and data products). CloudSat and Aqua satellites fly in close formation as part of the ‘A-train’ satellite constellation, so collocated AMSR-E/CPR observations are readily available. Far fewer collocated MHS-CloudSat data points exist, however, since the NOAA-18 satellite does not fly in a coordinated orbit with CloudSat. A combined dataset based on 31 CloudSat overpasses between July, 2006 and January, 2007 was utilized in this study and is described in further detail by Chen et al. (2008). The distance between the instrument footprint centers for the vast majority of the observations in the

collocated dataset does not exceed 5 km, with most matches on the order of a few kilometers. Even though MHS is a cross-track scanning instrument, the collocated MHS data are all near-nadir observations. The dataset was further quality-controlled to include only oceanic observations not affected by sea ice. Further relevant dataset statistics are presented in Section 6e.

c. Methodology

This section describes a combined active/passive modeling system that seamlessly converts CPR observations to simulated multi-frequency passive microwave brightness temperatures.

Pre-processing steps are first performed to correct for attenuation, as well as re-grid and extrapolate the CPR reflectivity data. The W-band radar signal can experience significant attenuation due the combined effects of liquid precipitation, melting precipitation, elevated cloud liquid water contents, large columnar water vapor amounts, and excessive ice water content. Therefore, the columnar 2-way attenuation is calculated for all of these important atmospheric constituents to create an attenuated-corrected reflectivity profile. The CPR reflectivity data can also be affected by surface clutter in the lowest data bins. Since this study is limited to over-ocean observations with a more stable clutter pattern than over-land observations, CPR data bins as low as ~500 m above ground level (AGL) are used. Such data bins can be utilized due to a clutter reduction algorithm applied to data bins 2 through 5 AGL in the version 011 2B-GEOPROF product (Tanelli et al. 2008). The CPR reflectivities are also re-gridded to the standard

ECMWF-AUX product levels and extrapolated to the surface to provide a complete vertical reflectivity profile in 240 m data bins.

After these pre-processing steps, layer microwave optical properties are calculated. Since a main goal of this study is to investigate simulated brightness temperature uncertainties due to different ice habit models, calculating the scattering characteristics of frozen particles is arguably the most important link in the combined active/passive modeling chain. Above the freezing level (temperature information is obtained from the ECMWF-AUX product), frozen hydrometeor profiles are generated directly from the CPR reflectivity fields via temperature- and ice habit-dependent equivalent reflectivity Z_e - IWC conversions (Fig. 5.1). Note the term “ice water content” here refers to the total mass of frozen hydrometeors per unit volume and may be more appropriately labeled “snow water content” in the context of this study.

CloudSat data products are used to generate vertical profiles of other quantities needed to calculate total layer optical properties for RT simulations. Profiles of temperature, pressure, and water vapor content (WVC) are obtained from the ECMWF-AUX product. Cloud liquid water content (LWC) profiles from the 2B-CWC-RO product are directly utilized in non-precipitating regions. A detailed synopsis of the LWC retrieval scheme is available at the CloudSat Data Processing Center (Austin 2007) and is also summarized by Chen et al. (2008). The LWC and WVC profiles are further scaled by their collocated AMSR-E retrieved columnar liquid water path (LWP) and water vapor path (WVP) values. This scaling is performed to obtain improved emission signature simulations at the scale of the passive microwave observations so the scattering

effect of ice particles can be better isolated. In precipitating regions below the freezing level, CPR reflectivity data are converted to rainfall rates using Z_e - R relationships developed for W-band radars (L'Ecuyer and Stephens 2002). AMSR-E LWP retrievals are also used to supplement the CloudSat 2B-CWC-RO LWC retrievals in precipitating conditions. The 2B-CWC-RO LWC retrievals are unusable in precipitating conditions and are flagged accordingly in the product. AMSR-E LWP values are distributed evenly in those data bins containing unphysical (and thus flagged) 2B-CWC-RO LWC solutions to emulate a realistic vertical distribution of cloud liquid water. Layer water vapor and cloud liquid water absorption are respectively derived using the Rosenkranz (1998) and Liebe et al. (1991) algorithms, while liquid precipitation optical properties are generated using standard Mie theory.

Relevant PSD-averaged optical properties (volume extinction, single scattering albedo, and asymmetry factor) are obtained from the combined layer optical properties (e.g., frozen hydrometeors, rain, cloud liquid water, and water vapor) and are used as input for RT simulations. Ocean surface emissivities are modeled using version 2 of the Fast Emissivity Model (FASTEM-2; DeBlonde and English 2001), and all RT calculations are performed with the slant-path version of the Successive Order of Interaction (SOI) RT model (Heidinger et al. 2006; O'Dell et al. 2006) for the following frequencies: 6.9, 10.6, 18.7, 23.8, 36.5, 89.0, and 157.0 GHz. This frequency subset is particularly relevant for the upcoming Global Precipitation Measurement (GPM) mission that will operate a passive microwave imager at similar frequencies, and current passive microwave observations from AMSR-E and MHS are available for these frequencies.

Two sets of simulations for each profile are performed using an assumed 55.1° (AMSR-E) and 0° (MHS) zenith angle. Modeled results are convolved to the approximate passive microwave footprints for comparison purposes.

d. Case study results

i. OVERVIEW

A synoptic-scale precipitation event is presented to highlight the utility of the combined active/passive modeling system and offer an assessment of the ice particle models. This oceanic case study is located between Australia and Antarctica near 0400 UTC on 9 August, 2006 (CloudSat orbit 01497). Fig. 6.1a depicts extensive clouds and precipitation associated with a very large frontal system. Cloud top heights are between 8-10 km, while maximum CPR reflectivities are between 10-15 dBZ_e in the cold sector, and 15-20 dBZ_e in the warmer, raining locations. An interesting feature of this particular CloudSat overpass is the transition from frozen to liquid precipitation coinciding with a freezing level increase from 0 to 2 km near 57.5°S latitude. Enhanced CPR brightband features accompany this transition and confirm the existence of liquid hydrometeors below 2 km AGL. With the exception of some liquid cloud features near 60°S , retrieved LWP values are very low in the snowfall regions (Fig. 6.1f). LWP increases north of the transition zone, with numerous retrieved LWP maxima exceeding 0.2 kg m^{-2} coinciding with near-surface reflectivity maxima.

Fig. 6.1b through Fig. 6.1e illustrate AMSR-E observations for the vertically polarized (V) 36 and 89 GHz channels, as well as MHS observations at 89 and 157 GHz. These observations indicate warmer brightness temperatures (T_B) at all frequencies coincident with emission from LWP, and lower T_B values between ~ 59 - 57° S in snowing regions due to reduced LWP and enhanced scattering from frozen hydrometeors.

ii. VALIDITY OF ICE PARTICLE MODELS

Simulation results using the ice particle models from Table 3.1 are also overlaid in Fig. 6.1 revealing the sensitivity of the forward model calculations to the choice of ice particle model. The most obvious feature in the simulation results is the large deviation from observations associated with certain ice particle models. For instance, the Hong (2007) and Liu (2004) (hereinafter referred to as the “DDA” ensemble) 36V simulation results realistically follow the AMSR-E observations (Fig. 6.1b). Since the 36V channel is most sensitive to LWP emission and not as susceptible to scattering as higher frequency channels, large sensitivity to the various ice particle models is not expected. However, most spherical and Kim et al. (2007) models grossly deviate from the observations in the snowfall regions when the columnar ice water path (IWP) reaches a critical level. Similarly, the emission signals revert to T_B depressions in high-LWP regions (Fig. 6.1f) for these same ice models. This trend is magnified at higher frequencies (Fig. 6.1c-e), and large simulated T_B depressions exist in the precipitating regions. Conversely, the simulated T_B 's from the Hong (2007) and Liu (2004) models produce physically realistic results for all frequencies. Similar discrepancies between

the ice particle models are pervasive throughout the entire dataset for precipitation events.

The cause of the simulated T_B discrepancies is due primarily to the following effects related to optical property differences between the ice habit models: (1) Z_e -IWC relationships and (2) extinction properties. The first link in the modeling system uses backscatter properties for each ice model to convert CPR reflectivities to IWC using Z_e -IWC relationships. Fig. 6.2 compares the derived IWP from three spherical models – as well as the KR6 habit and DDA ensemble average – for the precipitation event shown in Fig. 6.1. The FS-derived IWP consistently exceeds the DDA-derived IWP by about an order of magnitude in higher IWP regions due to the Z_e -IWC relationships shown in Fig. 5.1. For a given CPR reflectivity, the FS-derived IWC is much larger than the DDA-derived IWC due to comparatively smaller backscatter cross-sections of the low-density spherical model at all particle sizes (Fig. 3.7) which strongly affect the Z_e -IWC relationships. The inflated layer IWC retrievals cumulatively produce excessive column-integrated IWP and are a primary reason for the large simulated T_B depressions due to intensive scattering by the low-density spherical models.

The higher density spherical models (FG, FH) and the KR6 habit also exceed the DDA ensemble average IWP – and the upper IWP limit defined by the DDA ensemble uncertainty – by a smaller, yet still significant, margin compared to the FS habit. (The large derived IWP uncertainty exceeding 50-75% of the DDA ensemble is also worth mentioning and will be highlighted in Section 6f). However, these particles also exhibit larger PSD-averaged extinction properties for a given IWC compared to the DDA

ensemble average (Fig. 6.3). The combination of elevated retrieved IWP and increased extinction are therefore both significant factors contributing to reduced simulated T_B 's for the FG, FH, and KR6 models. Most of these ice models reside within the uncertainty range of the DDA ensemble at lower IWC amounts and only exceed the DDA ensemble uncertainty envelope at larger IWC's, so the PSD-averaged extinction properties do not differ as dramatically from the DDA ensemble as the FS backscatter properties. Note also the extinction properties of the FS model, which are located within the DDA ensemble uncertainty range, but gradually exhibit increased extinction at higher IWC levels and augment the large retrieved IWP's to produce excessive scattering.

iii. SIMULATION UNCERTAINTIES AND ERRORS

Since the relative validity of the DDA ensemble has been established, only DDA ensemble results are shown in Fig. 6.4 to highlight simulation uncertainties at each frequency. Simulated T_{B36V} uncertainties are very low (<0.75 K) for this emission-sensitive channel. There is very little overall bias in the simulated T_{B36V} results compared to ASMR-E observations in the snowfall sector due to low LWP values in this region (Fig. 6.1f). Note, however, the excellent agreement between simulation results and observations near the LWP maximum located at $\sim 59.7^\circ\text{S}$ associated with a shallow liquid cloud feature – an unsurprising result since the model LWP is directly scaled to AMSR-E derived LWP. In the raining regions, however, there are several areas of negative T_{B36V} bias where the model underestimates emission.

Larger simulated T_{B89V} uncertainties display a functional relationship with IWP and range from 4 to 9 K in the snowing regions (Fig. 6.4), thus indicating stronger sensitivity of this channel to the scattering properties of the different ice models in higher-IWP regions. Simulated T_{B89V} uncertainties in the warm sector of the synoptic weather system are generally between 2-3 K. The simulated T_{B89V} results are consistently biased low (up to ~ 14 K, but with large uncertainties) when compared to AMSR-E observations – but are not egregiously low like the spherical model results (Fig. 6.1). As shown in Fig. 6.5a, simulated 89 GHz scattering index (S_{89} ; Petty 1994) indicate excessive scattering in the snowfall region. Vertical (V) and horizontal (H) polarization information from the 89 GHz channels – combined with estimates of $T_{B89V/H}$ in nearby cloud-free regions – are used to calculate S_{89} to estimate the T_B depression due to scattering by frozen particles. Simulated S_{89} values exceed those derived by AMSR-E observations by a factor of 2 over much of the snowfall region. The simulated S_{89} values are not inflated in the liquid precipitation regions (Fig. 6.5a), while simulated T_{B89V} values in these same regions are consistently lower than observed values (Fig. 6.1c), thus hinting at emission underestimation similar to the 36V results.

The satellite zenith angle also needs to be considered when characterizing simulated T_B uncertainties. In contrast to 89V results with an oblique satellite viewing angle, the MHS 89 GHz near-nadir observations and simulated results display a much lower sensitivity to frozen hydrometeors and only respond to emission from LWP (Fig. 6.1d). Simulated T_{B89} uncertainties are generally between 1-2 K for the highest IWP locations in the snowfall region and are negligible elsewhere (Fig. 6.4). This lack of

sensitivity to IWP is also emphasized by no discernible T_{B89} depression when compared to cloud-free RT simulations (Fig. 6.5b).

The 157 GHz MHS observations and simulated T_B 's display increased sensitivity to IWP at near-nadir viewing angles than the 89 GHz channel. There are noticeable T_{B157} minima coinciding with high IWP values (Fig. 6.1e), simulated T_{B157} uncertainties are between 2-5 K in these same regions (Fig. 6.4), and T_{B157} depressions compared to cloud-free simulations are readily apparent (Fig. 6.5b). Additionally, differences in T_{B157} and T_{B89} emphasize the enhanced sensitivity of the 157 GHz channel to IWP (Fig. 6.5c). Unlike the 89V results, comparisons between MHS and simulated T_{B157} are excellent and exhibit relatively low bias in the highest scattering regions (Fig. 6.1e). Also note the higher simulated 89V versus 157 GHz uncertainties due to viewing angle effects (Fig. 6.4).

iv. INDIVIDUAL ICE PARTICLE MODEL COMPARISONS

Some of the Hong (2007) and Liu (2004) ice habits (e.g. columns, plates, droxtals, simple rosettes, etc.) are probably not intended as realistic proxies for precipitation-sized ice particles, but rather for smaller ice habits commonly observed in higher-level ice clouds. To justify using an ensemble average containing all of these habits to calculate model uncertainties in precipitating regions, Fig. 6.6 shows simulated versus observed T_{B157} biases for the case study. A few ice habits demonstrate very low biases (< 0.3 K) across the entire precipitating system between $\sim 60^\circ$ and 51° S (i.e., the "All" column in

Fig. 6.6), specifically the LC1, LSS, LR3, LC2, and HA models. Note, however, the extreme variability in simulated biases when regional subsets (labeled “I” through “V” in Fig. 6.1a) are considered. These may indicate fundamental changes in scattering properties of the frozen particles in different sections of the synoptic weather system. For instance, the HR6 model has one of the higher bias values (~ 1.9 K) over the entire domain, but displays the lowest biases in Region III and V. The LP2 shape exhibits typical biases near 2 K in all other areas except Region IV, where its bias is very low. The variability of these results seems to justify using an ensemble populated by the entire Hong (2007) and Liu (2008) dataset, as the combined active/passive optical properties of even the pristine crystal habits compare well in the precipitating regions. However, other error sources not related to the scattering properties of the ice models could also affect the results in Fig. 6.6. The 157 GHz channel, however, should be substantially less sensitive to error sources from lower atmospheric levels in the presence of adequate IWP (e.g., Bennartz and Bauer 2003). This trait is highlighted in Fig. 6.5b, which shows the enhanced sensitivity of the nadir 89 GHz channel to emission in the high-LWP regions. Conversely, the 157 GHz results do not display such large peaks in the same regions because of enhanced scattering by ice particles aloft, and the biases reflected in Fig. 6.6 are presumably more immune from error sources other than the ice particle model.

v. SUMMARY OF CASE STUDY RESULTS

In summary, the case study highlights the following issues:

- Spherical and Kim et al. (2007) models produce unrealistic simulated T_B results due to combined backscatter and extinction properties, while other non-spherical models are more physically consistent;
- IWP retrieval uncertainty exceeding 50% for the DDA ensemble;
- High (low) sensitivity of the 89V/157 nadir (36V/89 nadir) channels to IWP, and largest simulated IWP-dependent T_B uncertainties associated with 89V (up to 9 K) and 157 (up to 5 K).
- Excellent agreement between simulations and observations for 36V, 89, and 157 GHz in the snowfall region, but excessive simulated T_{B89V} depressions;
- Negative simulated T_B biases at all frequencies in the rainfall region;
- Highly variable simulation-MHS T_{B157} comparisons for the different ice particle models in sub-regions of the synoptic weather system.

e. Global results

i. STATISTICAL COMPARISON BY PRECIPITATION TYPE

In this section, results from the entire collocated CloudSat/AMSR-E/MHS dataset are tabulated by different criteria to demonstrate differences based on cloud or precipitation type. Table 6.1 shows the cloud and precipitation categories, as well as the number of collocated CloudSat/AMSR-E/MHS observations associated with each category used to calculate the statistics displayed in Fig. 6.7. Precipitation classification was performed manually/visually based on the CloudSat swaths and auxiliary

temperature information. Since this study focuses on precipitation, and since Chen et al. (2008) provides a detailed examination of RT validation based on many additional cloud categories from the CloudSat products, only three non-precipitating cloud categories are indicated in Table 6.1. Note that the “cold” cloud category is defined broadly, and in addition to ice clouds, may also include clouds comprised of supercooled water.

Statistics for the various cloud and precipitation types are shown in Fig. 6.7. These statistical measures (bias, bias-corrected root-mean square error (RMSE), correlation coefficient, and average T_B uncertainty) are defined with respect to simulations versus observations. The average T_B uncertainty ($\bar{\sigma}$) is the standard deviation between the T_B results for the different ice models and is thus a measure for the spread between the different simulations. As illustrated in the case study, there are notable differences between the spherical and DDA ensembles. The spheres consistently produce large biases and RMSE values, low correlations, and very large $\bar{\sigma}$ values for the entire collocated dataset (not shown). The remaining analysis and discussion will therefore focus exclusively on the DDA ensemble results shown in Fig. 6.7.

For clear-sky cases, all frequencies exhibit low biases, high correlations, and low RMSE values, indicating clear-sky atmospheric and ocean surface properties are modeled realistically. The cloud categories contain relatively small negative biases and similar statistical results, with the larger negative 89V biases for cold clouds the only notable difference between the cloud types. The global DDA results, however, display trends dependent on frequency and precipitation type. Highlights of the global DDA ensemble results from Fig. 6.7 include:

- Distinct statistical differences between precipitation categories (e.g., note the “all precipitation” versus various stratiform categories).
- Stratiform brightband events display the largest negative biases, although the 36V low freezing level stratiform bias is reduced for this category, presumably due to lower LWP/less emission associated with these events.
- Negative biases of 3-4 K for many precipitation categories.
- High correlations exceeding 0.9 for most precipitation categories.
- Distinct viewing angle differences between 89V and 89 nadir results.
- Lower 157 GHz biases (-1 to -1.5 K) for most precipitation categories. E.g., bias differences for the brightband and other stratiform categories are not as distinct compared to lower frequencies, most likely due to scattering by frozen particles aloft to modulate brightband emission.

ii. DEPENDENCE ON ICE CONTENT

The average simulated T_B uncertainties ($\bar{\sigma}$) due to ice particle model shown in Fig. 6.7d mimic the test case results due to their frequency dependence, but also point to distinctive differences between precipitation categories. Simulated σ_{36V} are very low due to decreased sensitivity of this channel to scattering effects, while σ_{89V} has higher values exceeding 1K for most categories and 2.5K for the brightband cases. The σ_{89} nadir values are consistently below ~ 0.6 K, except for the brightband category (~ 0.9 K). The σ_{157} nadir values display substantial variability between the precipitation categories, with

the brightband events possessing the highest average simulated T_B uncertainty (1.8 K). The average T_B uncertainties presented in Fig. 6.7 are useful to illustrate the sensitivity of simulated results to the ice particle model, but they should be analyzed with caution since these uncertainties exhibit a functional dependence to retrieved IWP (Fig. 6.4).

Since IWP retrievals are dependent on the ice model, an integrated reflectivity quantity (Z_{int} ; units of $\text{mm}^6 \text{m}^{-2}$) is introduced as a proxy for IWP:

$$Z_{\text{int}} = \int_{H_{\text{FL}}}^{H_{\text{CT}}} Z_{\text{CPR}}(z) dz, \quad (3)$$

where Z_{CPR} is the observed CPR reflectivity at a given height z and $H_{\text{FL}}/H_{\text{CT}}$ are the respective freezing level/cloud top heights. Z_{int} is a useful metric since it conveys an integrated columnar property above the freezing level, yet is independent of the ice habit model. Histograms of Z_{int} based on precipitation taxonomy are shown in Fig. 6.8. Note the wide disparity in Z_{int} distributions between the various precipitation types. Fig. 6.9 displays IWP as a function of Z_{int} for all mid-latitude stratiform precipitation cases using the DDA ensemble to illustrate the physical relationship between IWP and Z_{int} . The Z_{int} maxima near 40 dBZ_{int} for mid-latitude stratiform precipitation corresponds to a retrieved IWP of $\sim 0.3 \text{ kg m}^{-2}$, while 50 dBZ_{int} equates to $\sim 1.0 \text{ kg m}^{-2}$ of IWP, albeit with significant uncertainties due to the Z_e -IWC relationships.

Fig. 6.10 shows σ_{157} as a function of Z_{int} based on best-fit lines between these two quantities (not shown) to investigate simulated T_B uncertainty differences among the precipitation categories due to average columnar ice properties. As Fig. 7.10a indicates, the differences in σ_{157} are not expansive between the stratiform categories at lower Z_{int}

levels, but larger variations occur at higher Z_{int} data bins. The bias-corrected RMSE values for 157 GHz are also shown in Fig. 7.10b. When used in combination with the results from Fig. 7.10a, the T_{B} uncertainties due to scattering characteristics of the ice models contribute significantly to the overall model error variability at the highest Z_{int} levels, while other model error sources appear to dominate the error variability at lower Z_{int} levels – especially for the “all precipitation” category.

Fig. 6.11 illustrates 157 GHz simulation biases for the individual ice particle models in the DDA ensemble as a function of Z_{int} for all mid-latitude stratiform precipitation observations. The bias magnitudes are consistently low ($< \sim 1$ K) below the 35 dB Z_{int} data bin. There is also minimal spread in the bias results among the various ice particle models below this threshold, so the ice particle model employed is not particularly crucial until a critical Z_{int} level is reached. There is considerable divergence in the bias results above the 35 dB Z_{int} threshold, and numerous individual ice particle models in the DDA ensemble exhibit large negative biases due to excessive scattering when dB Z_{int} exceeds about 45. In contrast to the case study results, there are a few select ice particle models that produce more consistent results across the entire Z_{int} spectrum (e.g., HP, HR6, LDS), while others become outliers at the highest Z_{int} levels. The number of observations reduces sharply in the mid-latitude stratiform category above ~ 45 dB Z_{int} , so the statistics above this threshold are not as robust. Nonetheless, these results indicate potential systematic errors in the optical properties for many of the DDA ensemble members at high Z_{int} levels, so the veracity of the DDA ensemble for microwave remote sensing of high-IWP precipitation events remains questionable.

iii. ERROR COVARIANCE/CORRELATIONS

Error correlations and covariances for two mid-latitude stratiform precipitation categories (40 dBZ_{int} data bin only) are shown in Table 6.2 and Table 6.3 to illustrate the utility of the combined active/passive modeling results to data assimilation applications. The off-diagonal elements of such error covariance matrices can significantly influence how the observations are utilized in data assimilation schemes, yet are difficult to characterize under precipitating conditions. Table 6.2 and Table 6.3 combine the error correlations (upper right half of the matrix) and covariances (lower left half of the matrix, including the diagonal elements). The complete observational error matrix would contain all microwave channels, but only the vertically polarized channels are indicated in Table 6.2 and Table 6.3 for brevity. Lower frequency channels are also not illustrated due to their low sensitivity to ice particle model. Since 157 GHz observations containing polarization diversity at an AMSR-E-like viewing angle are not available, the nadir results are assumed to realistically represent the error correlations/covariances. Model biases are also first removed before the error correlations and covariances are calculated.

The error correlations and covariances shown in Table 6.2 and Table 6.3 again highlight the importance of partitioning results between different precipitation types. Error correlations exceed 0.75 between all of the lowest three channels (18, 23, and 36 GHz) in both precipitation categories, with the higher freezing level category displaying slightly increased correlations at these frequencies. Note, however, the covariance

differences for these same channels between the two precipitation categories. For instance, the 36V covariance value increases from 1.84 (low freezing level) to over 11 K² (higher freezing level) due to increased error variance at this channel. Error correlations between the 89/157 GHz channels and the lower three frequencies are consistently lower, although the 36V-89V error correlation increases from 0.13 (low freezing level) to 0.31 (high freezing level). The error correlations between 89V and 157 are much higher than the 89V/157 error correlations with lower frequencies. The higher freezing level category also has a noticeably higher 89V-157 error correlation than lower freezing level events, while a large 89V covariance disparity exists between the two precipitation categories. Fig. 6.12 also highlights 89V-157 and 89V-36V error correlation differences – and 157 GHz variance calculations – as a function of Z_{int} for three different precipitation categories. The mid-latitude stratiform categories display mostly similar 157-89V error correlation trends and magnitudes, but there are larger discrepancies evident at certain Z_{int} data bins. The shallow convective precipitation 157-89V error correlations, however, diverge strongly from the stratiform categories below the 40 dBZ_{int} data bin. Considerable variability also exists between the three precipitation types in the 89V-36V error correlations. Similar to Fig. 7.10b, the 157 GHz variances exhibit a Z_{int} dependency and are dictated by scattering effects at the highest Z_{int} levels (Fig. 6.12c). Note that the variances in Fig. 6.12 link the error correlations with covariances shown in Table 6.2 and Table 6.3.

f. Summary

This study describes a combined active/passive microwave modeling system that directly converts observed CloudSat CPR reflectivity fields to multi-frequency passive microwave brightness temperatures. The realistic vertical profiles of hydrometeors provided by the CPR data are particularly beneficial, and CPR observations also allow the variability of the modeling results to be studied by precipitation taxonomy. This modeling system also places inherent restrictions on the optical properties of frozen hydrometeor models, requiring both backscattering (converting reflectivity to IWC to derive the PSD) and extinction (calculating PSD-averaged optical properties for passive microwave RT simulations) properties to be self-consistent to produce realistic results from both an active and passive microwave perspective.

Since brightness temperature depressions due to scattering by frozen hydrometeors are the primary higher frequency passive microwave precipitation signature and a large source of forward model uncertainty, a primary purpose of this study is to illustrate the sensitivity of simulated results to the choice of ice particle model. Synoptic precipitation case study results, as well as globally-averaged results, indicate certain ice particle models (e.g., low-density spheres) produce consistently implausible results compared to coincident AMSR-E and MHS observations due to excessive scattering. These unphysical brightness temperature depressions are caused by inflated layer-derived IWC due to a priori Z_e -IWC relationships established for the ice particle models (especially for low-density soft spheres), as well as increased PSD-averaged extinction for other ice models. Recent work by Petty and Huang (2010) also highlights

discrepancies between extinction and backscatter properties of spherical and complex aggregate ice models, so the results in this study confirm the inherent difficulty using spheres for combined active and passive microwave remote sensing applications. Other non-spherical ice models from the Hong (2007) and Liu (2004) possess more physically realistic combined microwave backscattering and extinction properties, and these models produce consistently better results compared to multi-frequency passive microwave observations of precipitation, although derived IWP uncertainties from these models exceed 50-75% in precipitating regions.

An ensemble approach is adopted to highlight forward model uncertainties and errors due to the choice of ice particle model on a global scale, but only ice habits from the Hong (2007) and Liu (2008) datasets are included in the ensemble. The global results are partitioned into different cloud and precipitation categories, with ensuing variability evident between different precipitation categories. Overall, consistent negative model biases in the -1 to -4 K range exist for most precipitation categories, but there is considerable variability in these results due to frequency, zenith angle, and precipitation type. The simulated brightness temperature uncertainty due to ice particle model is also shown to be as high as 9 K for the vertically polarized 89 GHz channel under heavier snowfall conditions, but this uncertainty is reduced to about 2K in liquid precipitation regions and appears to be a strong function of ice water path. Two other high frequency nadir-viewing channels display lower uncertainties of about 4 (2) K for nadir 157 (89) GHz simulated results under high-ice water path conditions. The 157 GHz simulated brightness temperature uncertainties are also stratified by integrated CPR reflectivity

above the freezing level (as a proxy for ice water path), and precipitation-type dependencies are noted. Increased 157 GHz biases also exist for many members of the DDA ensemble for high ice water path events, and the realism of these ice models may be questionable under such circumstances and must be tested further.

These results also indicate a one-size-fits-all precipitation categorization might not be the most optimal way to characterize forward model uncertainties and errors. It might be preferable to instead partition results into further sub-categories based on a combination of latitude, precipitation type, and an integrated quantity indicative of columnar ice content (e.g., integrated reflectivity above the freezing level). For instance, the stratiform category of precipitation – which is often used as a generic precipitation type to partition research results – displays distinctive trends between the various stratiform sub-categories reported in this study. Significant variability in model error correlations and covariances between select microwave frequencies are shown in this study due to precipitation type and columnar ice amount, and the promise of improved all-weather data assimilation of microwave observations will ultimately rely on better characterizing such error correlation/covariance behavior under different precipitating conditions. Since the criteria for partitioning observations into precipitation categories were subjectively chosen in this study, future efforts should be focused on developing improved objectively-based precipitation categorization. Furthermore, developing a larger combined active/passive microwave observational dataset would be beneficial to increase the sampling of all precipitation sub-categories presented in this work. For instance, a precipitation category such as “snowfall-only” could be developed with more

observations and would be beneficial to isolate errors due to scattering by frozen hydrometeors and decouple them from emission-based errors from liquid or melting precipitation.

Future work will also be devoted to improve model components that may be the source of errors highlighted throughout this study. For instance, negative simulated 36 and 89 GHz biases observed under raining conditions are not directly related to scattering by frozen hydrometeors, but rather due to a possible combination of the following effects: (1) underestimation of columnar total water path; (2) liquid and ice partitioning near the freezing level (especially if there are model-derived temperature errors); and (3) no explicit modeling of brightband emission effects. The brightband can significantly increase T_B emissions due to dielectric property changes in melting particles (e.g. Bauer et al. 1999), and the current methodology may accordingly suffer from no explicit treatment of the brightband's enhanced emissive qualities. The 157 GHz channel, however, displays reduced biases compared to the lower frequencies under raining conditions, so this frequency seems more immune to emission-based bias sources because of its enhanced sensitivity to scattering by frozen particles aloft. Additionally, excessive scattering in snowing regions is evident in the 89 GHz oblique viewing angle simulations, but not in the nadir 89 and 157 GHz results, so further work must be conducted to isolate this error source. In light of recent work reported by Matrosov and Battaglia (2009), multiple scattering versus attenuation effects in W-band radar snowfall observations must be studied more thoroughly, as the attenuation correction scheme employed in this study

might be too aggressive and may contribute to overestimating retrieved layer IWC that, in turn, can contribute to excessive simulated scattering signatures.

Finally, the large derived IWP uncertainties due to ice model, combined with the simulated passive microwave results, indicate potential IWP retrieval implications. Even if the spherical models are disregarded, IWP uncertainties from the Z_e -IWC relationships still exceed 50-75% for the DDA ensemble in the higher IWP regions. These large IWP uncertainties, however, do not translate into particularly large simulated T_B uncertainties at a scattering sensitive microwave frequency like 157 GHz, and realistic T_{B157} results are obtained using the DDA ensemble despite the large IWP uncertainties. These findings suggest the accuracy of IWP retrievals using passive microwave observations in the 36-157 GHz range may suffer. It must be recognized, however, that IWP uncertainties are largely controlled by the Z_e -IWC relationships of the ice models used in this study, and many of the DDA ensemble members are probably not representative of aggregate particles (from a mass-size perspective) that typically dominate snowfall, even though they seem to adequately capture microwave radiative properties of frozen hydrometeors associated with precipitation. Continued work must be undertaken to both verify the physical mechanism responsible for the results presented in this study – especially isolating the influence of the derived PSD and PSD-averaged single scatter optical properties on simulated brightness temperatures for each ice particle model – and to develop ice models more representative of aggregate-type particles from both a mass-particle size and radiative perspective.

Table 6.1: Description of the different cloud and precipitation categories used for simulation versus observation comparisons. Abbreviations used to denote the categories in various figures and tables are also indicated. The number of CloudSat/AMSR-E/MHS coincident observations for each category (N_{obs}) used to generate the statistics in Fig. 6.7 is also shown.

Cloud/Precip Category	Label	N_{obs}	Description
All clouds	AC	9043	All clouds, no precipitation.
Cold clouds	CC	2494	Cold clouds only (< 0 C), no precipitation.
Warm clouds	WC	2894	Warm clouds only (> 0 C), no precipitation.
All precipitation	AP	5153	All precipitation occurrences.
Stratiform (mid-lat)	SML	1911	Mid-latitude (lat. $> 30^\circ $) stratiform precipitation.
Stratiform (low FL)	SLFL	916	Mid-latitude stratiform, freezing level < 1 km.
Stratiform (high FL)	SHFL	583	Mid-latitude stratiform, freezing level > 1 km.
Stratiform (brightband)	SBB	412	Mid-latitude stratiform with obvious brightband.
Low-topped convection	LTC	1148	Shallow, higher latitude (lat. $> 45^\circ $) convection.

Table 6.2: Lower freezing level mid-latitude stratiform precipitation model error covariances [K^2] (bold; lower left half) and correlations (upper right half) from the 40 dBZ_{int} data bin for the following frequencies: 18V, 23V, 36V, 89V, and 157 GHz.

	18V	23V	36V	89V	157
18V	1.99	0.85	0.74	0.06	0.25
23V	1.70	1.99	0.75	0.13	0.24
36V	1.42	1.44	1.84	0.13	0.11
89V	0.18	0.43	0.40	5.21	0.41
157	0.80	0.75	0.33	2.13	5.13

Table 6.3: Same as Table 6.2, but for higher freezing level mid-latitude stratiform precipitation.

	18V	23V	36V	89V	157
18V	4.51	0.93	0.82	0.07	0.13
23V	3.52	3.17	0.81	0.05	0.09
36V	5.86	4.87	11.39	0.31	0.13
89V	0.57	0.35	4.17	15.79	0.55
157	0.60	0.35	1.00	4.99	5.15

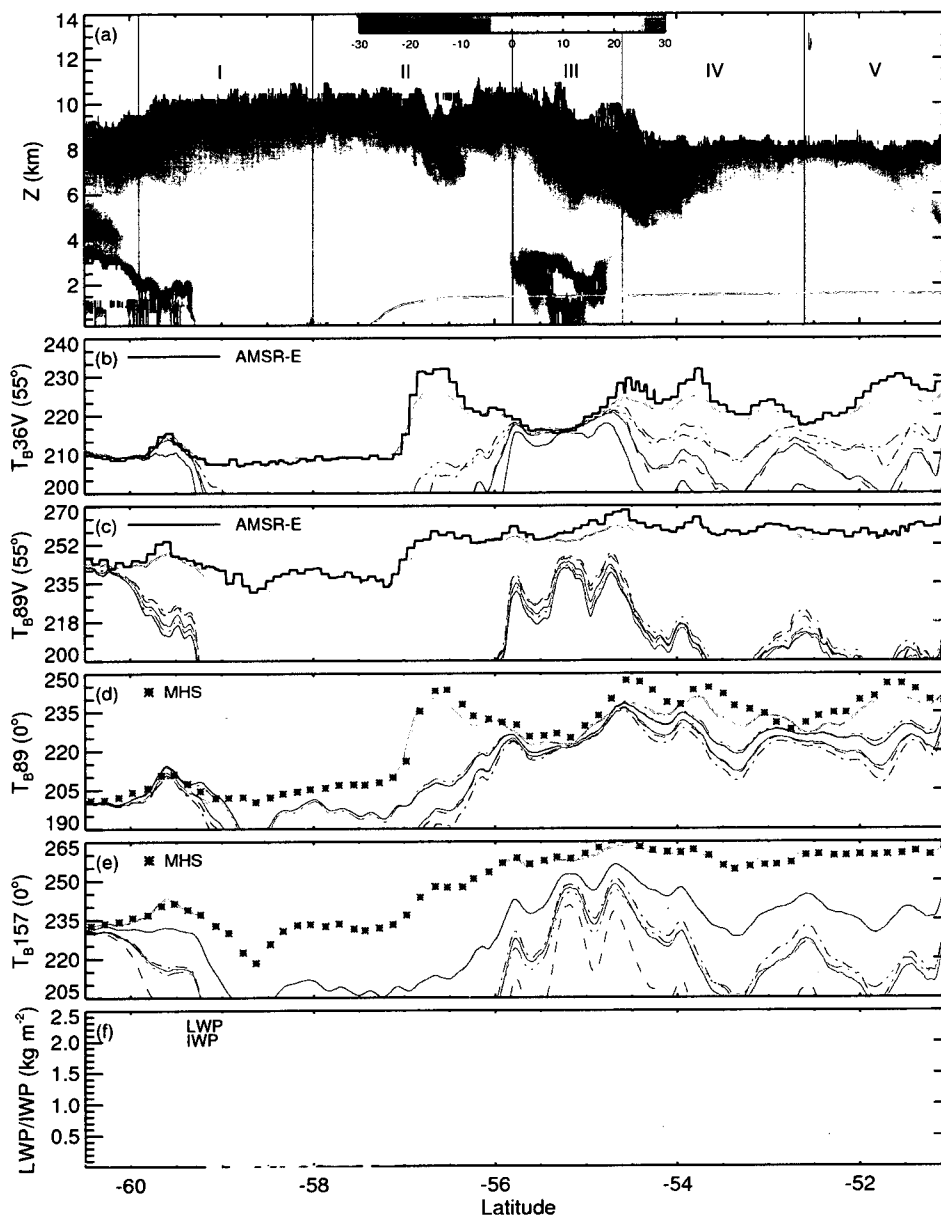


Fig. 6.1: Panel (a) shows the attenuation-corrected CPR reflectivity and freezing level (blue line) from CloudSat orbit 01497, panels (b) to (e) show brightness temperature [K] for the following instruments and channels (black lines/asterisks): (b) AMSR-E 36V and (c) 89V GHz; (d) MHS 89 and (e) 157 GHz. Panel (f) also shows AMSR-E derived LWP (green) and IWP (blue) derived from the DDA ensemble results. Simulated T_b 's for the DDA ensemble and $1-\sigma$ uncertainties (light gray shading), as well as spherical and Kim et al. (2007) models (using same color scheme as Fig. 5.1) are also included in panels (b)-(e). Panel (a) also shows five separate zones that are used for calculating the individual ice habit biases in Fig. 6.6.

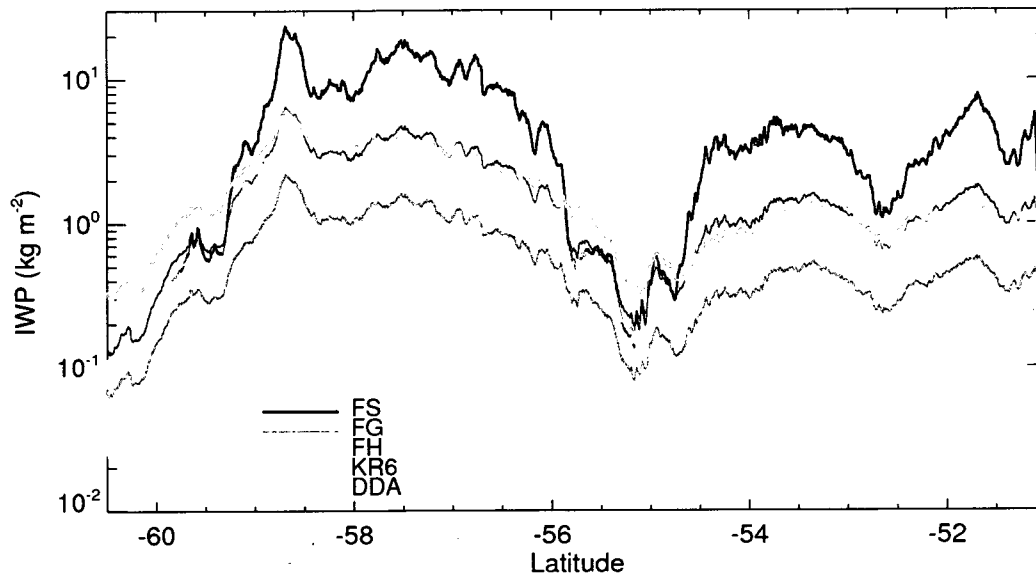


Fig. 6.2: Derived ice water path [kg m^{-2}] for fluffy spheres (FS), graupel (FG), and hail (FH), as well as the Kim et al. (2007) six-arm rosette (KR6). The DDA ensemble average and 1- σ uncertainty results (light gray shading) are also shown.

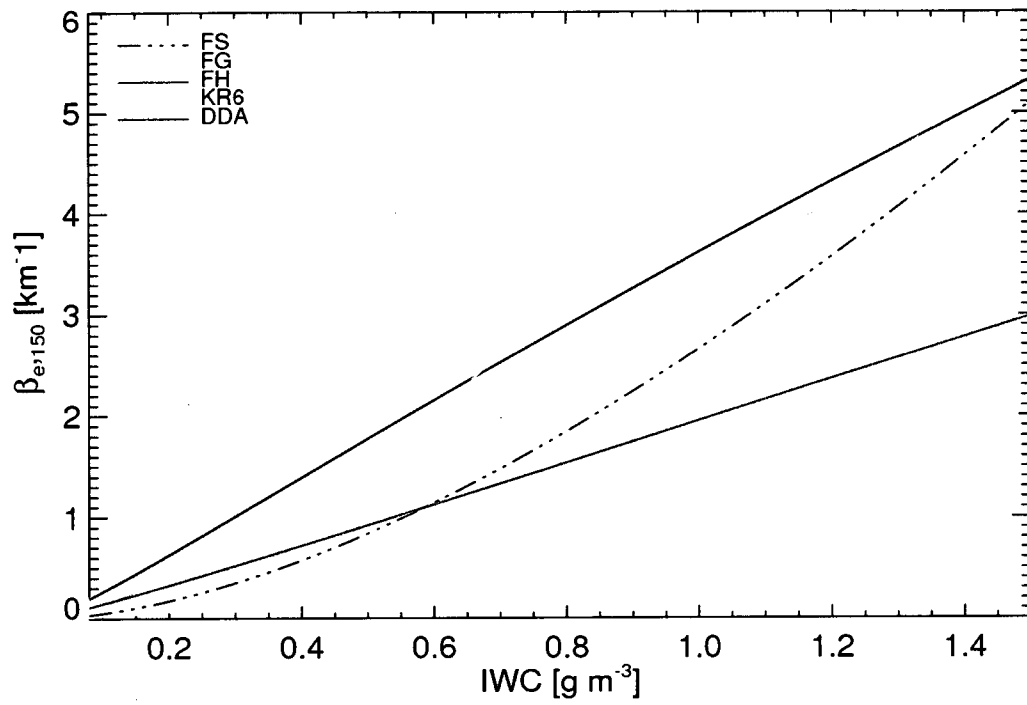


Fig. 6.3: Simulated volume extinction coefficient [km^{-1}] as a function of ice water content [g m^{-3}] for the same ice habits indicated in Fig. 6.2.

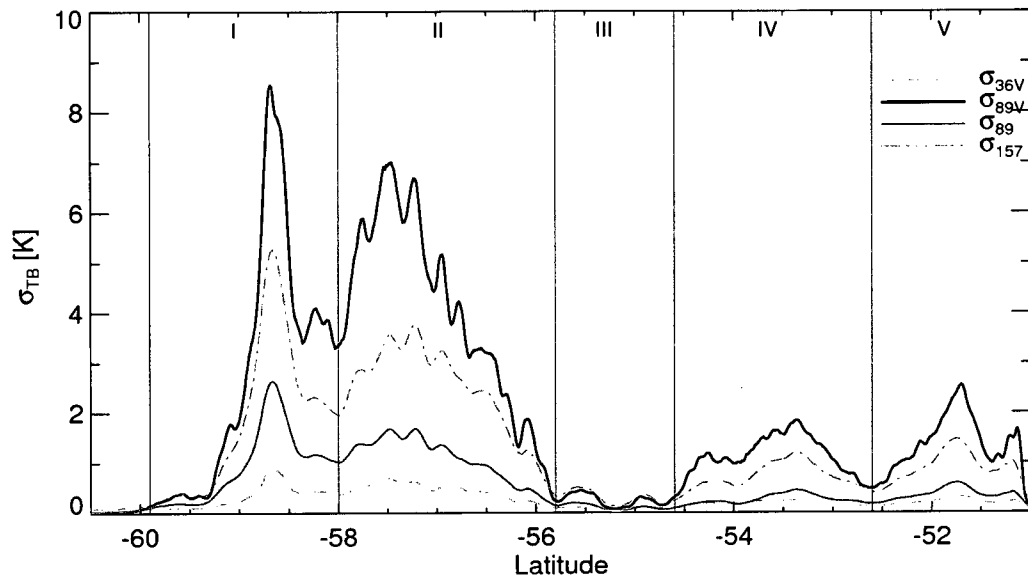


Fig. 6.4: Simulated T_B uncertainties for 36V (light dash), 89V (dark solid), 89 (light solid), and 157 (light dash-dot) GHz. The five separate zones from Fig. 6.1a are also shown.

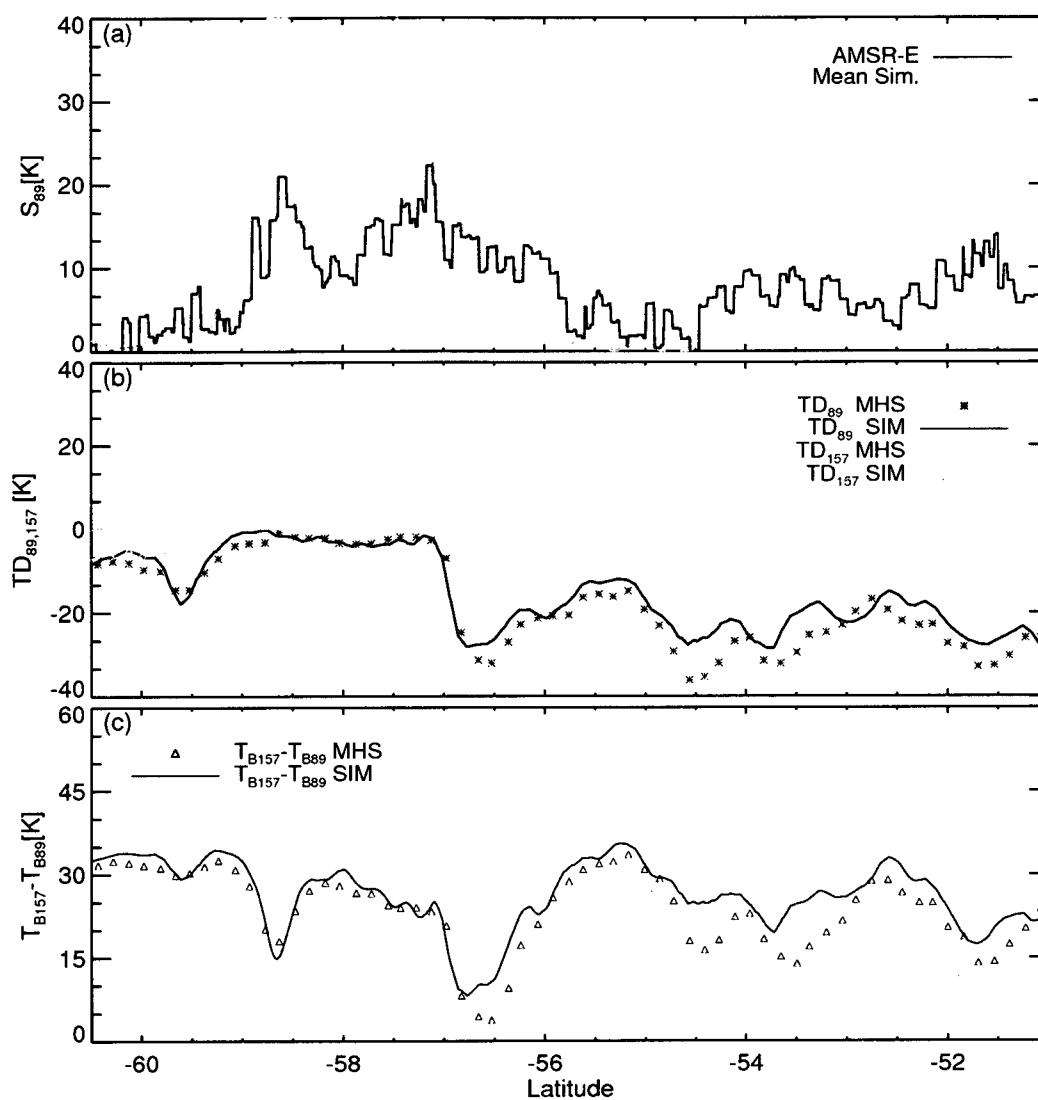


Fig. 6.5: (a) AMSR-E (dark) and simulated (light) scattering index for 89 GHz [K], (b) MHS 89 (dark asterisk)/157 (light diamond) and simulated 89(dark solid line)/157(light solid line) GHz brightness temperature depression [K] compared to water vapor-only results, and (c) MHS (triangles) and simulated (solid line) 157-89 GHz brightness temperature difference [K]. The latitude domain corresponds to Fig. 6.1 for CloudSat orbit 01497.

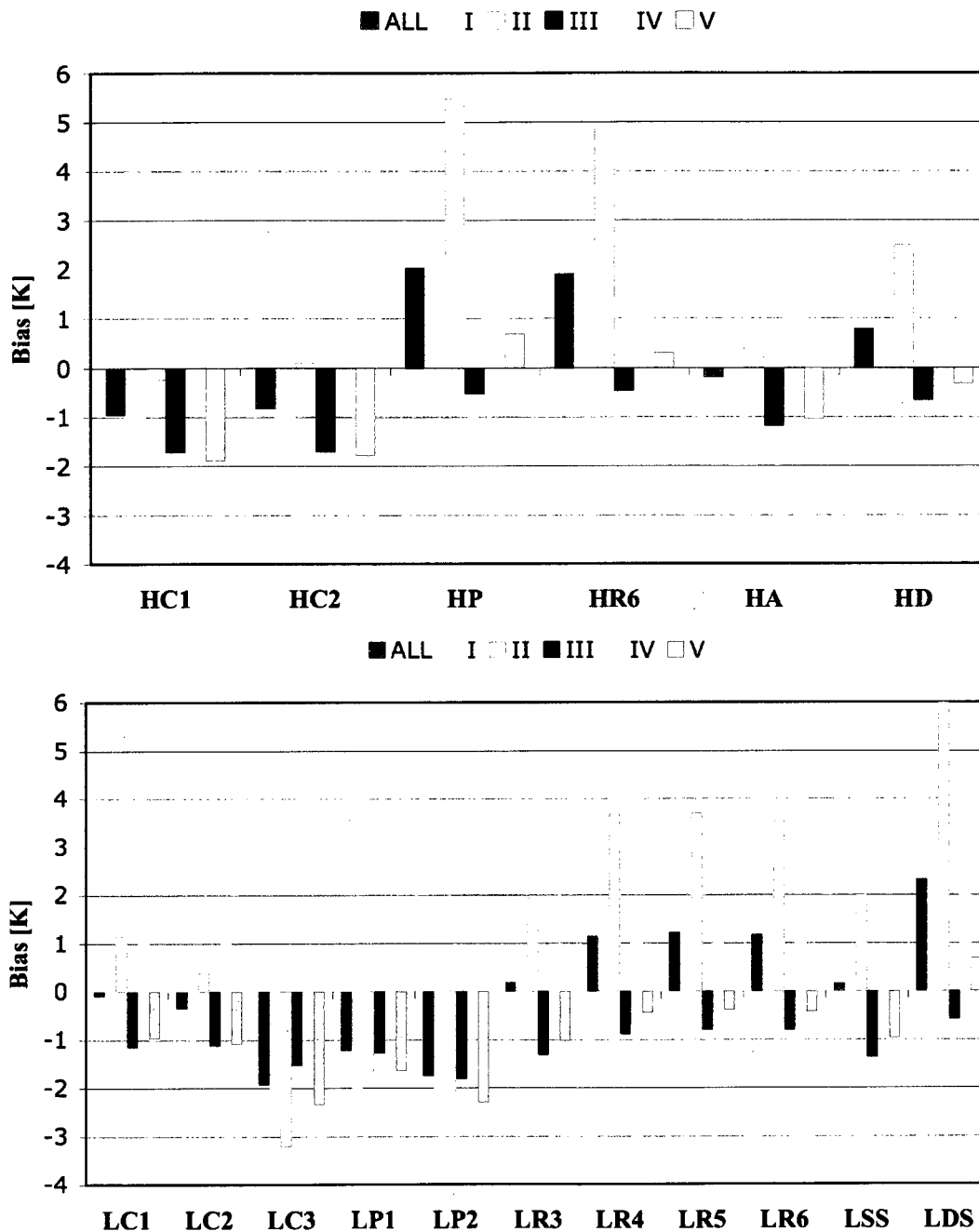
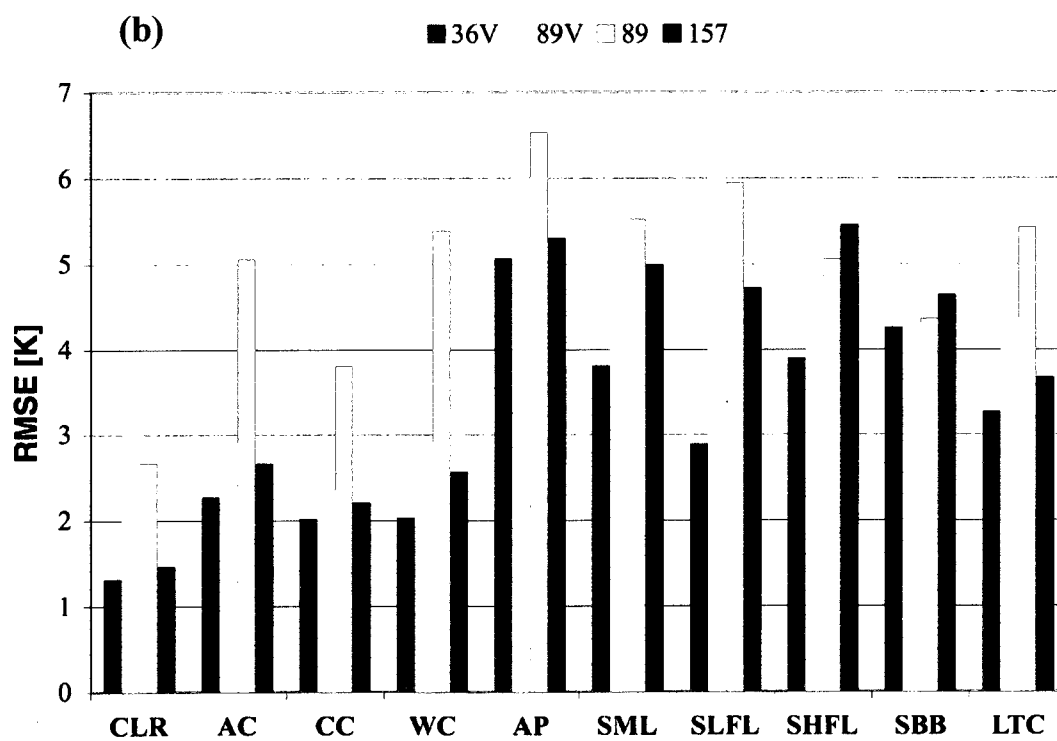
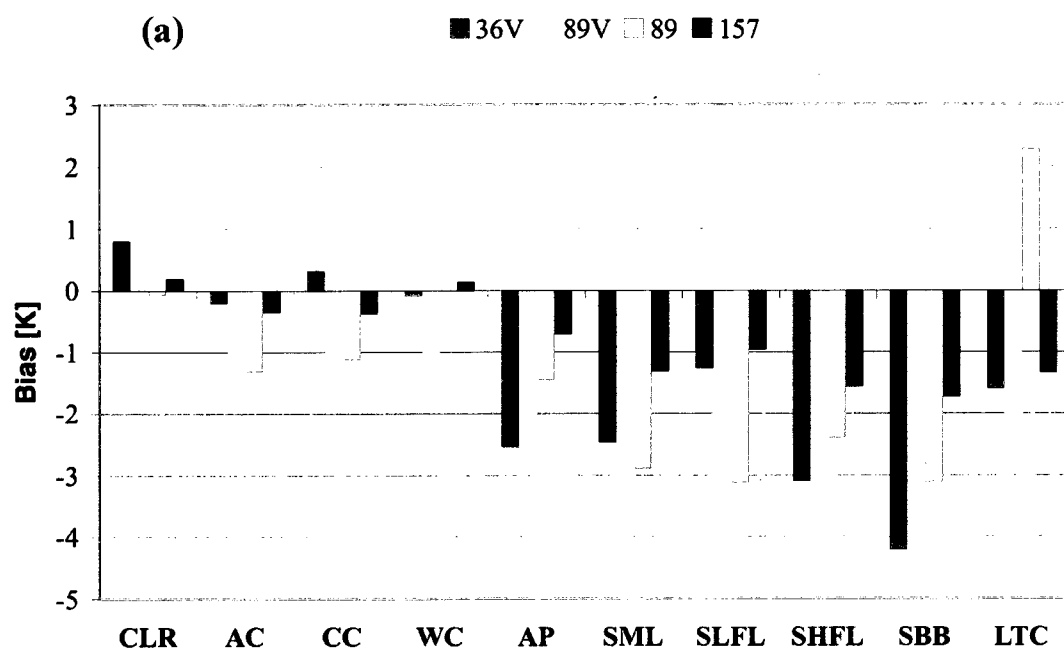


Fig. 6.6: Simulated versus observed 157 GHz brightness temperature bias [K] corresponding to the case study illustrated in Fig. 6.1. The "All" column refers to the entire latitudinal domain shown in Fig. 6.1, while the other columns (I, II, II, IV, V) refer to the regional subsets indicated in Fig. 6.1a. The ice habits follow the same nomenclature as Table 3.1.



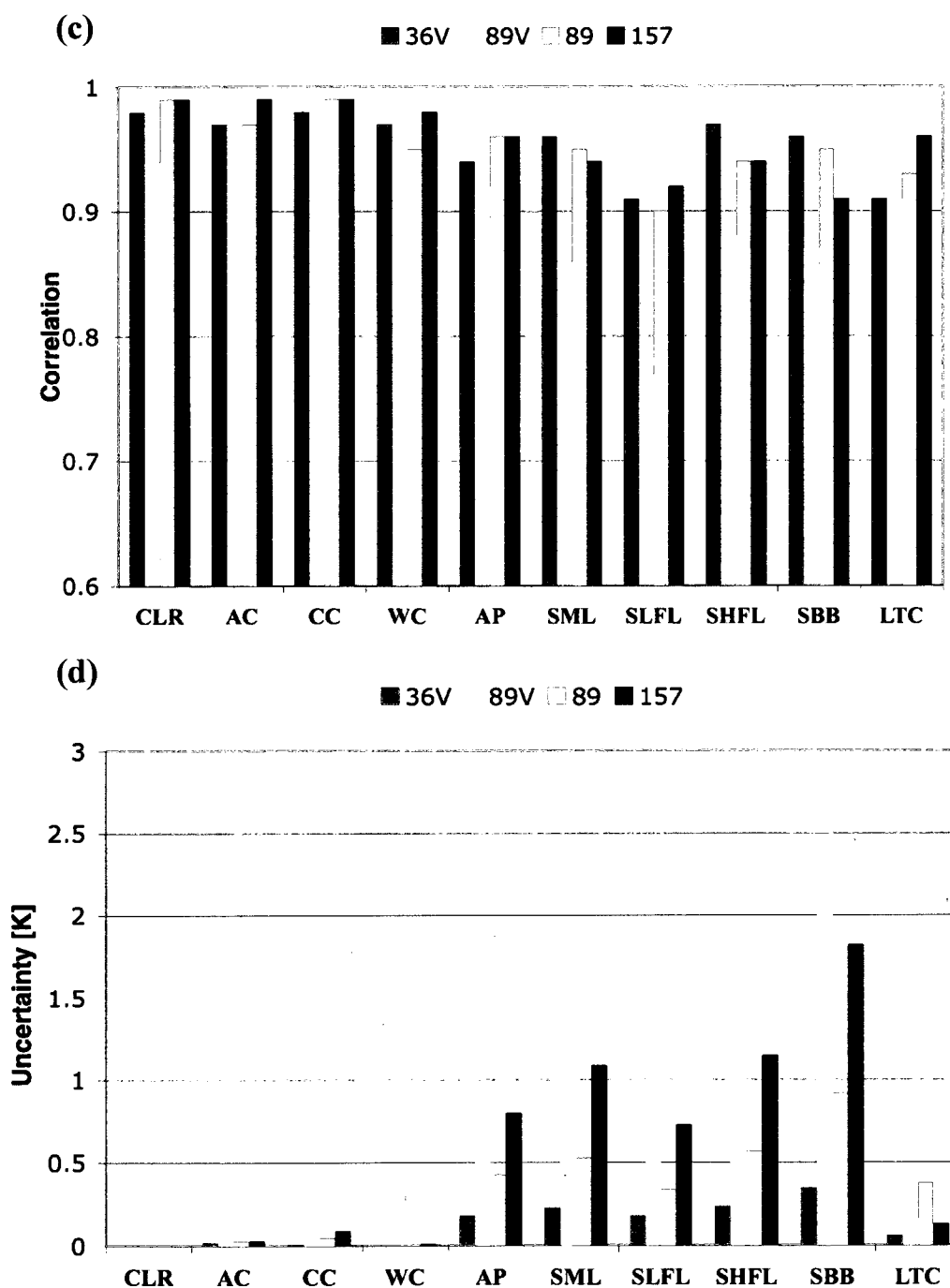


Fig. 6.7: Simulated DDA ensemble brightness temperature versus AMSR-E/MHS (a) bias, (b) bias-corrected root mean square error (rmse), (c) correlation, and (d) average simulated T_B uncertainty ($\bar{\sigma}$) for different cloud and precipitation categories. Abbreviations for the cloud and precipitation categories can be found in Table 6.1.

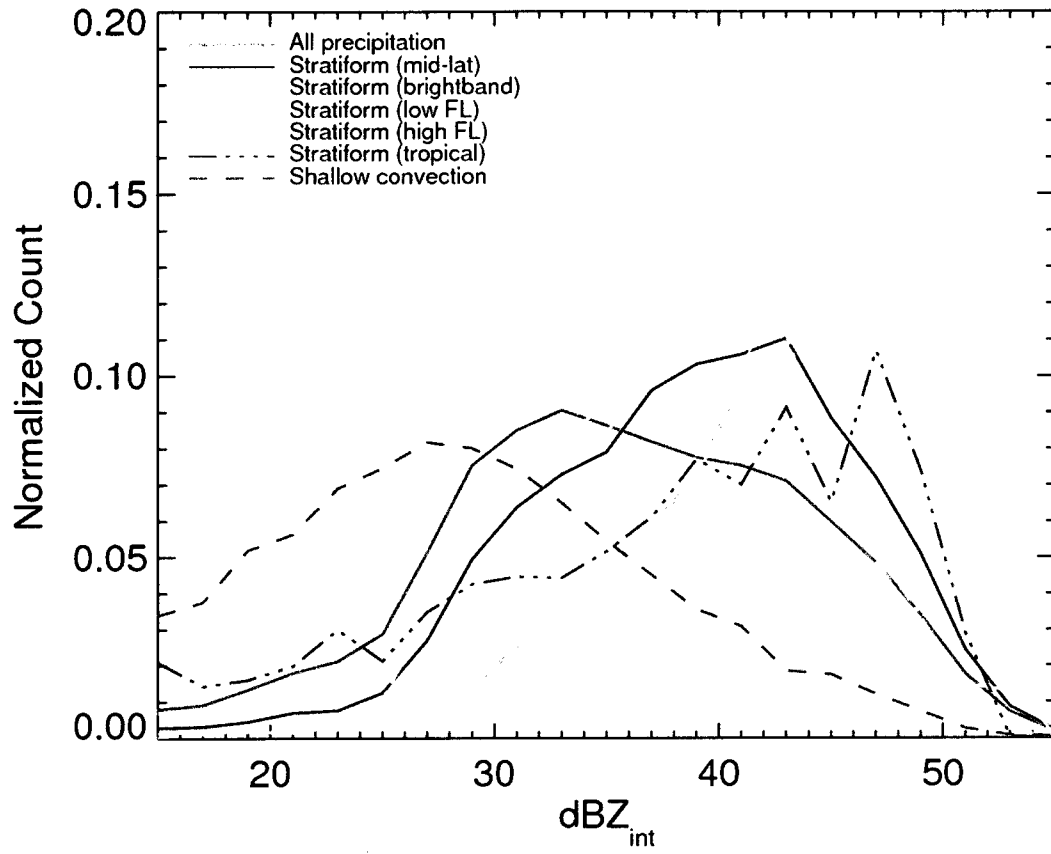


Fig. 6.8: Histograms of column-integrated reflectivity above the freezing level [dBZ] for different precipitation categories in 2 dB bins.

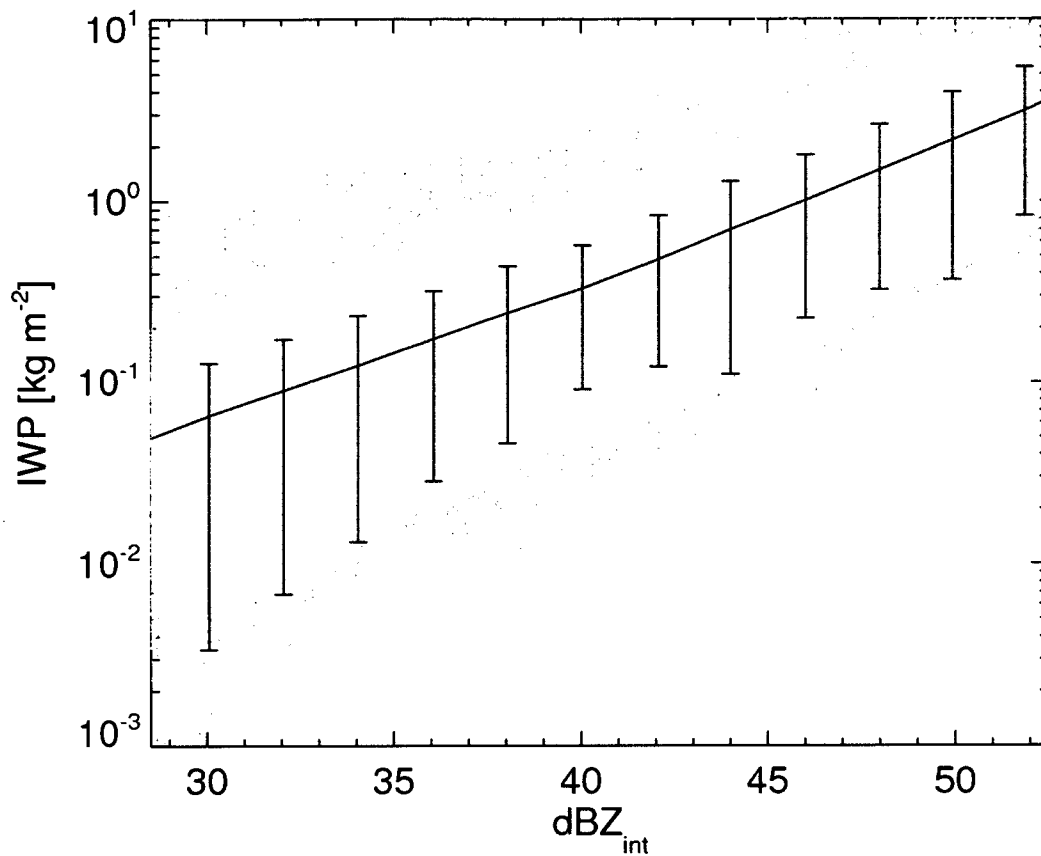


Fig. 6.9: Retrieved ice water path, IWP [kg m^{-2}] versus column-integrated reflectivity above the freezing level, Z_{int} [$\text{mm}^6 \text{m}^{-2}$] (shown in dBZ) for all mid-latitude stratiform cases using the DDA ensemble of ice particles. $1-\sigma$ uncertainties for every 2 dBZ_{int} data bin are also indicated.

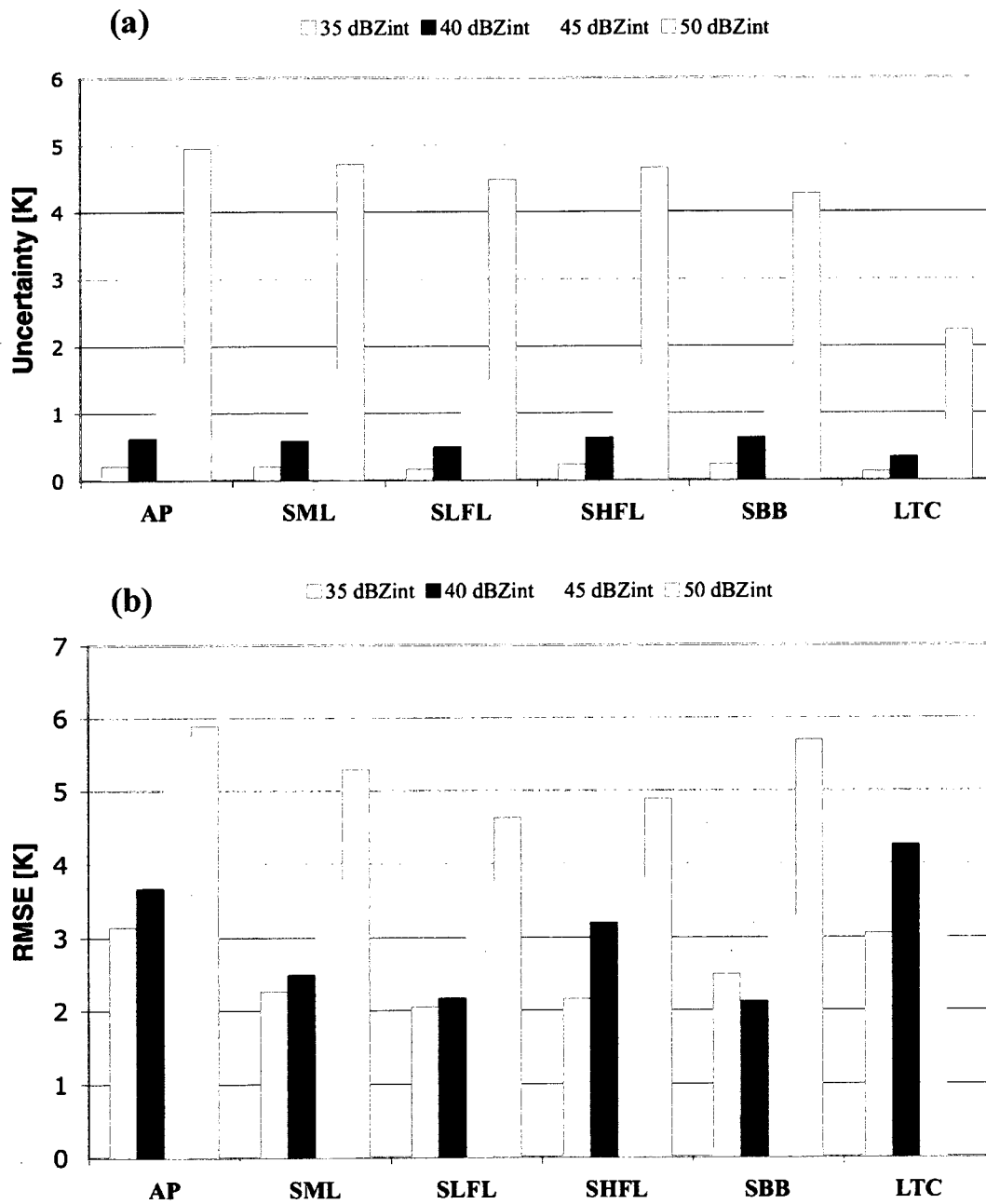


Fig. 6.10: Simulated T_B uncertainty [K] (top) and bias corrected root mean square error [K] (bottom) as a function of Z_{int} for the different precipitation categories listed in Table 6.1.

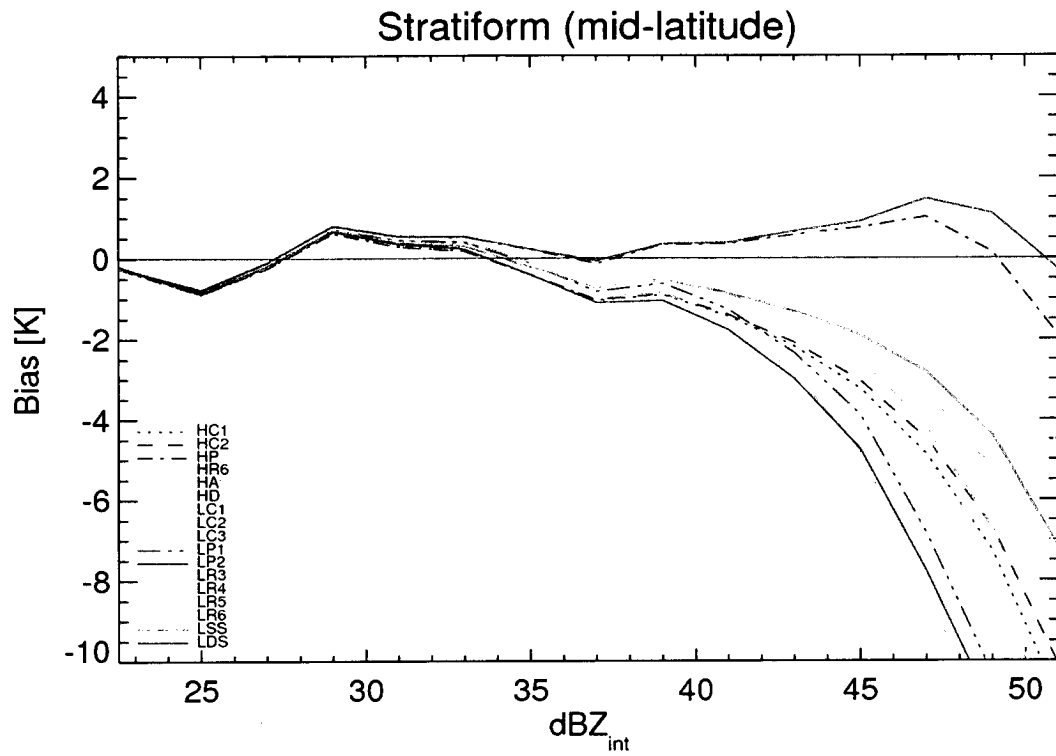


Fig. 6.11: Simulated versus observed 157 GHz brightness temperature bias [K] using the DDA ensemble of ice particle models for the mid-latitude stratiform precipitation category.

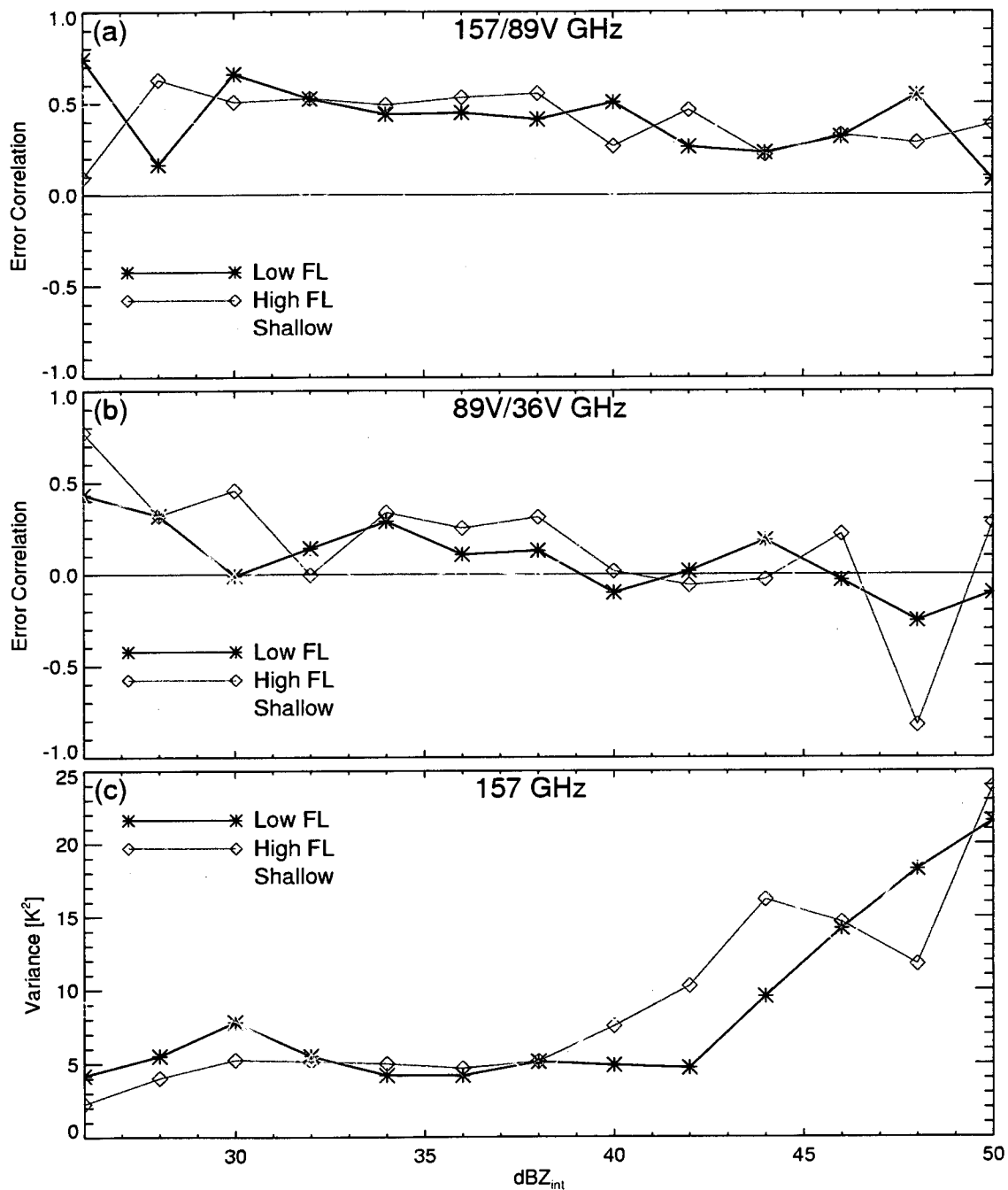


Fig. 6.12: Panels (a) 157-89V and (b) 89V-36V show error correlations for three different precipitation categories as a function of integrated reflectivity above the freezing level (Z_{int}). Panel (c) displays 157 GHz error variances for the same precipitation categories. The low freezing level mid-latitude stratiform (Low FL), higher freezing level mid-latitude stratiform (High FL), and higher latitude, shallow convective precipitation categories are shown (see Table 6.1).

7. Space-borne radar snowfall retrievals

a. Overview

This section focuses on a few critical aspects of active microwave remote sensing of dry snowfall using some of the tools developed in previous sections, and the valuable role of CloudSat data to study these issues is highlighted throughout the paper. Similar to Liu (2008a), CloudSat CPR data are used to analyze the annual cycle of snowfall from a global perspective. Considerable effort is also devoted to describe interesting regional snowfall differences based on the CloudSat snowfall dataset, as well as some complications of using CPR data that may bias snowfall retrievals in certain locations. Additionally, attempts are made to address future snowfall observations by a dual-frequency radar with similar characteristics as the GPM DPR. Current DPR instrument specifications anticipate the MDS for the DPR Ku-PR (13.6 GHz) and Ka-PR (35.5 GHz) will be near 17 and 12 dBZ_e, respectively (Nakamura and Iguchi 2007). While the Ka-PR's higher frequency and lower MDS will enable it to detect lighter precipitation rates than the Ku-PR and TRMM PR, a thorough assessment of its ability to realistically observe snowfall has yet to be undertaken. In an effort to assess a DPR-like instrument's near-surface snowfall detection efficacy, CPR data are used to calculate proxy DPR-like radar reflectivities of global snowfall events, and the possible role of CloudSat data to augment DPR-like snowfall climatologies is explored. Last, sensitivity tests are performed to highlight uncertainties due to the assumed model employed to represent

frozen hydrometeors, and recently published optical property databases of non-spherical ice particle models (Hong 2007a,b; Kim et al. 2007; Liu 2004) are utilized to illustrate this potentially significant source of uncertainty.

b. Data

CloudSat CPR radar reflectivity factor fields in 240 m vertical bins from the official CloudSat 2B-GEOPROF product (Mace 2007), combined with temperature data from the CloudSat ECMWF-AUX product (Partain 2007) gridded to the CPR's resolution, are utilized in this study. For this study, a dataset of potential snowfall events observed by CloudSat between July 2006 and July 2007 was compiled using the following criteria:

(1) CPR reflectivity data were restricted to the 30° to 75° latitude belt in both hemispheres. While the CPR routinely provides data at locations poleward of 75°, this latitudinal limit was chosen to better represent the planned orbit of the core GPM satellite (the proposed ~65° inclination angle of the GPM core satellite will prohibit the DPR's swath from reaching the highest latitudes). Liu (2008a) shows that snowfall occurrence is rare equatorward of 30° latitude, thus providing justification for using this value as a lower latitudinal limit of the dataset.

(2) Following Liu (2008a), only near-surface CPR data were used in the ensuing analysis, with "near-surface" defined as the 6th data bin above the surface (~1.3

km). CPR reflectivity data from the lowest 5 bins were automatically rejected to avoid potential clutter contamination from the surface. Section 7f will provide more discussion about whether this constraint is sufficient enough to reject all clutter events, especially over isolated regions containing complex terrain.

(3) CPR data that coincided with 2 m ECMWF-indicated temperatures at or below 0°C were only considered. Even though previous studies have indicated surface snowfall can be readily expected when surface temperatures are as high as 2°C (e.g., Bennartz 2007; Liu 2008a), the more stringent threshold of 0°C was chosen to reduce the occurrence of partially melted near-surface snow in the dataset and ensure that “dry” snowfall was predominantly sampled.

(4) The near-surface CPR reflectivity field had to exceed a threshold value of -15 dBZ_e, thus all snowfall rate statistics derived from this dataset are “conditional” snowfall rates. Additionally, the reflectivity fields had to possess vertical continuity to be considered as potentially precipitating (vertical continuity was defined as reflectivity exceeding the threshold value of -15 dBZ_e in the 5 data bins immediately above the near-surface data bin). This constraint is added to help eliminate ground clutter contamination. Section 7f includes a short discussion on the sensitivity of the results to varying the degree of vertical continuity required in order for an observation to be accepted in the snowfall dataset.

(5) Any CPR observations with a non-zero 2B-GEOPROF data quality field, which indicated a potentially problematic observation, were rejected.

(6) Similar to Liu (2008a), no attenuation corrections were applied to the reflectivity fields before inclusion into the snowfall dataset. Dry snowfall itself is not highly attenuating at 94 GHz unless the snowfall rates are large and the snowfall layer is thick (e.g., Matrosov 2007). While the CPR can experience high levels of attenuation under certain meteorological conditions (e.g., heavy liquid precipitation, melting precipitation, high cloud liquid water contents, and/or large columnar water vapor amounts), it is assumed that the majority of snowfall cases in this study will be largely immune to severe attenuation effects.

The resulting dataset after applying these conditions was populated by over 4.9 million snowfall occurrences, which comprised about 3% of the total possible CPR observations within the latitude belts considered and 13% of the total CPR observations associated with sub-zero 2 m ECMWF temperatures in the same latitudinal boundaries.

c. Methodology

Appropriate equivalent radar reflectivity factor (Z_e)-snowfall rate (S) relationships are first derived using three different ice particle models (HA, LR3, and SS from Table 3.1). As previously discussed, Z_e - S relationships are used for three primary purposes:

- (1) Reducing the computation time associated with explicitly deriving the PSD for every

CloudSat observation (37,000 profiles in every CloudSat data swath, plus over 100 vertical levels), (2) converting the radar signal (Z_e) to a physically useful geophysical parameter (S), and (3) reconstructing the actual CPR snowfall-related reflectivities to proxy 13.6 and 35 GHz reflectivities given a particular snowfall rate to create a proxy DPR dataset.

The Z_e - S relationships are derived using the two-step process described in greater detail in Section 4.b:

- (1) The ice particle size distribution (PSD) for a specified range of snowfall rates are derived via the Field et al. (2005) ice PSD moment conversion scheme;
- (2) The dependent variable, Z_e , is calculated for a given snowfall rate and ice particle model using the PSD derived in the previous step and ice particle backscattering characteristics from three ice habit models. Final Z_e - S relationships are derived using a power law curve fitting routine.

For this study, the prefactors and exponents in the m - D_{max} (Eq. 3.4) and v - D_{max} (Eq. 4.3) relationships are assumed to conform to the average aggregate properties shown in Fig. 4.2 in order to derive the same underlying PSD for all three ice habits. Fig. 7.1 depicts backscatter cross-sections (σ_b) at 94 GHz for various shapes based on DDA calculations of non-spherical particles (K07; H07; L04), as well as frequency-dependent low-density spherical representations of frozen particles following the approach of Surussavadee and Staelin (2006; SS06). In order to assess the sensitivity of the results to

the assumed frozen particle model, Z_e - S relationships for three different particle shapes at 94.0, 35.0, and 13.6 GHz are derived (Table 7.1). It should be emphasized these idealized ice particle models best represent unrimed – or perhaps lightly rimed – frozen hydrometeors, thus providing further motivation for limiting this study to “dry” snowfall. The L04 three-bullet rosette (denoted as LR3), H07 aggregate (HA) and the SS06 low-density spherical snow particles (SS) were chosen as three representative ice particle models. The LR3 backscattering values generally fall within the middle of the σ_b envelope at 94 GHz (Fig. 7.1), especially at larger particle sizes that contribute most to the calculated reflectivity, and will be used throughout this study as the representative “average” ice particle model. The HA and SS shapes show stronger and weaker backscattering characteristics at 94 GHz, respectively, than LR3 and are utilized to show the sensitivity of the results to other ice particle models and are also considered as plausible upper and lower uncertainty bounds for the entire ensemble of ice particle models.

The Z_e - S relationships are further illustrated in Fig. 7.2. Fig. 7.2a shows the 94 GHz Z_e - S relationships as both a scatter plot and a best-fit power law line that corresponds to the results shown in Table 7.1. The relative error of the best-fit lines is small, with only small differences observed at most Z_e - S pairings. As expected from the σ_b results in Fig. 7.1, the LR3 Z_e - S relationship falls between the HA and SS shapes at 94 GHz, but the resulting Z_e value for a given snowfall rate is extremely sensitive to the ice particle model. For instance, an assumed snowfall rate of 0.1 mm h^{-1} produces corresponding reflectivity values of about 0.14, 0.52, and $1.7 \text{ mm}^6 \text{ m}^{-3}$ for the SS, LR3,

and HA ice models, respectively – a range exceeding 10 dB. At a snowfall rate of 1.0 mm h⁻¹, the potential range of reflectivity values increases to about 14 dB. For this study, it is probably more meaningful to investigate the differences in retrieved values of S given a Z_e observation. As shown in Fig. 7.2b, calculated snowfall rates for the SS, LR3, and HA shapes are about 0.76, 0.22, and 0.10 mm h⁻¹ for a Z_e value of 1.6 mm⁶ m⁻³ (~2 dBZ_e), and 3.55, 0.82, and 0.32 mm h⁻¹ when Z_e is 10.0 mm⁶ m⁻³ (10 dBZ_e). The backscattering properties of the chosen ice model clearly represent a large potential source of uncertainty in retrieving snowfall rates from W-band radar data.

Complicating matters further, note that the Z_e - S relationships for each ice particle change relative to one another as frequency decreases (Fig. 7.2c and d). At 35 GHz, the LR3 Z_e - S curve converges with the SS results at higher snowfall rates. At 13.6 GHz, the LR3 Z_e - S relationship produces similar results as the HA shape at low snowfall rates, and the SS shape at high snowfall rates. (It should be noted that no 13.6 GHz DDA results were available from Hong (2007), so the HA shape's σ_b results at this frequency were scaled directly from the SS 35 GHz σ_b results.) Overall, these results highlight the complex shape-dependent transition of PSD-averaged backscattering behavior from higher to lower frequencies resulting from each shape's distinctive deviation from Rayleigh scattering behavior, especially at higher frequencies.

Table 7.1 also indicates three other recently published Z_e - S relationships for the frequencies of interest (Noh et al. 2006; Matrosov 2007; Liu 2008a). There are noticeable differences between the current results with these recent studies at all frequencies. The choice of ice particle model explains some of these differences. The

Noh et al. (2006) and Liu (2008a) studies both use DDA results from Liu (2004, 2008b), similar to this study. However, Noh et al. (2006) considers dendrite and sector snowflakes exclusively, while Liu (2008a) uses a best fit of all Liu (2004, 2008b) rosette shapes, plus sector and dendrite snowflakes, to derive the Z_e - S relationship. The Matrosov (2007a) Z_e - S relationships are not derived using with the DDA approach, but instead model aggregate snowflakes as spheroids combined with the T-matrix method to calculate backscattering coefficients. Differences between the current study and these related works can also be partially attributed to the PSD utilized, as Noh et al. (2006), Matrosov (2007) and Liu (2008a) all employ exponential PSD's that differ from the Field et al. (2005) PSD used in this study. Matrosov (2007) also notes considerable variability in Z_e - S relationships when the assumed aspect ratio of the model spheroid is changed, or when the mass/fall-speed relationships are altered to mimic the variability in observed aggregate masses and fall speeds. The overall variability in σ_b and Z_e - S relations illustrated in Fig. 7.1 and Fig. 7.2, however, combined with possible PSD effects, appear to dominate these other sources of potential uncertainty.

The derived 94 GHz Z_e - S relationships for the LR3 shape shown in Table 7.1 are used to convert CloudSat CPR near-surface radar reflectivity observations to snowfall rates. Once the snowfall rates are known for each CPR observation, corresponding proxy DPR-like reflectivities are calculated using the derived 35.0 and 13.6 GHz Z_e - S relationships. It should be acknowledged that the DPR will be a scanning radar capable of producing a much larger data swath than CloudSat's CPR, so the proxy DPR-like

database of snowfall events presented here assumes all statistics and comparisons are made using only the nadir viewing angle.

d. Global Results

The CPR 94 GHz near-surface reflectivity distribution in 1 dBZ_e data bins for global dry snowfall events located between the 30-75° latitudinal belts is shown in Fig. 7.3a. The CPR distribution peaks near the 3 and 4 dBZ_e bins, while an estimated 94% of all CPR near-surface radar observations in the snowfall dataset are less than 10 dBZ_e. It should be noted that this percentage also assumes a lower threshold of -10 dBZ_e corresponding to a snowfall rate of about 0.03 mm h⁻¹ (assuming the LR3 Z_e-S relationship), since radar reflectivities lower than about -10 dBZ_e do not contribute significantly to the total snowfall accumulation (see Fig. 7.3b). These results highlight the prevalence of very light radar reflectivities associated with dry snowfall and hint at potential detection difficulties using active remote sensing instruments operating a lower frequencies and with a higher MDS than the CPR. To better assess the detection efficacy of global snowfall by a DPR-like instrument, the 35 and 13.6 GHz reflectivity distributions that were calculated using the LR3 Z_e-S relationships in Table 7.1 are also indicated in Fig. 7.3a. The histograms for these two lower frequencies peak at the higher reflectivity bins of near 6 and 7 dBZ_e, respectively, due to the differing Z_e-S relationships shown in Table 7.1. Even though the peak reflectivities are shifted higher, the ability of a 35/13.6 GHz radar to observe snowfall may be limited by their MDS. The portion of the reflectivity distribution that can be captured by a 35 GHz instrument with a MDS of

12 dBZ_e is indicated in Fig. 7.3a and clearly shows the potential undercount of global snowfall events by a 35 GHz radar, and only about 7.1% of the reflectivity values associated with near-surface snowfall would be detected (Table 7.2). A 13.6 GHz instrument with a MDS of 17 dBZ_e is even less sensitive to snowfall and would potentially capture only about 1.2% of the near-surface snowfall cases (Table 7.2). Similar to the CPR 94 GHz results presented earlier, these percentages are calculated assuming measurable snowfall results from a near-surface reflectivity exceeding -9 and -8 dBZ_e at 35 and 13.6 GHz (which corresponds to a snowfall rate of 0.03 mm h⁻¹ assuming the LR3 Z_e-S relationship), respectively.

An alternative, and arguably more physically significant, perspective of global snowfall is shown in Fig. 7.3b, which highlights both the distribution of conditional snowfall rates and the cumulative density function of average conditional snowfall rate (which serves as a proxy for snowfall accumulation) that reveals how much each snowrate bin contributes to the conditional global snowfall rate. The snowfall rate bins are derived directly from the CPR reflectivity observation bins shown in Fig. 7.3a using the LR3 94 GHz Z_e-S relationship in Table 7.1. According to Fig. 7.3b, the average conditional global snowfall rate is near 0.3 mm h⁻¹. Assuming a MDS of 17 and 12 dBZ_e, 35 and 13.6 GHz instruments will only be sensitive to snowfall rates greater than about 0.76 and 1.27 mm h⁻¹, respectively, which translates to about 80% and 94% of the total global snowfall accumulation being missed by a DPR-like radar based on the cumulative distribution curve shown in Fig. 7.3b.

e. Sensitivity to particle type

The sensitivity of the global radar reflectivity and snowfall rate distributions to assumed particle type is shown in Fig. 7.4. At 35 GHz, noticeable shifts in the radar reflectivity histograms to higher values are evident if the HA and SS Z_e - S relationships are used instead of the LR3 shape. The HA histogram peaks near 8 dBZ_e, while the SS histogram peaks near 12 dBZ_e and substantially broadens. From a radar reflectivity detection standpoint, both of the scattering characteristics of these shapes would allow a 35 GHz active radar to observe more snowfall compared to the LR3 histograms shown in Fig. 7.3, and the detection rate increases substantially to about 18% and 41% for the HA and SS shapes, respectively. At 13.6 GHz, the SS distribution again shifts to higher reflectivity values, peaking near 16 dBZ_e, and increases the potential detection rate significantly to about 33% (versus only about 1.2% for the LR3 shape). The HA shape, however, peaks lower than the LR3 distribution at 13.6 GHz and would have a reduced the detection efficacy of under 1%.

The conditional snowfall rate histograms and cumulative plots shown in Fig. 7.4c and Fig. 7.4d enable both an assessment of the physical reality of each particle shape and a crude error estimate from an average global snowfall rate perspective. The snowfall rate distributions for each shape are clearly different, as the LR3 snowfall rate distribution is bounded by the HA snowfall rates at the lower end and SS at the higher end (Fig. 7.4c). According to Fig. 7.4d, the average global conditional snowfall rate is near 0.28 mm h⁻¹ based on the LR3 shape, but large deviations from this value of 60 (HA) to 300% (SS) are possible depending on what particle shape is chosen. The

potential detection rate of accumulated snowfall for a DPR-like radar is also very sensitive to the particle shape and increases markedly for the HA shape at 35 GHz and the SS shape at both frequencies.

A natural question to pose is what particle model produces the most physically realistic results, and is the assumption of the LR3 shape as a representative “average” value valid? Liu (2008a) showed reasonable comparisons between calculated yearly accumulation statistics averaged over a large expanse of Canadian and historical ground-based observations. From this comparison, the LR3 shape used in this study probably produces the most plausible results out of the three shapes considered, as the SS average conditional snowfall results seem skewed much too high and the HA too low, but more comparisons with other independent measurements are needed to further address this issue. Overall, these sensitivity tests illustrate the large potential uncertainty in snowfall retrievals based exclusively on the choice of ice particle model.

f. Sensitivity to vertical continuity threshold

Recall from Section 7b that a vertical continuity threshold is applied in the screening process to select CPR snowfall observations since precipitation-producing clouds are likely to possess some degree of vertical development. Also, ground-clutter tends to display limited vertical structure, so a secondary motive is to introduce further safeguards to reduce contamination by ground returns.

Fig. 7.5 illustrates the sensitivity of the global CPR histograms to the assumed vertical reflectivity structure threshold. As shown in Fig. 7.5a, the low end of the distribution is drastically altered if this threshold is reduced to ~ 0.5 km or completely eliminated, and the resulting histograms are skewed to much lower reflectivity values that peak near the -1 and -10 dBZ_e reflectivity bins, respectively. These changes to the reflectivity distributions are also reflected in the total number of snowfall counts (Fig. 7.5c) that increase tremendously as the vertical threshold is relaxed to ~ 0.5 km (increases $\sim 44\%$) or removed (increases $\sim 80\%$). The addition of such a large quantity of lower reflectivity observations depresses the conditional average snowfall rate shown in Fig. 7.5d by about 21% (0.5 km threshold) and 36% (no threshold) compared to the default threshold.

The upper end of the reflectivity distribution is also sensitive to the vertical continuity threshold, although it is not readily evident in Fig. 7.5a. If the ordinate in Fig. 7.5a is changed to a logarithmic scale, noticeable secondary maxima near 25 dBZ_e appear in each of the distributions (Fig. 7.5b). As will be discussed in greater detail in the next section, these secondary maxima are likely due to ground clutter. Recent studies have also indicated that 94 GHz precipitation-related reflectivities cannot exceed a threshold of about 25 dBZ_e due to the potential dampening effects of resonant Mie scattering (e.g., Matrosov 2007; Hudak et al. 2008), thus lending further support that the secondary CPR observational maxima near 25 dBZ_e in Fig. 7.5b is not due to precipitation. While the frequency of occurrence of these potential clutter-contaminated entries in the snowfall dataset is substantially less than the counts tallied at the lower end of the reflectivity

distribution when the vertical continuity threshold is eased, they can significantly influence the retrieved average conditional snowfall rates, especially on a regional basis (see Section 7g for more details). The effectiveness of the vertical reflectivity threshold in reducing clutter contamination is clearly illustrated in Fig. 7.5b. The secondary frequency of occurrence maxima with no vertical threshold is lowered by over an order of magnitude when the 1 km vertical threshold is utilized. Furthermore, the reduction is not as substantial for the 0.5 km threshold case, thus justifying the more stringent vertical continuity threshold to help mitigate clutter contamination. Note, however, that the 1 km vertical continuity threshold does not completely remove the occurrence of the elevated reflectivities above 20 dBZ_e, so further quality control measures must be taken to further reduce their effect on retrieved snowfall rates (see Section 7g).

The detection statistics for a DPR-like instrument shown in Table 7.1 are also affected by the assumed reflectivity depth constraint, as the percentage of near-surface 35/13.6 GHz reflectivities exceeding 12/17 dBZ_e would decrease from 7.1%/1.2% to 5.0%/1.0% due to the increased reflectivity counts at the lowest part of the reflectivity distributions shown in Fig. 7.5. Interestingly, the percentage of total snowfall accumulation detected would increase by 5-10% if no vertical threshold is applied, which seems counterintuitive if there are substantially lighter snowfall rates contributing to the total global snowfall accumulation. This paradox, however, is again related to the secondary maximum in the reflectivity distribution exceeding about 20 dBZ_e associated with ground clutter that artificially inflates the results. If a quality-control step is

introduced to partially correct some of these inflated values, the snowfall detection percentages fall substantially when the vertical continuity thresholds are removed.

These sensitivity tests raise a few important points. First, there is a distinct possibility the vertical continuity constraint is too restrictive in this study, and some snowfall counts are being rejected. But as shown in Fig. 7.5, most of these rejected snowfall occurrences reside at the light end of the reflectivity/snowfall rate spectrum. However, the sheer number of these rejected cases could possibly contribute a substantial, or at least non-negligible, amount to the total global snowfall accumulation. If this is the case, the global near-surface detection values for a DPR-like instrument shown in Table 7.2 would decrease, and the results shown in this study would be conservatively located at the high end of the potential DPR-like detection rate. Additionally, since the near-surface reflectivity is defined as ~ 1.3 km above the surface in this study, and removing any vertical reflectivity structure threshold significantly increases the number of near-surface snowfall counts, there may be a substantial mode of global shallow snowfall. This topic bears further study since no definitive conclusions can be drawn from this analysis. But great care must be taken when analyzing the CPR data without any vertical reflectivity continuity thresholds, as significant ground clutter contamination exists in such a dataset without applying additional safeguards.

g. Regional results

A regional perspective of snowfall detected by the CPR and the corresponding proxy DPR-like reflectivity and snowfall rate distributions is indicated in Fig. 7.6. These remote regions were chosen because CloudSat observations – and future missions like GPM – provide extremely valuable information in regions previously devoid of routine active remote sensing observations of snowfall. While passive microwave observations of these regions are comparatively plentiful, snowfall retrieval – especially light snowfall over continental regions – by passive microwave methods is extremely difficult (e.g., Kongoli et al. 2003; Skofronick-Jackson et al. 2004; Kim et al. 2008). The regions illustrated in Fig. 7.6 also display a relatively high frequency of snowfall occurrence (Liu 2008a), thus providing further motivation for selecting these specific locations. Since the CPR dataset utilized in this study only extends to 75° N/S, “Greenland” is assumed to be all land regions on Greenland located south of 75° N, while the “Greenland Ocean” region includes all over-ocean observations near Greenland (bounded by $58/75^{\circ}$ N latitude and $62/18^{\circ}$ W longitude). “Antarctica” describes all CPR observations north of 75° S (i.e., only the northern periphery of continental Antarctica). The North-Central Russia region is bounded by $58/75^{\circ}$ N latitude and $75/100^{\circ}$ E longitude and includes exclusively continental observations.

Fig. 7.6 highlights the inherent variability in the radar reflectivity distributions between the selected regions. The reflectivity histograms of the land regions are dominated by very light CPR reflectivities over Greenland, North Central Russia, and Antarctica, while snowfall over the ocean environs surrounding Greenland exhibits higher intensities than the adjacent land regions, similar to the findings of Liu (2008a).

Table 7.2 and Fig. 7.6 combine to show the tremendous variability in the percentage of reflectivity values exceeding the assumed MDS at 35 and 13.6 GHz, as well as the percentage of the average snowfall rate that would be captured by a DPR-like instrument, for each region. The following sub-sections highlight some interesting details that emerge from analyzing these data, with special attention paid to the Greenland dataset.

i. GREENLAND

The 94 GHz CPR-derived reflectivity histogram for Greenland peaks between -1 and 1 dBZ_e (Fig. 7.6a), so very light reflectivities dominate this regional distribution. The converted 35/13.6 GHz reflectivities are greater than or equal to 12/17 dBZ_e at about an 8%/3% rate, which is slightly higher than the global results (Table 7.2). The Greenland data display an interesting subtle secondary reflectivity maximum between 20 and 30 dBZ_e in Fig. 7.6a. This feature is also evident in the conditional snowfall rate histogram and appears more prominently in the average conditional snowfall rate that almost doubles its value due to snowfall rates exceeding about 10 mm h⁻¹ (Fig. 7.6b). These extremely intense snowfall rates produce impressive detection rates from a DPR-like instrument of about 48%/39% of the total snowfall accumulation that are abnormally large compared to the global values in Table 7.2.

The CPR data were closely inspected to find the cause of these high reflectivity values. Greenland can receive very large snowfalls, especially on its southeastern edge (Hanna et al. 2006), but the snowfall rates contributing to the large average snowfall rate value in Fig. 7.6b seem physically improbable. Therefore, the entire CPR snowfall

dataset was searched for reflectivity values exceeding 25 dBZ_e. Almost 1,400 instances of elevated reflectivities were found that represented only about .03% of the entire dataset, and 60% of these aberrant values occurred over Greenland. A handful of other regions like the Andes Mountains, the Canadian Rocky Mountains, the Himalaya Mountains, and some parts of Antarctica – all regions of complex terrain with potential snow and ice-covered surfaces – preferentially contained these anomalous reflectivity values as well.

Fig. 7.7 illustrates actual CPR data (6th bin above the surface and higher) for three cases over Greenland. The black line indicates the surface height taken directly from the 2B-GEOPROF product. These cases all contain very light reflectivities aloft (generally under 10 dBZ_e), although Fig. 7.7b does contain some reflectivities exceeding 15 dBZ_e that are indicative of heavier snowfall (e.g., near 3 km altitude at ~60.3°N). However, note the numerous exceedingly high near-surface reflectivities approaching 30 dBZ_e in numerous locations that are obviously unphysical. Also note that Fig. 7.7a and Fig. 7.7c are almost the exact same overpass location on different dates, and the same signatures appear in both plots in regions of complex terrain. Interestingly, some of the signatures in Fig. 7.7b do not appear to coincide with highly structured terrain, but these are areas where the elevation database may not be trustworthy in remote, complex topographic regions, and official CloudSat data literature does indeed warn of potential errors in the elevation database (Li et al. 2007). It should be noted that many of these potentially contaminated CPR observations are embedded within legitimate snowfall with significant vertical structure, thus making it very difficult to detect without using more complex

vertical reflectivity gradient tests to identify ground clutter signatures. Melting snow could also possibly cause elevated reflectivities, but, as indicated in Fig. 7.7, this does not appear to systematically occur over Greenland or the other regions mentioned.

In an attempt to mitigate the clutter contamination problem, all near surface CPR observations exceeding 20 dBZ_e were replaced with data from the 8th data bin above the actual surface instead of the 6th bin. As shown in Fig. 7.6b, this rudimentary quality-control method completely removes the large increase in average snowfall rate above the 10 mm h⁻¹ snowrate bin. Table 7.2 also indicates corrected values in bold print for the various percentages with most of the clutter eliminated. The total accumulation percentages detected by a DPR-like instrument decrease substantially to about 22%/7% for the 35/13.6 GHz frequencies. Also note that the global total accumulation detection percentage values in Table 7.2 were affected by the small amount of clutter contaminated near-surface reflectivity data points, but the reflectivity percentages were not significantly altered.

ii. GREENLAND OCEAN

As previously mentioned, the Greenland ocean environment produces consistently higher radar reflectivities associated with snowfall, as the peak CPR 94 GHz reflectivity bin is located near 5 dBZ_e. The Greenland oceanic region contains the highest percentage of 35 GHz radar reflectivities exceeding 12 dBZ_e (11.8%) and total snowfall accumulation detected by 35 and 13.6 GHz frequency measurements (27.3 and 8.8%, respectively). The conditional average snowfall rate of near 0.34 mm h⁻¹ is about 30%

higher than the related value over Greenland. Note that this region displays some of the highest snowfall frequency occurrence values and the most intense snowfall on the entire globe (Liu 2008a). The detection statistics of a DPR-like instrument for the Greenland oceanic region can therefore be considered as a best-case regional scenario.

Surprisingly, ground clutter affected the Greenland ocean dataset, as indicated by the secondary increase in average conditional snowfall rate in Fig. 7.6d that is similar to continental Greenland. Two clusters of data points were discovered over near-coastal Greenland regions that were apparently misclassified as ocean instead of land and were the source of the excessive clutter contamination. These clusters appear to be located within a few elevated conditional mean reflectivity pixels in the Liu (2008a) study and may have artificially inflated their results as well.

iii. ANTARCTICA AND NORTH CENTRAL RUSSIA

The conditional average snowfall rates retrieved over these continental regions are very similar and much lighter than the Greenland land and ocean regions (Fig. 7.6f and Fig. 7.6h). Note, however, that the reflectivity and snowfall rate histograms are very different between these two locations. North Central Russia's histogram peaks near the 1 dBZ_e data bin, while Antarctica's is much lower at about -3 dBZ_e (Fig. 7.6e and Fig. 7.6g). Antarctica's 94 GHz reflectivity distribution is much broader than North Central Russia, though, which has major implications for how a DPR-like instrument would observe the snowfall over each area. A DPR-like radar would have difficulty retrieving much snowfall over North Central Russia, as its near-surface reflectivity detection

efficacy is about 2.4%/0.2% for 35/13.6 GHz (Table 7.2), while Antarctica is substantially improved at 35 GHz (4.8%) and slightly better at 13.6 GHz (0.9%) due to its broad reflectivity distribution shape. The percentage of total accumulation that could be observed by a DPR-like instrument is 16.2%/4.3% for Antarctica, which is very near the global averages, while North Central Russia is much lower (5.8%/0.5%). Note that North Central Russia is also not affected by ground clutter contamination, but Antarctica is susceptible to it. The North Central Russia and Antarctica comparison highlights the importance of knowing regional differences in the snowfall rate distributions, as one might conclude these regions would be similarly sampled by an active space-borne radar based on their comparable conditional average snowfall rates.

h. Summary

With the advent of CloudSat, global radar observations of snowfall are for the first time possible. Such observations arrive at an especially crucial time, as pressing scientific issues related to the rapid and dramatic effects of climatic change at higher latitudes make sustained monitoring of global snowfall extremely important in the coming years. The main goals of this study were to highlight the utility of global CloudSat snowfall observations, illustrate interesting regional differences in the reflectivity and retrieved snowfall rate distributions, provide necessary guidance related to how future space-borne radars may observe snowfall on a global and regional basis,

and address some of the uncertainties associated with active, space-borne snowfall retrievals.

Properly characterizing the scattering properties of snowfall remains one of the largest sources of uncertainty related to snowfall retrieval. In the last few years, various authors have developed databases of optical properties of non-spherical precipitation-sized ice particles. One goal of the present study was to attempt to summarize these efforts and address the question of how different retrieved snowfall rates and accumulations depend on the chosen ice microphysical model. It is shown that the annually and globally averaged conditional dry snowfall rate varies significantly depending on what ice scattering model is used. Some of the more unlikely ice particle shapes with extreme backscatter behavior, such as precipitation-sized droxtals, might be disregarded using heuristic arguments. However, the remaining spread of backscattering properties from various frozen particle models is significant. Clearly, based on the sixty-plus years of experience with regular weather radars, a unique, globally valid answer is unlikely to be found. Thus, efforts to estimate and report uncertainties and errors associated with snowfall observations are highly desirable. Further studies should, in particular, perform closure experiments using additional information. Dedicated aircraft campaigns, long-term ground validation sites, as well as combined active and passive observations might help establish smaller error margins and reject unrealistic estimates.

Closely related to the accuracy of instantaneous retrievals is the problem of precipitation detection and clutter removal. The high vertical resolution of space-borne radars offers a distinct advantage over ground-based scanning system. Nevertheless, this

study shows that ground clutter effects are problematic in the CloudSat data and need to be carefully removed, especially in highly structured terrain. This study also illustrates that the use of “near-surface” reflectivity bins (i.e., bins located ~1 km above the surface) alone might be insufficient to effectively eliminate all sources of ground clutter. The use of vertical continuity thresholds provides a simple measure to eliminate many false returns, although some embedded clutter remains even if such thresholds are utilized and further quality control measures are necessary. Vertical continuity thresholds may also reject legitimate low-topped precipitation events, so an enhanced cost-benefit analysis of using these thresholds to help remove clutter that can severely bias the snowfall retrievals must be undertaken. Ground-based, vertically-pointing cloud radars might offer a unique perspective to study whether significant low-topped snowfall does occur since its immune to the clutter contamination that affects the lowest CloudSat data bins. Ground-based instruments can also be an effective tool to develop enhanced relationships between the “near-surface” reflectivity bins (located above 1 km) used in this study and the actual surface reflectivity for snowfall events.

It is important to acknowledge further potential deficiencies in this study that warrant further attention in subsequent research efforts. The results of this study may suffer from the reliance on near-surface reflectivity observations, as situations may arise that can cause an overestimation (e.g., virga) or underestimation (e.g., very shallow precipitation) of precipitation if no reflectivity data are available below the 1 km level (see Hudak et al. 2008 for examples of these issues). Additionally, errors in the temperature data used in this study may adversely affect the results, as any systematic

ECMWF-derived temperature biases may also cause the number of snowfall events in the dataset to be misrepresented. Furthermore, vertical temperature information is not used in this study, so under certain meteorological conditions like elevated temperature inversions, freezing rain or brightband signatures may be inadvertently included in the snowfall dataset and artificially elevate reflectivity counts and alter the detectability statistics. The main assumption of “dry” snowfall utilized in this study may also be unrealistic in snowfall cases where significant supercooled water exists, as the backscattering characteristics of the ice particle models used in this study may not adequately represent heavily rimed frozen particles. Combined active and passive microwave observations of snowfall events may provide a better assessment of the percentage of snowfall cases that contain significant columnar supercooled water content and the potential for excessive riming. Lastly, attenuation and multiple scattering effects need to be further quantified for snowfall events. Attenuation probably doesn’t play an important role for a large percentage of the light snowfall events represented in this study, but the higher end of the reflectivity distribution may be underestimated by as much as 1-2 dB, especially for events like heavy lake effect snow that contain significant cloud liquid water. Multiple scattering effects have been shown to artificially increase the radar signal and would tend to counteract the weakening of the signal due to attenuation, but preliminary evidence using CloudSat data has indicated these effects are most pronounced at moderate to heavy precipitation rates (e.g., Battaglia et al. 2008; Matrosov et al. 2008b). Further studies will be necessary to quantify the degree to which they adversely affect the results presented in this study.

Despite these shortcomings and the large uncertainties currently associated with snowfall retrievals, this study shows how multi-frequency active space-borne observations – with the inclusion of 94 GHz observations – offer a distinct advantage over lower frequency single- or dual-frequency methods for retrieving dry snowfall. The results of this study indicate that the near-surface dry snowfall detection efficacy of a dual-frequency radar operating at 35/13.6 GHz may suffer and might only approach 7%/1%, which translates into about 17%/4% of the total global snowfall accumulation. These results should be considered preliminary, though, and are subject to large potential errors that have been previously discussed. However, this study shows that high frequency active radar observations can be extremely beneficial and can augment future dual-frequency observations of the GPM DPR at the lowest snowfall rates by building a priori or concurrent snowfall rate distributions that adequately capture the entire snowfall rate spectrum. This study reveals strong regional differences in snowfall rate/reflectivity distributions, however, so these regional effects must be taken into consideration when using the CloudSat data (or future cloud radars) to enhance snowfall retrievals of lower frequency instruments. Additionally, the one year snowfall dataset presented in this study is admittedly limited, so sustained multi-year CloudSat observations will be essential to build more robust global and regional snowfall climatologies, and a strong argument can be made for an extended CloudSat mission that would truly benefit snowfall research. Ideally, future active remote sensing missions that study precipitation at higher latitudes will include a multi-frequency instrument to gain the most benefit from space-borne

observations, or minimally include a parallel cloud radar mission that will assist the lower frequency instruments at adequately capturing the lowest snowfall rates.

Table 7.1: Derived Z_e - S relationships for various shapes and frequencies used in Section 7. Published Z_e - S relationships for other recent studies of dry snowfall are also shown. Z_e has units of $[\text{mm}^6 \text{m}^{-3}]$, while S is assumed to be in units of $[\text{mm h}^{-1}]$.

Ice habit (or Reference)	94 GHz	35 GHz	13.6 GHz
LR3	$Z_e=13.16 S^{1.40}$	$Z_e=24.04 S^{1.51}$	$Z_e=34.63 S^{1.56}$
HA	$Z_e=56.43 S^{1.52}$	$Z_e=313.29 S^{1.85}$	$Z_e=163.51 S^{1.98}$
SS	$Z_e=2.19 S^{1.20}$	$Z_e=19.66 S^{1.74}$	$Z_e=36.10 S^{1.97}$
Liu (2008a)	$Z_e=11.50 S^{1.25}$	-	-
Matrosov (2007a)	$Z_e=10.00 S^{0.80}$	$Z_e=56.00 S^{1.20}$	-
Noh et al. (2006)	-	$Z_e=88.97 S^{1.04}$	$Z_e=250.00 S^{1.08}$

Table 7.2: The first two columns are percentages of near-surface proxy DPR-like radar reflectivities at 35/13.6 GHz greater than or equal to the proposed DPR minimum detectable signal of 12/17 dBZ_e calculated from CPR observations. The last two columns are the percentage of total snowfall accumulation that would be detected at 35/13.6 GHz for the same snowfall dataset. Bold numbers indicate percentages after quality-control measures were applied to clutter-contaminated data points (see Section 7g).

	% dBZ ₃₅ > 12	% dBZ _{13.6} > 17	% Total Accumulation (35)	% Total Accumulation (13.6)
Global	7.1/ 7.1	1.2/ 1.2	19.2/ 17.3	5.8/ 3.6
Greenland (land)	8.1/ 7.1	2.7/ 1.6	48.3/ 22.0	38.5/ 7.1
Greenland (ocean)	11.8/ 11.5	3.1/ 2.9	33.3/ 27.3	16.3/ 8.8
Antarctica	4.9/ 4.8	1.1/ 0.9	21.9/ 16.2	10.9/ 4.3
Russia	2.4/ 2.4	0.2/ 0.2	5.8/ 5.8	0.5/ 0.5

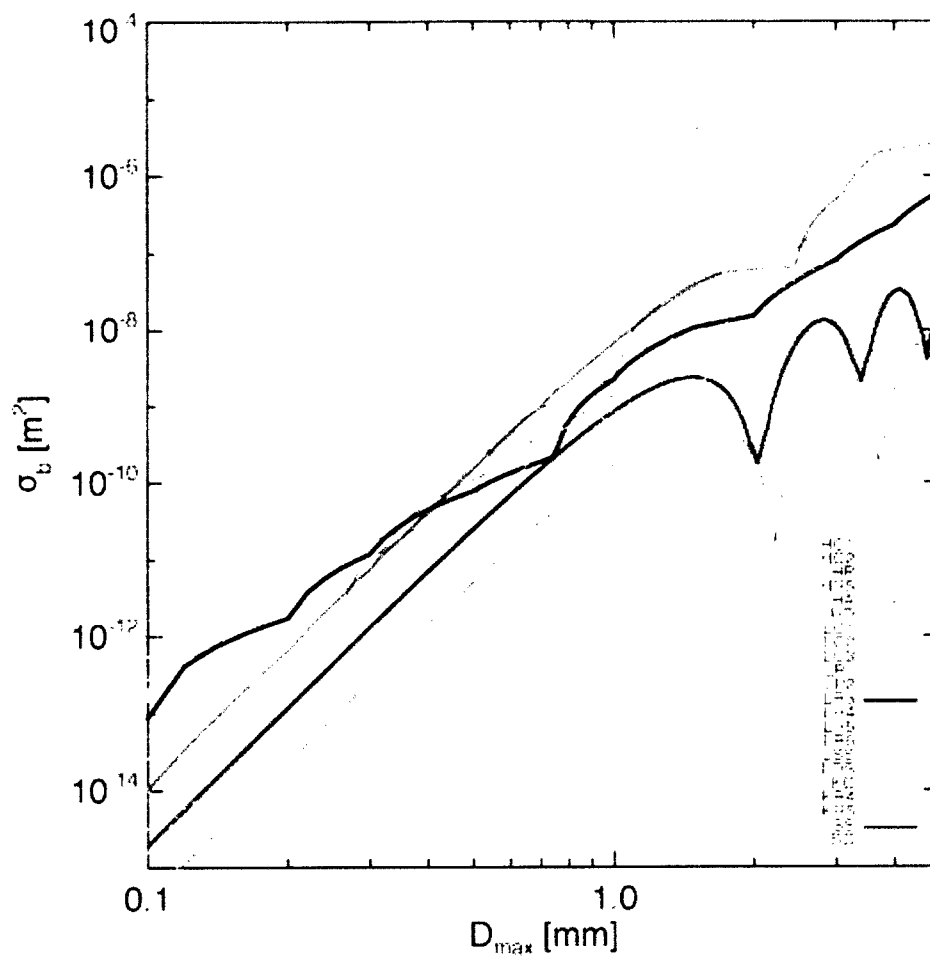


Fig. 7.1: Similar to Fig. 3.7b, but the following three ice particle models used in Section 6 – LR3 (black), HA (red), and SS (purple) – are highlighted by thick, solid lines.

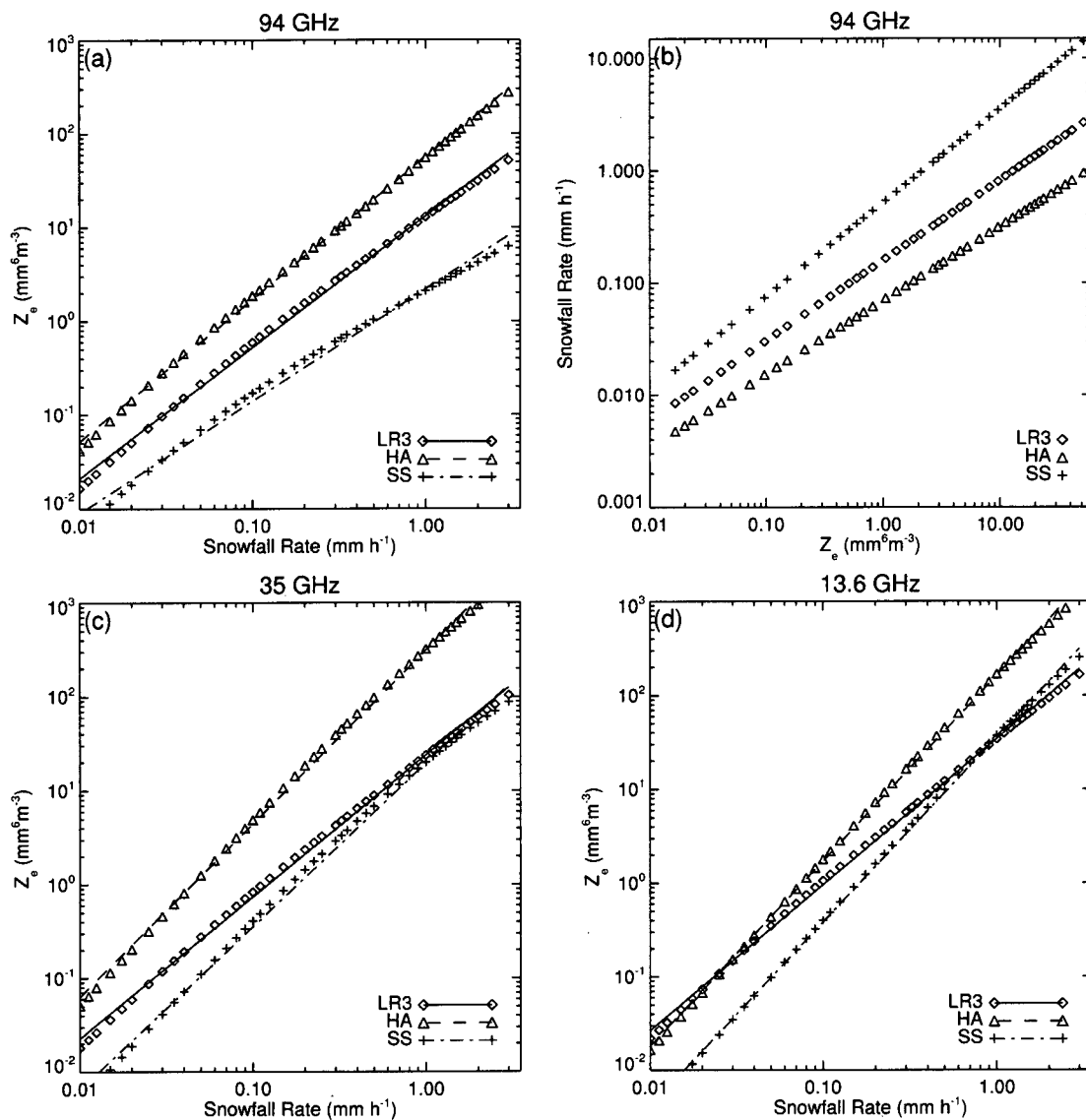


Fig. 7.2: (a) Radar reflectivity factor, Z_e [$\text{mm}^6 \text{m}^{-3}$], as a function of snowfall rate, S [mm h^{-1}], at 94 GHz for the three different ice particle models highlighted in Fig. 7.1 – LR3 (diamonds), HA (triangles), and SS (crosses). Best-fit lines using the Z_e - S relationships outlined in Table 7.1 are also indicated through the data points for each ice particle model. (b) Same as (a), but for S as a function of Z_e (using the Z_e - S relationships from Table 7.1) at 94 GHz. (c) Same as (a), but for 35 GHz. (d) Same as (a), but for 13.6 GHz.

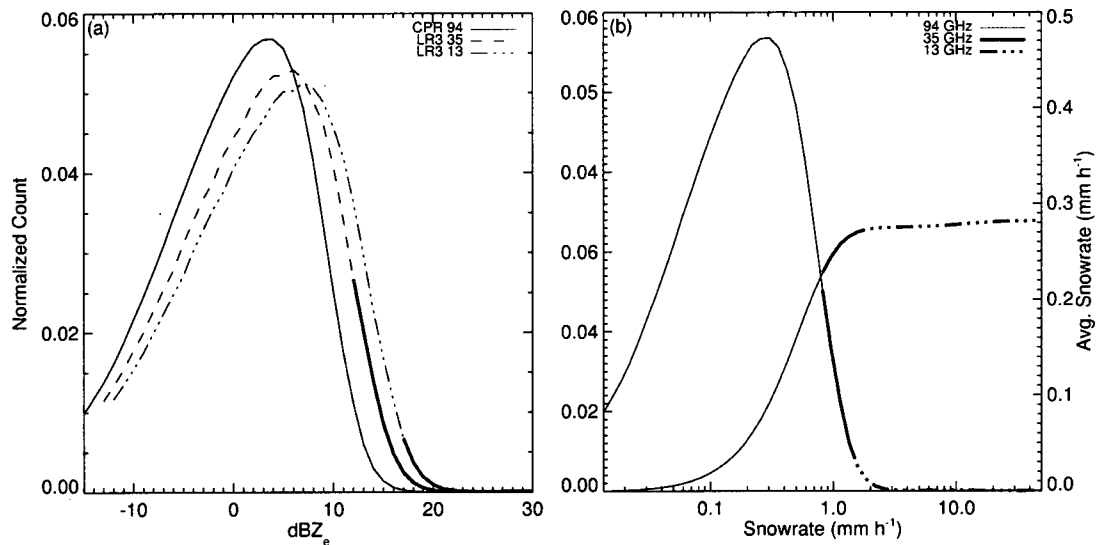


Fig. 7.3: (a) Radar reflectivity factor histograms in 1 dBZ_e bins for observed CloudSat CPR snowfall events (solid line) and calculated proxy radar reflectivities for 35 GHz (dash) and 13.6 GHz (dash-dot) using the LR3 Z_e -S relationship from Table 7.1. The thick solid line on the 35 and 13.6 GHz histograms indicates the reflectivity bins that exceed the proposed minimum detectable signal (MDS) of the GPM DPR for each respective frequency. (b) Conditional snowfall rate histogram (left axis) and average conditional snowfall rate cumulative distribution function (right axis). The thick solid and dash-dot line on each curve represents the snowfall rate threshold corresponding to a MDS of 12 and 17 dBZ_e , respectively.

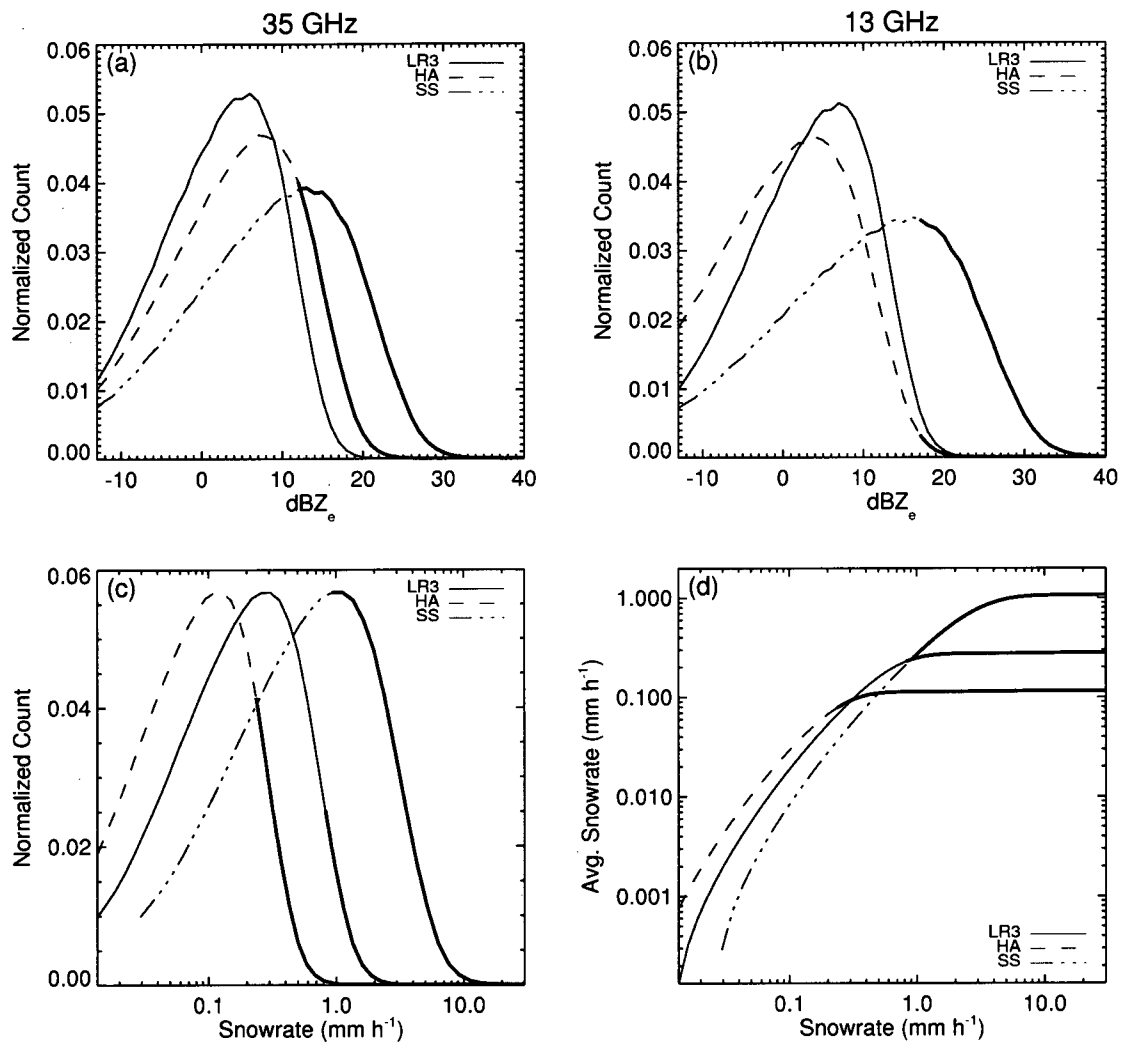


Fig. 7.4: Radar reflectivity factor histograms for (a) 35 GHz and (b) 13.6 GHz for the LR3 (solid), HA (dash), and SS (dash-dot) shapes. The thick solid lines indicate the assumed MDS of 12 and 17 dBZ_e for 35 and 13.6 GHz, respectively. (c) Snowfall rate histograms and (d) cumulative distribution function of the snowfall rate histograms from (c) (expressed as an average snowfall rate) for LR3 (solid), HA (dash), and SS (dash-dot) shapes. The thick solid lines in (c) and (d) indicate the snowfall rate for each shape that corresponds to the assumed MDS of 12 dBZ_e for 35 GHz.

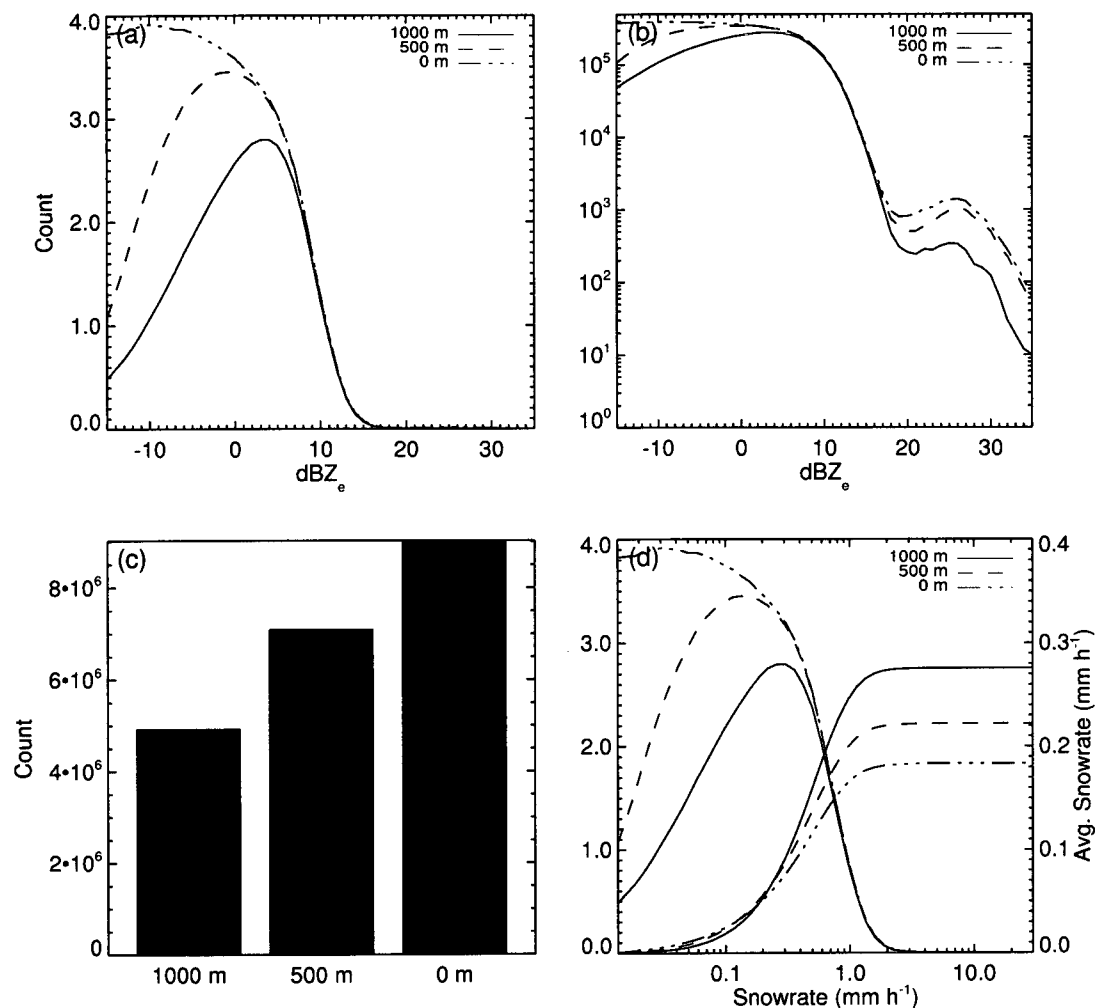


Fig. 7.5: (a) Radar reflectivity factor histograms in 1 dBZ_e bins for observed CloudSat CPR snowfall events based on the assumed vertical reflectivity thickness above the near-surface reflectivity value needed for a near-surface CPR observation to be included in the snowfall dataset (e.g., "1000 m" means the reflectivities must exceed -15 dBZ_e for ~1000 m above the near-surface reflectivity value). (b) Same as (a), but the ordinate is provided in a logarithmic scale to accentuate differences in the histograms above 20 dBZ_e . (c) Bar plot showing the frequency of occurrence of total snowfall cases included in the dataset for the various vertical reflectivity thresholds. (d) Same as (a), but for conditional snowfall rate histogram (left axis) and average conditional snowfall rate cumulative distribution function (right axis). Snowfall rates are calculated using the LR3 Z_e -S relationship in Table 7.1. The frequency of occurrence indicated on the ordinate is in units of 10^5 in (a) and (d).

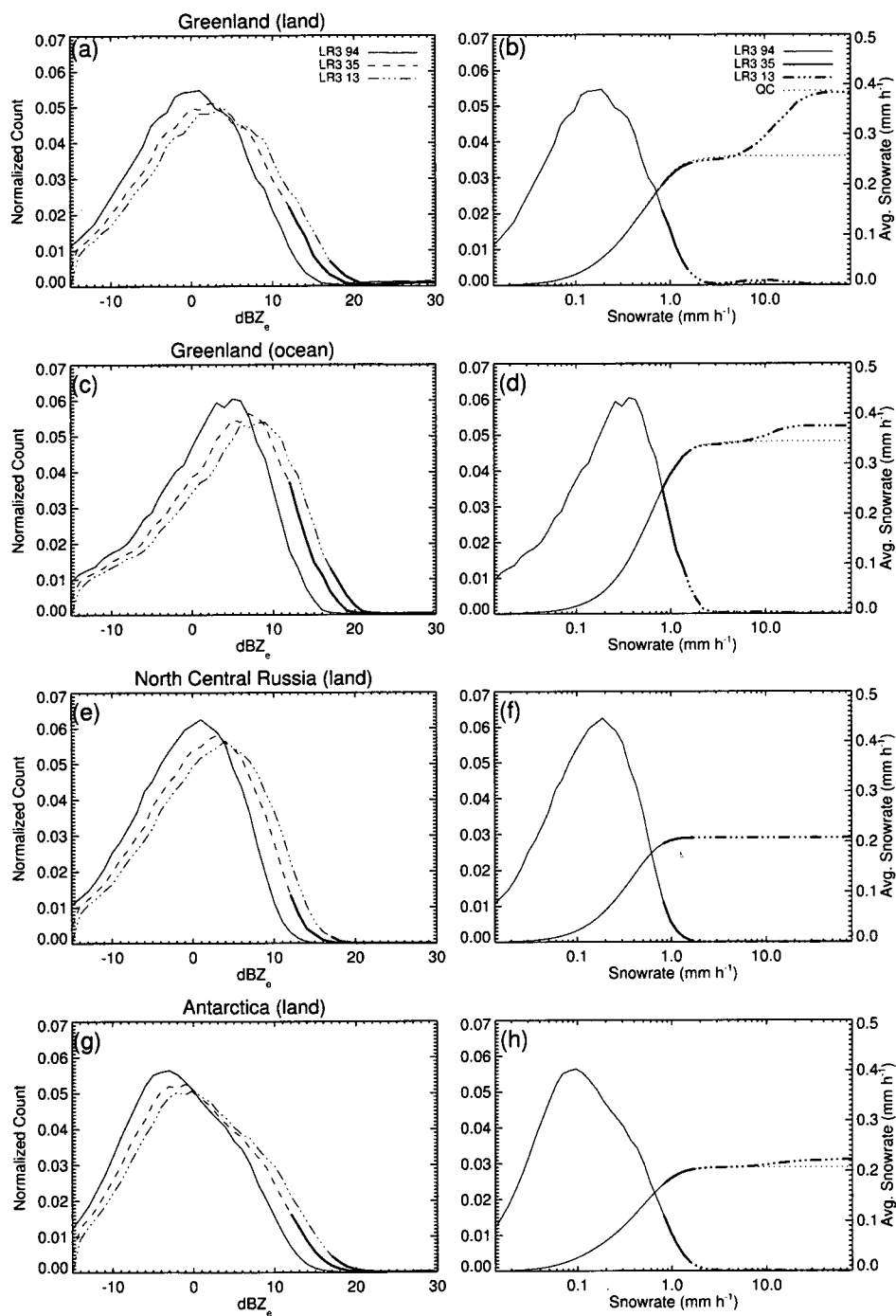


Fig. 7.6: Same as Fig. 7.3, but histograms are derived on a regional, not global, basis. Also, the average conditional snowfall rate thin dotted line shown for the Greenland, Greenland Ocean, and Antarctica regions represents the quality-controlled (QC) cumulative distribution function that alters the reflectivity pixels potentially associated with ground clutter in topographically complex regions.

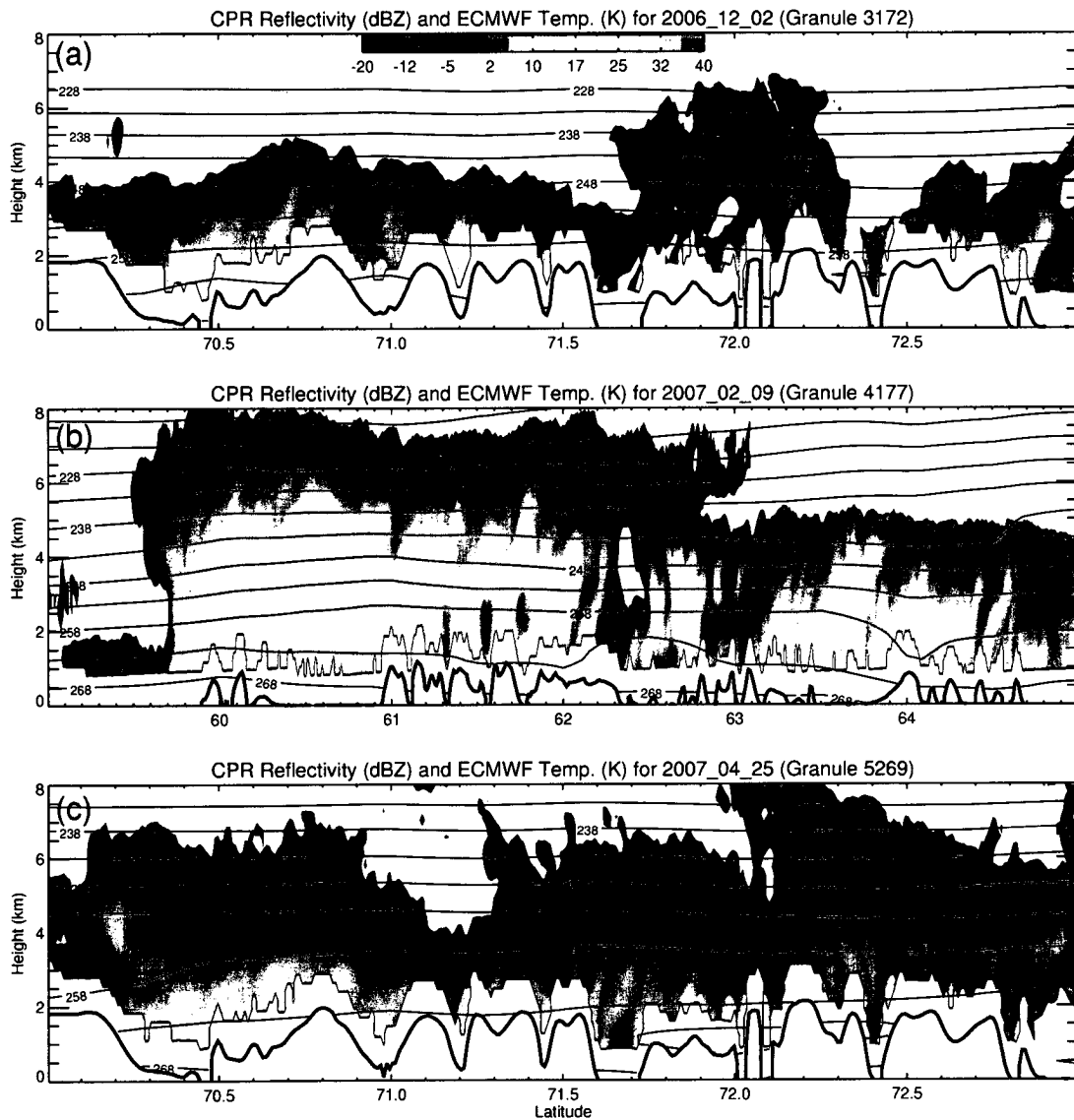


Fig. 7.7: CloudSat CPR radar reflectivity observations [dBZ_e] and ECMWF temperature [K] of three snowfall events over Greenland. The 6th reflectivity bin above the surface (“near-surface” reflectivity) and above are shown to correspond with the actual dataset used in this study. The land surface – derived from a digital elevation map database used in the official CloudSat products – is also indicated by the black line.

8. Summary and outlook

With the anticipated launch of NASA's Global Precipitation Measurement (GPM) mission in the near future, developing physically-based active and passive microwave remote sensing tools will be essential to effectively investigate precipitation at higher latitudes. The following topics presented in this study should provide valuable contributions to GPM preparatory efforts:

- Temperature-dependent Z_e -S/ Z_e -IWC relationships are developed for a variety of different ice particle models and are critical components to both an active/passive combined modeling system and an active-only snowfall retrieval scheme. These relationships can be flexibly utilized with actual observations (e.g., CloudSat) or datasets generated by numerical model output to produce synthetic datasets of higher latitude precipitation events;
- A physical assessment of the ice particle models using a combined active/passive modeling system is performed under precipitating conditions. An ensemble of non-spherical ice particle models produces more physically realistic results from a combined active/passive perspective than other ice models (e.g., low-density spheres), and modeling uncertainties and errors are characterized by precipitation type;

- Active-only space-borne snowfall retrievals using CloudSat data are performed to provide a critical preliminary global and regional snowfall assessment with an accompanying uncertainty analysis.

As mentioned in the respective summaries of Sections 6 and 7, numerous future research avenues naturally arise from the results presented in this study. Near-term goals primarily involve improving key model components to reduce modeling biases that are evident when results are compared to passive microwave observations. Additionally, recent results from Petty and Huang (2010) should be incorporated into the optical properties database, as the complex aggregates² created by Petty and Huang (2010) might possess the necessary combination of radiative and mass-particle size properties desired to properly characterize aggregate particles commonly associated with snowfall events. Furthermore, strengthening links between this research and data assimilation applications should be continued, especially related to defining modeling errors associated with different precipitation types and ice water path. Last, and perhaps most important, is fully exploiting the synergistic observations of CloudSat, AMSR-E, and MHS to produce viable proxy combined active and passive microwave precipitation datasets that can be utilized for general scientific purposes and GPM precipitation algorithm development.

² The Petty and Huang (2010) particle models are comparatively complex and potentially more realistic compared to the pristine ice models populating the current database.

9. Appendix

Table 9.1: Coefficient a for the temperature-dependent 94 GHz $Z_e = aS^b$ relationships.

	-2.5	-7.5	-12.5	-17.5	-22.5	-27.5	-32.5	-37.5	-42.5	-47.5	-52.5	-57.5
HC1	20.97	18.38	15.23	12.09	9.32	6.98	5.12	3.68	2.62	1.86	1.34	0.96
HC2	20.54	18.02	14.88	11.73	8.92	6.57	4.72	3.34	2.35	1.65	1.17	0.84
HP	32.21	29.08	26.42	24.43	22.41	19.69	16.26	12.69	9.55	7.10	5.32	4.08
HR6	11.22	9.26	7.45	6.13	5.10	4.05	2.97	2.03	1.33	0.85	0.55	0.36
HA	26.81	23.42	20.22	17.69	15.36	12.56	9.39	6.48	4.24	2.72	1.75	1.16
HD	56.31	57.57	59.56	61.20	60.87	57.17	49.95	40.70	31.49	23.79	18.03	14.02
LC1	67.40	72.50	74.52	71.44	61.60	45.95	29.07	16.14	8.71	5.01	3.08	1.97
LC2	74.63	83.96	91.79	95.85	93.38	82.41	64.03	43.16	25.80	14.71	8.75	5.62
LC3	55.46	68.73	82.51	94.34	100.74	98.33	85.87	66.02	44.67	27.45	16.43	10.33
LP1	82.71	99.26	117.65	135.94	150.08	154.00	142.42	116.16	84.30	57.57	40.13	29.84
LP2	38.66	43.77	48.52	52.02	52.63	48.72	40.68	31.43	23.67	17.79	13.33	10.11
LR3	29.48	25.38	21.31	17.75	14.30	10.61	7.16	4.66	3.23	2.44	1.91	1.49
LR4	16.42	13.27	9.88	7.01	4.92	3.56	2.62	1.88	1.32	0.96	0.73	0.58
LR5	15.66	12.80	9.79	7.24	5.36	4.05	3.05	2.21	1.56	1.12	0.85	0.66
LR6	14.70	12.41	9.87	7.61	5.84	4.53	3.44	2.49	1.76	1.27	0.96	0.75
LSS	23.63	29.39	35.74	40.86	43.07	41.97	38.24	33.13	27.78	22.80	18.38	14.58
LDS	26.30	30.18	33.92	37.81	39.96	37.95	31.81	24.23	17.75	13.07	9.81	7.47
KC	6.38	4.51	3.18	2.24	1.53	1.00	0.63	0.39	0.23	0.14	0.09	0.06
KR4	6.09	4.77	3.80	2.99	2.25	1.59	1.05	0.66	0.40	0.24	0.15	0.10
KR6	8.25	6.11	4.72	3.66	2.75	1.94	1.29	0.82	0.50	0.31	0.19	0.12
SS	6.62	8.91	11.73	15.37	19.94	24.28	25.60	22.35	16.58	11.15	7.29	4.89
SG	0.27	0.36	0.50	0.67	0.86	1.01	1.05	0.97	0.81	0.64	0.51	0.41
FS	1.34	1.55	1.99	2.72	3.64	4.42	4.54	3.87	2.84	1.91	1.25	0.84
FG	2.81	3.17	3.63	4.19	4.71	4.99	4.84	4.27	3.50	2.75	2.14	1.71
FH	4.71	4.78	4.97	5.19	5.31	5.18	4.73	4.01	3.21	2.49	1.91	1.50

Table 9.2: Exponent b for the temperature-dependent 94 GHz $Z_e = aS^b$ relationships.

	-2.5	-7.5	-12.5	-17.5	-22.5	-27.5	-32.5	-37.5	-42.5	-47.5	-52.5	-57.5
HC1	1.27	1.27	1.26	1.25	1.23	1.20	1.18	1.16	1.14	1.12	1.10	1.27
HC2	1.27	1.28	1.27	1.25	1.23	1.21	1.19	1.16	1.14	1.12	1.10	1.27
HP	1.09	1.08	1.08	1.09	1.10	1.12	1.12	1.12	1.11	1.10	1.09	1.09
HR6	1.24	1.22	1.19	1.18	1.19	1.20	1.20	1.19	1.17	1.15	1.13	1.24
HA	1.18	1.17	1.16	1.17	1.19	1.20	1.21	1.19	1.18	1.16	1.14	1.18
HD	0.99	1.01	1.04	1.07	1.10	1.13	1.14	1.14	1.13	1.12	1.11	0.99
LC1	1.04	1.10	1.16	1.22	1.27	1.30	1.30	1.26	1.21	1.17	1.16	1.04
LC2	0.96	1.01	1.07	1.13	1.18	1.22	1.25	1.25	1.23	1.19	1.16	0.96
LC3	0.84	0.92	0.99	1.05	1.11	1.16	1.19	1.21	1.21	1.19	1.17	0.84
LP1	0.81	0.86	0.92	0.98	1.03	1.09	1.13	1.15	1.16	1.14	1.12	0.81
LP2	0.89	0.94	0.98	1.03	1.08	1.11	1.13	1.12	1.11	1.11	1.12	0.89
LR3	1.23	1.23	1.23	1.24	1.25	1.24	1.21	1.15	1.10	1.08	1.08	1.23
LR4	1.37	1.36	1.32	1.28	1.23	1.20	1.18	1.16	1.12	1.09	1.07	1.37
LR5	1.34	1.33	1.29	1.25	1.22	1.20	1.18	1.16	1.13	1.10	1.08	1.34
LR6	1.31	1.29	1.27	1.24	1.21	1.20	1.18	1.16	1.13	1.10	1.08	1.31
LSS	0.86	0.92	0.97	1.02	1.06	1.07	1.08	1.08	1.08	1.07	1.07	0.86
LDS	0.92	0.95	0.98	1.03	1.08	1.12	1.13	1.13	1.11	1.09	1.08	0.92
KC	1.42	1.38	1.35	1.32	1.30	1.27	1.24	1.21	1.19	1.16	1.14	1.42
KR4	1.33	1.31	1.30	1.29	1.29	1.28	1.26	1.23	1.20	1.17	1.15	1.33
KR6	1.38	1.34	1.32	1.31	1.30	1.28	1.26	1.23	1.20	1.17	1.15	1.38
SS	0.72	0.77	0.81	0.86	0.93	1.01	1.08	1.12	1.13	1.13	1.13	0.72
SG	0.66	0.72	0.79	0.86	0.94	1.01	1.06	1.08	1.10	1.10	1.10	0.66
FS	0.76	0.75	0.79	0.85	0.94	1.02	1.09	1.12	1.14	1.14	1.13	0.76
FG	0.83	0.86	0.90	0.95	1.00	1.05	1.08	1.10	1.11	1.10	1.10	0.83
FH	0.97	0.98	1.01	1.04	1.07	1.10	1.12	1.12	1.12	1.12	1.11	0.97

Table 9.3: Same as Table 9.1, but for 35 GHz.

	-2.5	-7.5	-12.5	-17.5	-22.5	-27.5	-32.5	-37.5	-42.5	-47.5	-52.5	-57.5
HC1	35.54	28.55	21.53	15.51	10.84	7.45	5.08	3.47	2.39	1.66	1.17	0.84
HC2	34.41	27.52	20.51	14.55	10.00	6.77	4.56	3.09	2.11	1.46	1.02	0.73
HP	95.67	86.30	72.31	56.43	41.45	29.19	20.13	13.82	9.56	6.72	4.86	3.66
HR6	31.86	27.82	21.82	15.45	10.05	6.19	3.71	2.21	1.33	0.81	0.50	0.33
HA	153.22	121.77	88.68	59.51	37.36	22.42	13.14	7.65	4.48	2.67	1.65	1.06
HD	315.30	261.39	207.73	158.63	117.21	84.62	60.26	42.70	30.35	21.85	16.12	12.34
LC1	168.16	158.94	143.83	124.32	100.14	71.31	42.77	21.81	10.49	5.46	3.17	1.96
LC2	222.79	214.55	199.02	178.28	154.09	125.93	93.22	59.98	33.45	17.27	9.27	5.56
LC3	246.01	240.29	227.09	207.81	184.68	158.60	128.38	94.12	60.69	34.78	18.93	10.82
LP1	349.26	364.43	369.61	364.58	350.39	324.64	279.60	213.02	140.05	82.56	48.67	31.90
LP2	200.75	213.92	221.41	220.57	205.74	170.81	120.14	71.60	39.69	23.52	15.51	10.99
LR3	60.54	49.88	38.91	29.20	20.96	13.99	8.57	5.09	3.26	2.36	1.81	1.40
LR4	35.33	29.16	21.18	13.64	8.06	4.77	3.03	2.00	1.33	0.93	0.69	0.54
LR5	39.18	32.20	23.36	15.09	9.03	5.46	3.54	2.36	1.58	1.10	0.81	0.62
LR6	43.38	35.47	25.67	16.59	10.00	6.12	3.99	2.66	1.79	1.24	0.91	0.70
LSS	60.76	66.10	66.73	62.60	55.51	47.57	39.79	32.68	26.56	21.40	17.07	13.46
LDS	84.59	99.91	105.33	98.46	81.90	61.16	41.81	27.50	18.41	12.90	9.44	7.09
KC	22.84	11.79	5.98	3.25	1.89	1.11	0.65	0.37	0.22	0.13	0.08	0.05
KR4	30.23	16.64	9.40	5.56	3.33	1.96	1.14	0.65	0.37	0.22	0.13	0.08
KR6	30.04	17.42	10.43	6.42	3.93	2.36	1.38	0.80	0.46	0.27	0.16	0.10
SS	93.53	131.74	155.57	149.35	116.31	75.97	44.08	24.10	13.03	7.22	4.21	2.64
SG	2.58	2.32	1.93	1.49	1.08	0.75	0.50	0.33	0.22	0.15	0.11	0.08
FS	24.25	30.64	33.25	29.80	21.74	13.35	7.43	4.02	2.19	1.22	0.72	0.45
FG	5.51	5.00	4.24	3.36	2.52	1.81	1.28	0.89	0.62	0.44	0.32	0.25
FH	1.75	1.46	1.18	0.93	0.70	0.52	0.38	0.28	0.20	0.14	0.11	0.08

Table 9.4: Same as Table 9.2 but for 35 GHz.

	-2.5	-7.5	-12.5	-17.5	-22.5	-27.5	-32.5	-37.5	-42.5	-47.5	-52.5	-57.5
HC1	1.39	1.37	1.35	1.32	1.28	1.24	1.20	1.17	1.14	1.12	1.11	1.10
HC2	1.39	1.38	1.35	1.32	1.28	1.24	1.21	1.17	1.14	1.12	1.11	1.10
HP	1.21	1.23	1.24	1.24	1.22	1.20	1.17	1.15	1.13	1.11	1.10	1.09
HR6	1.33	1.36	1.37	1.36	1.33	1.30	1.26	1.22	1.18	1.16	1.14	1.12
HA	1.45	1.45	1.44	1.41	1.37	1.33	1.28	1.24	1.20	1.17	1.15	1.14
HD	1.36	1.35	1.33	1.30	1.27	1.23	1.20	1.17	1.15	1.13	1.12	1.11
LC1	1.16	1.19	1.23	1.27	1.31	1.34	1.35	1.31	1.24	1.19	1.17	1.16
LC2	1.14	1.16	1.18	1.20	1.22	1.25	1.28	1.29	1.27	1.22	1.18	1.16
LC3	1.13	1.14	1.16	1.17	1.18	1.20	1.22	1.24	1.24	1.23	1.20	1.17
LP1	0.98	1.01	1.04	1.06	1.09	1.13	1.17	1.20	1.21	1.19	1.16	1.14
LP2	0.97	1.01	1.06	1.12	1.17	1.23	1.25	1.24	1.19	1.15	1.14	1.14
LR3	1.33	1.33	1.32	1.32	1.32	1.30	1.25	1.18	1.12	1.09	1.08	1.08
LR4	1.46	1.47	1.46	1.41	1.34	1.27	1.22	1.18	1.14	1.10	1.08	1.06
LR5	1.47	1.48	1.46	1.41	1.33	1.26	1.22	1.18	1.14	1.10	1.08	1.07
LR6	1.48	1.49	1.46	1.41	1.33	1.27	1.22	1.18	1.14	1.11	1.08	1.07
LSS	1.05	1.09	1.11	1.12	1.12	1.11	1.10	1.09	1.08	1.07	1.07	1.07
LDS	1.01	1.09	1.15	1.19	1.21	1.21	1.19	1.16	1.12	1.10	1.08	1.08
KC	1.72	1.61	1.50	1.42	1.36	1.32	1.27	1.23	1.20	1.17	1.15	1.13
KR4	1.70	1.60	1.51	1.44	1.39	1.34	1.30	1.25	1.21	1.18	1.16	1.14
KR6	1.68	1.58	1.51	1.45	1.40	1.35	1.30	1.26	1.22	1.18	1.16	1.14
SS	0.88	1.03	1.14	1.22	1.27	1.27	1.26	1.23	1.20	1.17	1.15	1.14
SG	1.21	1.24	1.25	1.25	1.24	1.22	1.19	1.17	1.15	1.13	1.12	1.11
FS	0.97	1.10	1.20	1.27	1.30	1.29	1.26	1.23	1.20	1.17	1.15	1.14
FG	1.24	1.26	1.26	1.26	1.24	1.21	1.19	1.17	1.14	1.13	1.11	1.11
FH	1.34	1.33	1.31	1.28	1.25	1.22	1.20	1.17	1.15	1.13	1.11	1.11

10. References

Ashcroft, Peter and Frank Wentz. 2006, updated daily. *AMSR-E/Aqua L2A Global Swath Spatially-Resampled Brightness Temperatures V002*, July 2006-January 2007. Boulder, Colorado USA: National Snow and Ice Data Center. Digital media.

Austin, R., 2007: Cloudsat ECMWF-AUX auxiliary data process description and interface control document, version 5.2. Available from the CloudSat Data Processing Center web site (http://www.cloudsat.cira.colostate.edu/ICD/2B-CWC-RO/2B-CWC-RO_PD_5.1.pdf).

Battaglia, A. J., J. M. Haynes, T. L'Ecuyer, and C. Simmer, 2008: Identifying multiple-scattering-affected profiles in CloudSat observations over the oceans. *J. Geophys. Res.-Atmos.*, **113**, D00A17, doi: 10.1029/2008JD009960.

Bauer, P., J. P. V. P. Baptista, and M. de Iulis, 1999: The effect of the melting layer on the microwave emission of clouds over the ocean. *J.Atmos.Sci.*, **56**, 852-867.

Bauer, P., A. Khain, A. Pokrovsky, R. Meneghini, C. Kummerow, F. Marzano, and J. P. V. P. Baptista, 2000: Combined cloud-microwave radiative transfer modeling of stratiform rainfall. *J.Atmos.Sci.*, **57**, 1082-1104.

Bauer, P., P. Amayenc, C. D. Kummerow, and E. A. Smith, 2001: Over-ocean rainfall retrieval from multisensor data of the Tropical Rainfall Measuring Mission. Part II: Algorithm implementation. *J.Atmos.Ocean.Technol.*, **18**, 1838-1855.

Bauer P., P. Lopez, A. Benedetti, D. Salmond, and E. Moreau, 2006a: Implementation of 1D+4D-Var assimilation of precipitation-affected microwave radiances at ECMWF. I: 1D-Var. *Quart. J. Roy. Meteor. Soc.*, **132**, 2277–2306.

Bauer P., P. Lopez, A. Benedetti, D. Salmond, S. Saarinen, and M. Bonazzola, 2006b: Implementation of 1D+4D-Var assimilation of precipitation-affected microwave radiances in precipitation at ECMWF. II: 4D-Var. *Quart. J. Roy. Meteor. Soc.*, **132**, 2307–2332.

Bennartz, R., 2007: Passive microwave remote sensing of precipitation at high latitudes. *Measuring Precipitation from Space - EURAINSAT and the Future*. V. Levizzani, P. Bauer, and F. J. Turk, Eds., Springer, 165-178.

Bennartz, R., and G. W. Petty, 2001: The sensitivity of microwave remote sensing observations of precipitation to ice particle size distributions. *J.Appl.Meteorol.*, **40**, 345-364.

Bennartz R., and P. Bauer, 2003: Sensitivity of microwave radiances at 85–183 GHz to precipitating ice particles, *Radio Sci.*, **38 (4)**, 8075, doi:10.1029/2002RS002626.

Bennartz, R., and D. B. Michelson, 2003: Correlation of precipitation estimates from spaceborne passive microwave sensors and weather radar imagery for BALTEX PIDCAP. *Int.J.Remote Sens.*, **24**, 723-739.

Bennartz, R., A. Thoss, A. Dybbroe, and D. B. Michelson, 2002: Precipitation analysis using the Advanced Microwave Sounding Unit in support of nowcasting applications. *Meteorol.Appl.*, **9**, 177-189.

Braham, R. R., 1990: Snow particle size spectra in lake effect snows. *J. of Appl. Meteor.*, *Boston, MA*, **29**, 200-207.

Bruggeman, D. A. G., 1935: Berechnung verschiedener physikalischer Konstanten von heterogenen Substanzen: I. Dielectrizitätskonstanten und Leitfähigkeiten der Mischkörper aus isotropen Substanzen. *Ann. Phys.*, **24**, 636–679.

Chen, Y., F. Weng, Y. Han, and Q. Liu, 2008: Validation of the community radiative transfer model by using CloudSat data. *J.Geophys.Res.-Atmos.*, **113**, D00A03, doi:10.1029/2007JD009561.

Deblonde, G., and S. J. English, 2001: Evaluation of the FASTEM-2 fast microwave oceanic surface emissivity model. *Tech. Proc. ITSC-XI*, Budapest, Hungary, WMO and Co-sponsors, 67-78.

Donovan, D. P., M. Quante, I. Schlimme, and A. Macke, 2004: Use of equivalent spheres to model the relation between radar reflectivity and optical extinction of ice cloud particles. *Appl. Opt.*, **43**, 4929-4940.

Draine, B. T., 1988: The Discrete-Dipole Approximation and its Application to Interstellar Graphite Grains. *Astrophys.J.*, **333**, 848-872.

Draine, B. T., and P. J. Flatau, 1994: Discrete-Dipole Approximation for Scattering Calculations. *Journal of the Optical Society of America A-Optics Image Science and Vision*, **11**, 1491-1499.

Draine, B. T., and P. J. Flatau, 2004: User guide for the Discrete Dipole Approximation Code DDSCAT 6.1, <http://arxiv.org/abs/astro-ph/0409262v2>

Ellis, T. D., T. L'Ecuyer, J. M. Haynes, and G. L. Stephens, 2009: How often does it rain over the global oceans? The perspective from CloudSat. *Geophys.Res.Lett.*, **36**, L03815, doi:10.1029/2008GL036728.

English, S. J., R. J. Renshaw, P. C. Dibben, A. J. Smith, P. J. Rayer, C. Poulsen, F. W. Saunders, and J. R. Eyre, 2000: A comparison of the impact of TOVS and ATOVS satellite sounding data on the accuracy of numerical weather forecasts. *Q.J.R.Meteorol.Soc.*, **126**, 2911-2931.

Errico, R. M., P. Bauer, and J. Mahfouf, 2007a: Issues regarding the assimilation of cloud and precipitation data. *J.Atmos.Sci.*, **64**, 3785-3798, doi:10.1175/2006JAS2044.1.

Errico, R. M., G. Ohring, P. Bauer, B. Ferrier, J. Mahfouf, J. Turk, and F. Weng, 2007b: Assimilation of satellite cloud and precipitation observations in numerical weather prediction models: Introduction to the JAS special collection. *J.Atmos.Sci.*, **64**, 3737-3741, doi:10.1175/2007JAS2622.1.

Evans, K. F., 2007: SHDOMPPDA: A radiative transfer model for cloudy sky data assimilation. *J.Atmos.Sci.*, **64**, 3854-3864, doi:10.1175/2006JAS2047.1.

Evans, K. F., G. L. Stephens, 1995: Microwave Radiative-Transfer through Clouds Composed of Realistically Shaped Ice Crystals .1. Single Scattering Properties. *J.Atmos.Sci.*, **52**, 2041-2057.

Evans, K. F., S. J. Walter, G. L. Stephens, and G. M. McFarquhar, 2002: Submillimeter-wave cloud ice radiometer: Simulations of retrieval algorithm performance. *J. Geophys. Res.*, **107**, 4028, doi:10.1029/2001JD000709.

Field, P. R., R. J. Hogan, P. R. A. Brown, A. J. Illingworth, T. W. Choullarton, and R. J. Cotton, 2005: Parametrization of ice-particle size distributions for mid-latitude stratiform cloud. *Q.J.R.Meteorol.Soc.*, **131**, 1997-2017, doi:10.1256/qj.04.134.

Field, P., A. Heymsfield, and A. Bansemmer, 2007: Snow Size Distribution Parameterization for Midlatitude and Tropical Ice Clouds. *J.Atmos.Sci.*, **64**, 4346-4365, doi:10.1175/2007JAS2344.1.

Gordon, G.L., and J.D. Marwitz, 1984: An Airborne Comparison of Three PMS Probes. *J. Atmos. Oceanic Technol.*, **1**, 22–27.

Greenwald, T., R. Bennartz, C. O'Dell, and A. Heidinger, 2005: Fast computation of microwave radiances for data assimilation using the "successive order of scattering" method. *J. Appl. Meteorol.*, **44**, 960-966.

Greco, M., and W. S. Olson, 2008: Precipitating snow retrievals from combined airborne cloud radar and millimeter-wave radiometer observations. *J. Appl. Meteor. Clim.*, **47**, 1634-1650.

Han, Y., P. van Delst, Q. Liu, F. Weng, B. Yan, R. Treadon, and J. Derber, 2006: Community Radiative Transfer Model (CRTM): Version 1. NOAA technical report, 122 pp., NOAA, Washington, D.C.

Hanna, E., J. McConnell, S. Das, J. Cappelen, and A. Stephens, 2006: Observed and modeled Greenland ice sheet snow accumulation, 1958-2003, and links with regional climate forcing. *J. Climate*, **19**, 344-358.

Heidinger, A. K., C. O'Dell, R. Bennartz, and T. Greenwald, 2006: The successive-order-of-interaction radiative transfer model. Part I: Model development. *Journal of Applied Meteorology and Climatology*, **45**, 1388-1402.

Herzogh, P. H., P. V. Hobbs, 1985: Size spectra of ice particles in frontal clouds: correlations between spectrum shape and cloud conditions. *Royal Meteorological Society, Bracknell, Eng., Quarterly Journal*, **111**, 463-477.

Heymsfield, A. J., M. Kajikawa, 1987: Improved approach to calculating terminal velocities of platelike crystals and graupel. *Journal of the Atmospheric Sciences, Boston*, **44**, 1088-1099.

Heymsfield, A. J., A. Bansemer, C. Schmitt, C. Twohy, and M. R. Poellot, 2004: Effective ice particle densities derived from aircraft data. *J. Atmos. Sci.*, **61**, 982-1003.

Hilburn, K. A., F. J. Wentz, 2008: Intercalibrated passive microwave rain products from the unified microwave ocean retrieval algorithm (UMORA). *J. Appl. Meteorol. Climatol.*, **47**, 778-794, doi:10.1175/2007JAMC1635.1.

Hinzman, L. D., and Coauthors, 2005: Evidence and implications of recent climate change in northern Alaska and other arctic regions. *Climatic Change*, **72**, 251-298.

Hong, G., 2007a: Parameterization of scattering and absorption properties of nonspherical ice crystals at microwave frequencies. *J. Geophys. Res.-Atmos.*, **112**, D11208, doi:10.1029/2006JD008364.

Hong, G., 2007b: Radar backscattering properties of nonspherical ice crystals at 94 GHz. *J. Geophys. Res.-Atmos.*, **112**, D22203, doi: 10.1029/2007JD008839.

Houze, R.A., P.V. Hobbs, P.H. Herzegh, and D.B. Parsons, 1979: Size Distributions of Precipitation Particles in Frontal Clouds. *J. Atmos. Sci.*, **36**, 156–162.

Hudak, D., Peter Rodriguez, and N. Donaldson, 2008: Validation of the CloudSat precipitation occurrence algorithm using the Canadian C band radar network. *J. Geophys. Res. (D Atmos.)*, **113**, doi:10.1029/2008JD009992.

Johnson, B. T., 2007: Multi-frequency passive microwave and dual-frequency radar remote sensing of snowfall. PhD Dissertation. University of Wisconsin-Madison. 223 pp.

Johnson, B. T., and G. Petty, 2004: *Improving mid to high latitude passive microwave retrievals and simulations of precipitation using aircraft based doppler radar data (2004 - 13satmet)*. 13. AMS Conf. on Satellite Meteorology and Oceanography, Norfolk, VA (USA), 19-23 Sep 2004, Vol. 13, American Meteorological Society .

Katsumata, M., H. Uyeda, K. Iwanami, and G. Liu, 2000: The Response of 36- and 89-GHz microwave channels to convective snow clouds over ocean: Observation and modeling. *J. Appl. Meteor.*, **39**, 2322–2335.

Kawanishi, T., T. Sezai, Y. Ito, K. Imaoka, T. Takeshima, Y. Ishido, A. Shibata, M. Miura, H. Inahata, and R. W. Spencer, 2003: The Advanced Microwave Scanning

Radiometer for the Earth Observing System (AMSR-E), NASDA's contribution to the EOS for global energy and water cycle studies. *IEEE Trans.Geosci.Remote Sens.*, **41**, 184-194, doi:10.1109/TGRS.2002.808331.

Kelly, G. A., P. Bauer, A. J. Geer, P. Lopez, and J. -. Thepaut, 2008: Impact of SSM/I observations related to moisture, clouds, and precipitation on global NWP forecast skill. *Mon.Weather Rev.*, **136**, 2713-2726, doi:10.1175/2007MWR2292.1.

Kidd, C., 1998: On rainfall retrieval using polarization-corrected temperatures. *Int. J. Remote Sens.*, **19**, 981-996.

Kim, M.-J., 2006: Single scattering parameters of randomly oriented snow particles at microwave frequencies. *Journal of Geophysical Research-Atmospheres*, **111**, D14201.

Kim, M.-J., J. R. Wang, R. Meneghini, B. Johnson, S. Tanelli, J. I. Roman-Nieves, S. M. Sekelsky, and G. Skofronick-Jackson, 2005: Microwave remote sensing of falling snow. *Geoscience and Remote Sensing Symposium, 2005. IGARSS '05. Proceedings. 2005 IEEE International* , **4**, 2645-2648.

Kim, M.-J., M. S. Kulie, C. O'Dell, and R. Bennartz, 2007: Scattering of ice particles at microwave frequencies: A physically based parameterization. *J. Appl. Meteor. Clim.*, **46**, 615-633.

Kim, M.-J., J.A. Weinman, W.S. Olson, D.E. Chang, G. Skofronick-Jackson, and J. R. Wang, 2008: A physical model to estimate snowfall over land using AMSU-B observations. *J. Geophys. Res.-Atmos.*, **113**, DOI:10.1029/2007JD008589.

Kongoli, C., P. Pellegrino, R. Ferraro, N. Grody, and H. Meng, 2003: A new snowfall detection algorithm over land using measurements from the Advanced Microwave Sounding Unit (AMSU). *Geophys.Res.Lett.*, **30**, doi:10.1029/2003GL017177.

Krabill, W., and Coauthors, 1999: Rapid thinning of parts of the southern Greenland ice sheet. *Science*, **283**, 1522-1524.

Kulie, M. S. and R. Bennartz, 2009: Utilizing space-borne radars to retrieve dry snowfall. *J. Appl. Meteorol.*, **48**, 2564-2580.

Kummerow, C., W. S. Olson, and L. Giglio, 1996: A simplified scheme for obtaining precipitation and vertical hydrometeor profiles from passive microwave sensors. *IEEE Trans.Geosci.Remote Sens.*, **34**, 1213-1232.

Kummerow, C., W. Barnes, T. Kozu, J. Shiue, and J. Simpson, 1998: The Tropical Rainfall Measuring Mission (TRMM) sensor package. *J.Atmos.Ocean.Technol.*, **15**, 809-817.

Kummerow, C., Y. Hong, W. S. Olson, S. Yang, R. F. Adler, J. McCollum, R. Ferraro, G. Petty, D. B. Shin, and T. T. Wilheit, 2001: The evolution of the Goddard profiling algorithm (GPROF) for rainfall estimation from passive microwave sensors. *J. Appl. Meteorol.*, **40**, 1801-1820.

L'Ecuyer, T. S., G. L. Stephens, 2002: An estimation-based precipitation retrieval algorithm for attenuating radars. *J. Appl. Meteorol.*, **41**, 272-285.

Li, L., S Durden, and S. Tanelli, 2007: Level 1B CPR process description and interface control document, version 5.3. Available from the CloudSat Data Processing center web site (<http://www.cloudsat.cira.colostate.edu/dataHome.php>).

Liebe, H. J., G. A. Hufford, and T. Manabe, 1991: A Model for the Complex Permittivity of Water at Frequencies Below 1 Thz. *Int J Infrared Millim Waves*, **12**, 659-675.

Liu, C., E. J. Zipser, 2009: "Warm Rain" in the Tropics: Seasonal and Regional Distributions Based on 9 yr of TRMM Data. *J. Clim.*, **22**, 767-779, doi:10.1175/2008JCLI2641.1.

Liu, G., 2004: Approximation of single scattering properties of ice and snow particles for high microwave frequencies. *J. Atmos. Sci.*, **61**, 2441-2456.

Liu, G., 2008a: Deriving snow cloud characteristics from CloudSat observations. *J. Geophys. Res.-Atmos.*, **113**, doi:10.1029/2007JD009766.

Liu, G., 2008b: A database of microwave single-scattering properties for nonspherical ice particles. *Bull. Amer. Meteor. Soc.*, **89**, 1563-1570.

Liu, G., and J. A. Curry, 2000: Determination of ice water path and mass median particle size using multichannel microwave measurements. *J. Appl. Meteor.*, **39**, 1318-1329.

Liu, Q., F. Weng, 2006: Advanced doubling-adding method for radiative transfer in planetary atmospheres. *J. Atmos. Sci.*, **63**, 3459-3465.

Lo, K.K., and R.E. Passarelli, 1982: The Growth of Snow in Winter Storms: An Airborne Observational Study. *J. Atmos. Sci.*, **39**, 697-706.

Locatelli, J. D., and P. V. Hobbs, 1974: Fall speeds and masses of solid precipitation particles. *J. Geophys. Res.*, **79**, 2185-2197.

Luckman, A., T. Murray, R. de Lange, and E. Hanna, 2006: Rapid and synchronous ice-dynamic changes in East Greenland. *Geophys. Res. Lett.*, **33**, L03503, doi:10.1029/2005GL025428.

Mace, G.G., 2007: Level 2 GEOPROF product process description and interface control document algorithm, version 5.3. Available from the CloudSat Data Processing center web site (<http://www.cloudsat.cira.colostate.edu/dataHome.php>).

Mahfouf, J. F., P. Bauer, and V. Marecal, 2005: The assimilation of SSM/I and TMI rainfall rates in the ECMWF 4D-Var system. *Q.J.R.Meteorol.Soc.*, **131**, 437-458, doi:10.1256/qj.04.17.

Marshall, J., and W.M. Palmer, 1948: The distribution of raindrops with size. *J. Atmos. Sci.*, **5**, 165–166.

Matrosov, S. Y., 2007: Modeling backscatter properties of snowfall at millimeter wavelengths. *J. Atmos. Sci.*, **64**, 1727-1736, doi:10.1175/JAS3904.1.

Matrosov, S. Y., A. J. Heymsfield, and Z. Wang, 2005: Dual-frequency radar ratio of nonspherical atmospheric hydrometeors. *Geophys. Res. Lett.*, **32**, L13816, doi:10.1029/2005GL023210.

Matrosov, S. Y., M. D. Shupe, and I. V. Djalalova, 2008a: Snowfall retrievals using millimeter-wavelength cloud radars. *J. Appl. Meteor. Clim.*, **47**, 769-777.

Matrosov, S. Y., A. Battaglia, P. Rodriguez, 2008b: Effects of multiple scattering on attenuation-based retrievals of stratiform rainfall from CloudSat. *J. Atmos. Oceanic Technol.*, **25**, 2199-2208.

Matrosov, S. Y., A. Battaglia, 2009: Influence of multiple scattering on CloudSat measurements in snow: A model study. *Geophys.Res.Lett.*, **36**, doi:10.1029/2009GL038704.

Maxwell Garnett, J. C., 1904: Colours in metal glasses and in metallic films. *Philos. Trans. Roy. Soc. London*, **203A**, 385–420.

McCollum, J., R. Ferraro, 2003: Next generation of NOAA/NESDIS TMI, SSM/I, and AMSR-E microwave land rainfall algorithms. *J.Geophys.Res.(D Atmos.)*, **108**, doi:10.1029/2001JD001512.

Meneghini, R., and L. Liao, 2000: Effective dielectric constants of mixed-phase hydrometeors. *J. Atmos. Oceanic Technol.*, **17**, 628–640.

Mie, G., 1908: Beitrage zur Optik truber Medien, speziell kolloidaler Metallosungen. *Ann. Phys.*, **25**, 377.

Mishchenko, M. I., L. D. Travis, 1998: Capabilities and limitations of a current FORTRAN implementation of the T-matrix method for randomly oriented, rotationally symmetric scatterers. *J.Quant.Spectrosc.Radiat.Transfer*, **60**, 309-324.

Mitchell, D.L., 1991: Evolution of Snow-Size Spectra in Cyclonic Storms. Part II: Deviations from the Exponential Form. *J. Atmos. Sci.*, **48**, 1885–1899.

Mitchell, D. L., 1996: Use of mass- and area-dimensional power laws for determining precipitation particle terminal velocities. *J. Atmos. Sci.*, **53**, 1710-1723.

Mitchell, D. L., and A. J. Heymsfield, 2005: Refinements in the treatment of ice particle terminal velocities, highlighting aggregates. *J. Atmos. Sci.*, **62**, 1637-1644.

Nakamura, K. and T. Iguchi 2007: Dual-wavelength radar algorithm. *Measuring Precipitation from Space - EURAINSAT and the Future*. V. Levizzani, P. Bauer, and F. J. Turk, Eds., Springer, 225-234.

Noh, Y.- J., G. Liu, E.- K. Seo, J. R. Wang, and K. Aonashi, 2006: Development of a snowfall retrieval algorithm at high microwave frequencies. *J. Geophys. Res.-Atmos.*, **111**, D22216, doi:10.1029/2005JD006826.

O'Dell, C. W., A. K. Heidinger, T. Greenwald, P. Bauer, and R. Bennartz, 2006: The successive-order-of-interaction radiative transfer model. Part II: Model performance and applications. *Journal of Applied Meteorology and Climatology*, **45**, 1403-1413.

O'Dell, C. W., F. J. Wentz, and R. Bennartz, 2008: Cloud liquid water path from satellite-based passive microwave observations: A new climatology over the global oceans. *J.Clim.*, **21**, 1721-1739, doi:10.1175/2007JCLI1958.1.

Partain, P., 2007: Cloudsat ECMWF-AUX auxiliary data process description and interface control document, version 5.2. Available from the CloudSat Data Processing center web site (<http://www.cloudsat.cira.colostate.edu/dataHome.php>).

Petty, G. W., 1994a: Physical retrievals of over-ocean rain rate from multichannel microwave imagery. Part 1: Theoretical characteristics of normalized polarization and scattering indexes. *Meteorology and Atmospheric Physics*, **54**, 79-99.

Petty, G. W., 1994b: Physical retrievals of over-ocean rain rate from multichannel microwave imagery. Part 2: Algorithm implementation. *Meteorology and Atmospheric Physics*, **54**, 101-121.

Petty, G. W., 2001: Physical and microwave radiative properties of precipitating clouds. Part II: A parametric 1D rain-cloud model for use in microwave radiative transfer simulations. *J. Appl. Meteorol.*, **40**, 2115-2129.

Petty, G., W., and W. Huang, 2010: Microwave backscatter and extinction by soft ice spheres and complex snow aggregates. *J. Atmos. Sci.*, In press.

Prupaccher, H. R., and J. D. Klett, 1997: *Microphysics of clouds and precipitation* (2nd Ed.). Kluwer Academic Publishers.

Purcell, E. M., and C. R. Pennypacker, 1973: Scattering and Absorption of Light by Nonspherical Dielectric Grains. *Astrophys.J.*, **186**, 705-714.

Rosenkranz, P. W., 1998: Water vapor microwave continuum absorption: A comparison of measurements and models. *Radio Sci.*, **33**, 919-928.

Ryan, B. F., 2000: A bulk parameterization of the ice particle size distribution and the optical properties in ice clouds. *J. Atmos. Sci.*, **57**, 1436-1451.

Sekhon, R., and R. Srivastava, 1970: Snow Size Spectra and Radar Reflectivity. *J. Atmos. Sci.*, **27**, 299-307.

Skofronick-Jackson, G. M., M. J. Kim, J. A. Weinman, and D. E. Chang, 2004: A physical model to determine snowfall over land by microwave radiometry. *IEEE Trans. Geosci. Remote Sens.*, **42**, 1047-1058.

Smith, E. A., and co-authors, 2007: International global precipitation measurement (GPM) program and mission: An overview. *Measuring Precipitation from Space - EURAINSAT and the Future*. V. Levizzani, P. Bauer, and F. J. Turk, Eds., Springer, 611-653.

Spencer, R.W., H.M. Goodman, and R.E. Hood, 1989: Precipitation retrieval over land and ocean with the SSM/I: Identification and characteristics of the scattering signal. *J. Atmos. Oceanic Technol.*, **6**, 254–273.

Stephens, G. L., D. G. Vane, R. J. Boain, G. G. Mace, K. Sassen, Z. Wang, A. J. Illingworth, and coauthors, 2002: The cloudsat mission and the A-Train. *Bull. Amer. Meteor. Soc.*, **83**, 1771-1790.

Surussavadee C. and D. H. Staelin 2006: Comparison of AMSU millimeter-wave satellite observations, MM5/TBSCAT predicted radiances, and electromagnetic models for hydrometeors. *IEEE Trans. Geosci. Remote Sens.*, **44**, 2667-2678.

Tanelli, S., S. L. Durden, E. Im, K. S. Pak, D. G. Reinke, P. Partain, J. M. Haynes, and R. T. Marchand, 2008: CloudSat's Cloud Profiling Radar After Two Years in Orbit: Performance, Calibration, and Processing. *Geoscience and Remote Sensing, IEEE Transactions on*, **46**; **46**, 3560-3573.

Todd, M.C., and J.O. Bailey, 1995: Estimates of rainfall over the United Kingdom and surrounding seas from the SSM/I using the polarization corrected temperature algorithm. *J. Appl. Meteor.*, **34**, 1254–1265.

Weng, F. Z., N. C. Grody, R. Ferraro, A. Basist, and D. Forsyth, 1997: Cloud liquid water climatology from the special sensor microwave/imager. *J.Clim.*, **10**, 1086-1098.

Weng, F., T. Zhu, and B. Yan, 2007: Satellite data assimilation in numerical weather prediction models. Part II: Uses of rain-affected radiances from microwave observations for hurricane vortex analysis. *J.Atmos.Sci.*, **64**, 3910-3925, doi:10.1175/2006JAS2051.1.

Wentz, Frank, and T. Meissner. 2004, updated daily. *AMSR-E/Aqua L2B Global Swath Ocean Products Derived from Wentz Algorithm V002*, July 2006-January 2007. Boulder, Colorado USA: National Snow and Ice Data Center. Digital media.

Westbrook, C. D., R. C. Ball, P. R. Field, and A. J. Heymsfield, 2004: Theory of growth by differential sedimentation, with application to snowflake formation. *Physical Review E*, **70**, 021403.

Westbrook, C. D., R. C. Ball, P. R. Field, and A. J. Heymsfield, 2004: Universality in snowflake aggregation. *Geophys.Res.Lett.*, **31**, L15104.

Wilheit, T., C. D. Kummerow, and R. Ferraro, 2003: Rainfall algorithms for AMSR-E. *IEEE Trans.Geosci.Remote Sens.*, **41**, 204-214, doi:10.1109/TGRS.2002.808312.

Wilson, D. R. and S. P. Ballard, 1999: A microphysically based precipitation scheme for the UK Meteorological Office Unified Model. *Q. J. R. Meteor. Soc.*, **125**, 1607-1636.

Wilson, D. R., and S. P. Ballard, 1999: A microphysically based precipitation scheme for the UK Meteorological Office Unified Model. *Quart. J. Roy. Meteor. Soc.*, **125**, 1607-1636.

Woods, C. P., M. T. Stoelinga, and J. D. Locatelli, 2008: Size spectra of snow particles measured in wintertime precipitation in the Pacific Northwest. *J. Atmos. Sci.*, **65**, 189-205.